USCIPI Report 850

IMAGING WITH RADAR RETURNS

by

Chung-Ching Chen

August 1978

Image Processing Institute
University of Southern California
Los Angeles, California 90007

This research was supported by the Advanced Research Projects Agency of the Department of Defense and was monitored by the Wright Patterson Air Force Base under Contract F-33615-76-C-1203, ARPA Order No. 3119.

ACKNOWLEDGEMENTS

I would like to express my sincere appreciation to Professor Harry C. Andrews, Chairman of my dissertation committee, who helped me decide to work on this most exciting and enjoyable topic and whose constant advice and encouragement made the work completed within the shortest time.

Thanks also go to Mr. James K. Crosby, Manager of the Signature Technology Department, Radar Systems Group, Aerospace Groups of Hughes Aircraft Company. The Department provided the radar data which made possible the experimental aspect of this work. Many invaluable suggestions came from them to keep my time of wandering to a minimum.

The importance of the role of the facility of the Image Processing Laboratory in this work is reflected by the numerous images presented in this dissertation. I wish to thank the whole staff of the Laboratory for providing me with a convenient access to the image processing equipments throughout this work.

Finally my wife Lucy deserves a special thanks. Without her encouragement the work would not have been started. Without her endurance the work would not have been completed.

TABLE OF CONTENTS

Page

ACKNOWLEDGEMENTS ii

LIST OF FIGURES vii

LIST OF TABLES xi

ABBREVIATIONS xii

ABSTRACT xiii

CHAPTER

1. INTRODUCTION 1

2. STRUCTURES OF TWO-DIMENSIONAL TRANSFORMATIONS 4
    - 2.1 Introduction 4
    - 2.2 Lexicographic Ordering 6
    - 2.3 Point Spread Function Matrices and Computational Requirements 8
    - 2.4 Physical Examples 30
    - 2.5 Conclusions 49

3. PRINCIPLES OF RADAR IMAGING 52
    - 3.1 Imaging Systems 52
    - 3.2 Principles of Radar Imaging Systems 54
    - 3.3 Conclusions 64

Chapter Page

4. SAR STRIPPING MODE 66

4.1 Introduction 66

4.2 System Evaluation 72

4.3 Derivation of Point Spread Function for the SAR Imaging System 74

4.4 Simplification of PSF 82

4.5 Conclusions 91

5. TURNTABLE RADAR IMAGING 92

5.1 Introduction 92

5.2 The RAT-SCAT Facility and Data Acquisition 93

5.3 Hypothetical Target Reflectivity Function 95

5.4 PSF of the Imaging System 96

5.5 DOF of the Data 102

5.6 Actual Reconstruction Method 108

5.7 Incoherent Summation of Different Looks 114

5.8 Conclusions 114

6. EXPERIMENTAL RESULTS OF RADAR TURNTABLE IMAGING 116

6.1 Introduction 116

6.2 Imaging a Model F-102 Airplane 116

6.2.1. Physical Properties of the imaging geometry 116

6.2.2. Source data from model F-102 airplane 119

6.2.3. Fourier transforming in the range direction 121

Chapter Page

6.2.4. Azimuth processing 125

6.2.5. Incoherent summation of the looks 133

6.2.6. Imaging the vertical model F-102 134

6.3 Imaging the model F-5E 139

6.4 Comparison Between the Model F-102 and F-5E Images 142

6.5 Imaging a Real F-102 Airplane 148

6.6 Summary and Conclusions 149

7. RADAR IMAGING WITH TARGET MOTION 152

7.1 Introduction 152

7.2 Radar Imaging Equations 152

7.2.1. First interval 155

7.2.2. Second interval 161

7.3 Preprocessing 166

7.4 Range Curvature and Range Bin Alignment 169

7.4.1. Range curvature 169

7.4.2. Range alignment 171

7.4.2.1. spatial domain re-alignment 172

7.4.2.2. frequency domain re-alignment 173

7.5 Motion Compensation 174

7.6 Oversampling and Presuming 177

7.7 Conclusions 180

8. EXPERIMENTAL RESULTS OF RADAR IMAGING WITH TARGET MOTION 181

Chapter Page

8.1 Introduction 181

8.2 Experimental Results - First interval 181

8.2.1. Linear fitting the phase difference and subsequent integration 184

8.2.2. Linear fitting the phase difference and quadratic subtraction 187

8.2.3. Target point referencing 187

8.3 Experimental Results - Second interval 196

8.4 Range Realignment Results 201

8.5 Conclusions 213

9. SUMMARY AND EXTENTIONS 214

9.1 Summary 214

9.2 Sonar Imaging 217

REFERENCES 221

LIST OF FIGURES

Figure		Page
2-1	Imaging models	9
2-2	PSF matrix classification and decomposition	12
	(a) Classification of two-dimensional discrete linear systems	12
	(b) A possible flow chart for classification	22
	(c) Imaging system	24
	(d) Preprocessing of image reconstruction	24
	(e) Processing in transformed domain	26
2-3	SAR stripping mode	32
2-4	CAT scanners	35
2-5	Diffraction limited OTF	39
2-6	Astigmatism and curvature of field	40
2-7	Astigmatic processor	43
2-8	Rotational motion blur	44
2-9	Square aperture magnification	47
2-10	Fourier transforming properties of lenses	47
3-1	Imaging system and reconstruction	53
3-2	Antenna illumination geometry	53
3-3	Analogy between a physical antenna array and a synthetic antenna	63
4-1	Flight-path geometry of stripping mode	67
4-2	Waveforms of pulsed signals	70

Figure Page

4-3 Flight-path geometry on vertical plane 71

4-4 Flight-path geometry on slant range slant 71

4-5 Justification of the stationarity of radar within one pulse time 77

4-6 Reordering of received signal 80

4-7 Range variation of a point target 84

4-8 Block diagram of Equation (4-15) 88

5-1 Relation among radar, target and reference sphere 94

5-2 Geometry of coordinate systems 94

5-3 Raw data in frequency domain 100

5-4 Projection imaging geometry 104

5-5 Spatial and frequency domains of a spatially normalized target 104

5-6 Correlation of the data field and its Fourier transform 107

5-7 Separability of azimuthal and range processing at small angle variation Φ 107

5-8 Separable processing of range and azimuth, small fan angle Φ 112

6-1 Source data of the horizontal model F-102 120

6-2 Fourier transformation along range 122

6-3 Model F-102 azimuth images 128

6-4 Azimuth images of model F-102 130

6-5 Consecutive 6.4° abutting azimuth looks of model F-102 131

6-6 Incoherently integrated azimuth images of model F-102 135

Figure		Page
6-7	Counterparts of Fig. 6-6 with 6.4° aspect coherence intervals	136
6-8	Counterparts of Figs. 6-6 and 6-7 with 12.8° aspect coherence intervals	137
6-9	Incoherently integrated azimuth images of model F-102 with different centers of rotation	138
6-10	Elevation images of model F-102 with different overlapping factors	140
6-11	A sequence of 14 azimuth looks from 0° to 90° for model F-5E	141
6-12	Model F-5E azimuth image	143
6-13	Same as Fig. 6-12 except: center of rotation: range bin 181	143
6-14	Fine tuning of the rotation center for model F-5E azimuth images	144
6-15	Effect of overlapping factors for model F-5E azimuth images	145
6-16	Model F-5E elevation images	146
6-17	Model F-102 and Model F-5E azimuth and elevation images	147
6-18	Images of real F-105 with different centers of rotation	150
7-1	Overall flight path of target	153
7-2	Flight geometry of first interval	154
7-3	Radar trajectory relative to target center in first interval	156
7-4	Geometry of the flight in second interval	162
7-5	Linear radar imaging system	168
7-6	Decomposition of [H] in Fig. 7-5	168
7-7	Determination of azimuth oversampling factor	179

Figure Page

8-1 Overall view of data in first interval 183

8-2 First 512 signatures in first interval 183

8-3 Data in first interval with 128 range bins stacked side by side 185

8-4 Signature number 8001-8512 188

8-5 Motion Compensation on Fig. 8-4(b) using linear curve fitting 188

8-6 Corss-range processing Fig. 8-5 191

8-7 Aircraft radar images with abutting 20 second coherence times 192

8-8 Aircraft images with different coherence times 194

8-9 2:1 range collapsed; coherence time=40 seconds 195

8-10 Same portion as Fig. 8-7(d); phase information only 195

8-11 Overall view of data in second interval 197

8-12 Data in second interval with 128 range bins side by side 198

8-13 Aircraft radar images with abutting 2.5 second coherence times in second interval 200

8-14 Aircraft images with different coherence times 202

8-15 Range-realigned signatures 205

8-16 Aircraft images after range realignment 209

LIST OF TABLES

Table Page

2-1 Covering relations among 9 cases proposed for two-dimensional systems 20

2-2 Properties of the 9 cases 28

2-3 Mathematical examples of the 9 cases 29

2-4 Physical examples of imaging systems for the 9 cases 50

4-1 Summary of PSF simplifications 90

6-1 Model F-102 imaging parameters 118

ABBREVIATIONS

CAT	Computer-aided Tomography
CW	Continuous Wave
DOF	Degree of Freedom
FFT	Fast Fourier Transform
FM	Frequency Modulation
HRR	High Range Resolution
LOS	Line of Sight
MFS	Multiple Frequency Signature
PSF	Point Spread Function
PRF	Pulse Repetition Frequency
PRI	Pulse Repetition Interval
RCS	Radar Cross Section
RAT SCAT	Radar Target Scatter Site
SAR	Synthetic Aperture Radar
SVD	Singular Value Decomposition
TBP	Time Bandwidth Product
TOT	Time on Target

ABSTRACT

This dissertation presents both analytic and processing techniques for various radar imaging systems.

A two dimensional system classification method, which is very general and hence applies to the special case of radar imaging systems as well, is proposed to assist in understanding the structure and describing the limitations of 2-D systems. Once a given system is identified with the simplest possible class, the specific techniques can be directly utilized to process the data or reconstruct the images.

Following a review of radar imaging principles, several coherent radar systems are analyzed and experimented upon. They include synthetic aperture radar (SAR) ground mapping, imaging of an aircraft target from turntable data, and imaging of a flying aircraft target. In each case the point spread function (PSF) of the imaging system is derived or estimated. Physical considerations are then incorporated in mathematical PSF's to categorize the imaging systems according to the aforementioned system classification principle proposed. Degrees of Freedom (DOF) under different imaging geometries are analyzed as a means to determine the amount of information present in the usually huge amount of raw radar data for the purpose of efficient computation and minimal storage requirement. Motion compensation, range curvature, range alignment, de-chirping, FFT, registration and side lobe reduction problems are all addressed and experiments are performed using data from RAT-SCAT (for turntable imaging) and other facilities. The results shown suggest the versatility of coherent radar imaging.

Possible extentions of the current work are discussed. The understanding of the system characteristics, in particular the formation of the radar image will aid in the advancement of techniques for radar image enhancement, encoding, quantization, and restoration.

Chapter 1

INTRODUCTION

This dissertation deals with the radar imaging problems. The objective of a radar imaging system is to reconstruct the target image from its radar returns. Radar imaging geometry is one of the most important factors which determines the complexity of reconstruction procedures and the quality of the images obtainable. Many radar parameters function interactively making the analysis and the optimization of the system very complicated. Physical considerations as well as mathematical assumptions must be taken and made before a practical reconstruction algorithm can be realized.

This dissertation presents both analytic and processing techniques for various radar imaging systems from a system point of view. Degrees of freedom (DOF) under different imaging geometrics are sought as a means to determine the amount of information available in the usually huge amount of raw radar data for the purpose of efficient image reconstruction and minimal storage requirement.

A two-dimensional system classification method, which is very general and hence applies to the special case of radar imaging systems as well, is proposed in Chapter 2 as a preliminary study to assist in understanding the structure and describing the limitations of 2-D systems, with the ultimate goal of providing guidelines for any given system to reduce its reconstruction or processing effort. Once a system is identified with the simplest possible class, the specific techniques can be directly applied to 2-D processing. Mathematical examples are given and physical examples are shown to fit nicely into such categorizations. In addition to the system classification, system decomposition is proposed which would expose more system structure available for current fast processing techniques.

An overview of the radar signalling principles and processing techniques in both the range and azimuth directions, assuming system separability, is presented in Chapter 3. This chapter is devoted to reviewing the one-dimensional radar signal processing methods which form the foundation of general two-dimensional radar image processing discussed in later chapters. Advantages as well as limitations for each simple case are given and compared.

Following the chapter on radar signalling principles, several coherent radar systems are analyzed and experiments performed to support the theoretical work. They include synthetic aperture radar ground mapping of the stripping mode, coherent imaging of aircraft targets from turntable data, and imaging of an actual aircraft target in flight. In each case the point spread function of the imaging system is derived and categorized according to the classification method proposed in Chapter 2. Physical considerations are then incorporated in mathematical PSF's to determine the actual reconstruction algorithms to be used. Motion compensation, de-chirping, range alignment, range curvature, image registration, sidelobe reduction and Fourier transforming problems are all discussed and numerous experiments performed using data from RAT-SCAT (for turntable imaging) and other facilities. The results shown suggest the feasibility and versatility of coherent radar imaging.

Finally, possible extensions of the current work are discussed. Postprocessing upon the images reconstructed from this work can be helpful in extracting the most relevant information once the characteristics of various radar imaging systems are fully understood. Among them, the radar image enhancement, image coding and quantization are valuable examples.

An analogy between radar imaging systems and sonar imaging systems from the mathematical point of view is pointed out which could be a significant extension of this work. However, because of the tremendous disparity between the speeds of an EM wave and a sound wave, many different physical considerations have to be investigated before any feasibility of the sonar imaging system could be concluded.

Chapter 2

STRUCTURES OF TWO-DIMENSIONAL TRANSFORMATIONS

2.1 Introduction

Modern day imaging systems often use digital computers for completion of the imaging process in the form of "reconstruction" algorithms. Such algorithms may be as simple as edge enhancement for modulation transfer function compensation to as complex as polar coordinate tomographic reconstruction methods for three dimensional imaging. However, one common thread throughout these methodologies is the theme of avoiding singularity (ill-conditioning) and consequent noise amplification while simultaneously extracting as much image information as is possible from the original scene of interest. In numerical analysis terms, we wish to reconstruct the object up to the degrees of freedom (rank) of the imaging system without exceeding the computational complexity indigeneous to a particular imaging configuration. Previous analysis for the degrees of freedom of imaging systems includes the earlier work of Twomey [2-1,2-2] followed by Gori and Guattari [2-3]. However, the above degrees of freedom (DOF) are to be differentiated from the computational degrees of freedom (DOF_c) to be proposed in this chapter.

As a preliminary study for our research work of radar imaging systems, this chapter is devoted to a generalization of the concept of the point spread function (PSF) matrix and its role in general two variable to two variable discrete linear mappings (the most common of which are, of course, imaging systems). The importance of understanding the system PFS lies in the fact that the image reconstruction requires, in a general sense, the inversion of the point spread function or its gramian [2-1,2,3,4,5]. It is obvious that one would like to make full use of the structure of the PSF to ease this process. By categorizing the two-dimensional systems according to their structure with associated computational and storage savings one could then apply fast and efficient reconstruction algorithms for each class. Thus, whenever a given category is identified with the simplest possible class, the underlying reconstruction techniques can be directly utilized.

The PSF matrix is generically related to optical analysis of linear space invariant imaging systems, but today has come to represent a much more general mapping, especially if one takes a numerical analysis view. Because of the relatively advanced state of the numeric processing art provided by numerical procedures in problems of inversion of ill-conditioned systems and because the domain of reconstruction for modern day imaging systems is numeric and discrete, linear algebraic analysis techniques are becoming increasingly popular [2-5,6]. In order that we take advantage of such techniques, the following section discusses the implications of formulating our two variable linear mapping systems into one variable lexicographic ordering and the tensor to matrix simplifications thus introduced (at least in a notational sense).

Following the lexicographic discussion, nine categories of PSF matrices are discussed, along with their computational degrees of freedom (DOF_c) and inherent structural relationships. It is shown that these nine models cover all two variable to two variable linear mappings and that the reconstruction and analysis algorithms which relate to the respective models allow for generalized processing results given the users' knowledge of what processing model his imaging system falls into. The models so discussed are then exemplified by illustrations from radar imaging, tomography, optical astigmatism, curvature of field, rotational motion blur, and standard space invariant optical transfer function distortions.

2.2 Lexicographic Ordering

General two variable to two variable imaging systems can be analyzed from three typical models; a continuous-continuous representation, a continuous-discrete representation, or a discrete-discrete representation. Such models result in the following three versions of the integral equations used for imaging (see Figure 2-1).

$$g(x,y) = \iint f(\xi,\eta)h(x,y;\xi,\eta)d\xi d\eta \tag{2-1a}$$

$$\underline{g} = \iint f(\xi,\eta)\underline{h}(\xi,\eta)d\xi d\eta \tag{2-1b}$$

$$\underline{g} = [H]\cdot\underline{f} \tag{2-1c}$$

In the above f represents the original object, g represents the resulting image or observations to be reconstructed and h represents the linear mapping of object to image. The first equation represents a Fredholm integral with a four variable kernel. The second represents a linear mapping with a continuous -discrete kernel, and the third represents the mapping in linear algebraic notation. For the discrete image cases we will index the (x,y) continuous plane with a set of discrete indices (i,k). However, for notational convenience, these indices will be lexicographically ordered to form a "row scanned" vector image $\underline{g}$. Thus the M×N image becomes a vector of dimension MN×1.

In the discrete-discrete model we assume the original object was N×M indexed by (p,q). Due to our lexicographic "row scanning" notation, the point spread function becomes an MN×MN matrix with a "block" notational structure. (Actually imaging a systems with unequal data points in the input and output planes are easily included in this analysis, but for notational convenience, we will restrict our notation to non-square, N×M, but equal input and output planes).

This lexicographic "block" structure of the point spread function matrix can be represented as

$$[H] = \begin{bmatrix} [H]^{(1,1)} & [H]^{(1,2)} & \cdots & [H]^{(1,M)} \\ [H]^{(2,1)} & [H]^{(2,2)} & \cdots & \\ \cdot & & & \\ \cdot & & & \\ \cdot & & & \\ [H]^{(M,1)} & & \cdots & [H]^{(M,M)} \end{bmatrix} \qquad (2\text{-}2)$$

where the individual matrices are N×N given as:

$$[H]^{(i,p)} = [h_{k,q}]^{(i,p)} \qquad (2\text{-}3)$$

See Figure 2-1. Thus the most general point spread function matrix represents an arbitrary kernel h(i,k;p,q) in a discrete notational system. We will see that the block structure of equations (2-2) and (2-3) will be particularly powerful as an analysis tool because, in matrix algebra, such block structure is invariant to matrix addition, multiplication, transposition, inversion, etc. Consequently, "block diagonal", "block Toeplitz", "block circulant", etc. matrices will retain their lexicographic structure throughout manipulation with matrices within their own class.

2.3 Point Spread Function Matrices and Computational Requirements

In this section we discuss various models of point spread function matrices, define the notations used and

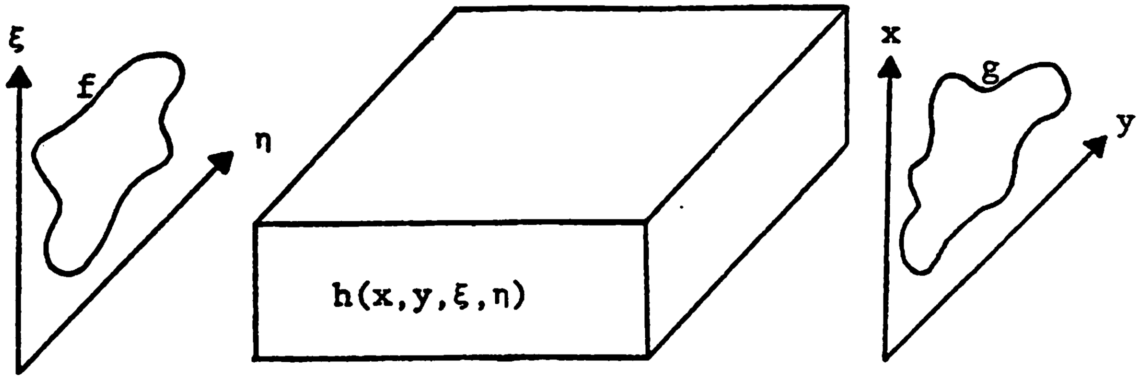

a) Continuous imaging model

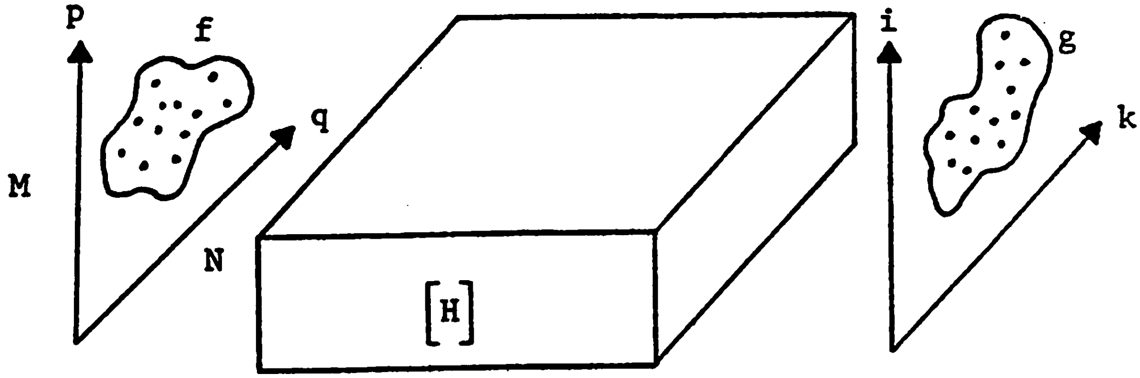

b) Discrete imaging model

N samples in q } input plane
M samples in p }

N samples in k } output plane
M samples in i }

Fig. 2-1. Imaging models

exploit ways to utilize the structure of the system to speed up the reconstructions. In its most general form [H] is that of a nonseparable space variant point spread function and there is no structure without further analytic knowledge.

For our discrete model, three classes of structure could be used to simplify the system description. These structures are labeled i) space invariant, ii) separate, and iii) separable. Let $h(i,k;p,q)$ be the point spread function with input variable index p,q (as in Figure 2-1) and output variable index i,k. Then the definitions of the three concepts mentioned above become:

i) Space Invariant:

invariant in one dimension only

invariant in both dimensions

ii) Separate:

$$h(i,k;p,q) = h_N(k;q/i)h_M(i;p/q)$$

Here $h_M(i;p/q)$ means processing along the i or p direction with q as a parameter fixed for i and p but variable in the k indexed dimension. Note that in h_N and h_M above the conditioning variables i and q are output and input variables respectively. This means h_M occurs before h_N. Of course it is also possible to have separate processing in the other order, i.e.

$$h(i,k;p,q) = h_M(i;p/k)h_N(k;q/p).$$

The order of processing in the two dimensions is not commutative, in contrast to the separable class below. In fact the separable class will always be a subset of the separate class.

iii) Separable:

$$h(i,k;p,q) = h_M(i;p)h_N(k;q)$$

Combinations of the above three structures lead to nine cases which can be diagrammatically depicted as in Figure 2-2(a). Thus there are nine branches of the system classification tree, which have been arbitrarily numbered from 1 to 9 in the figure.

If we define the computational degrees of freedom (DOF_c) of a class of linear system matrices to be the maximum number of independently-determined entries of the matrix which belongs to this class, then intuitively, this DOF_c of the matrix is an indicator of the effort required to diagonalize the matrix or to reconstruct the image in the ideal case. Accordingly, if a structure is a subset of another, its DOF_c must be less than the other. In the following we exploit the structure of the 9 cases of Figure 2-2(a) for two dimensional discrete linear systems in the approximate order of decreasing DOF_c for given nontrivial M and N, i.e. $M \geq 2$ and $N \geq 2$. We will assume that the data are stacked in appropriate lexicographic order as defined in the previous section.

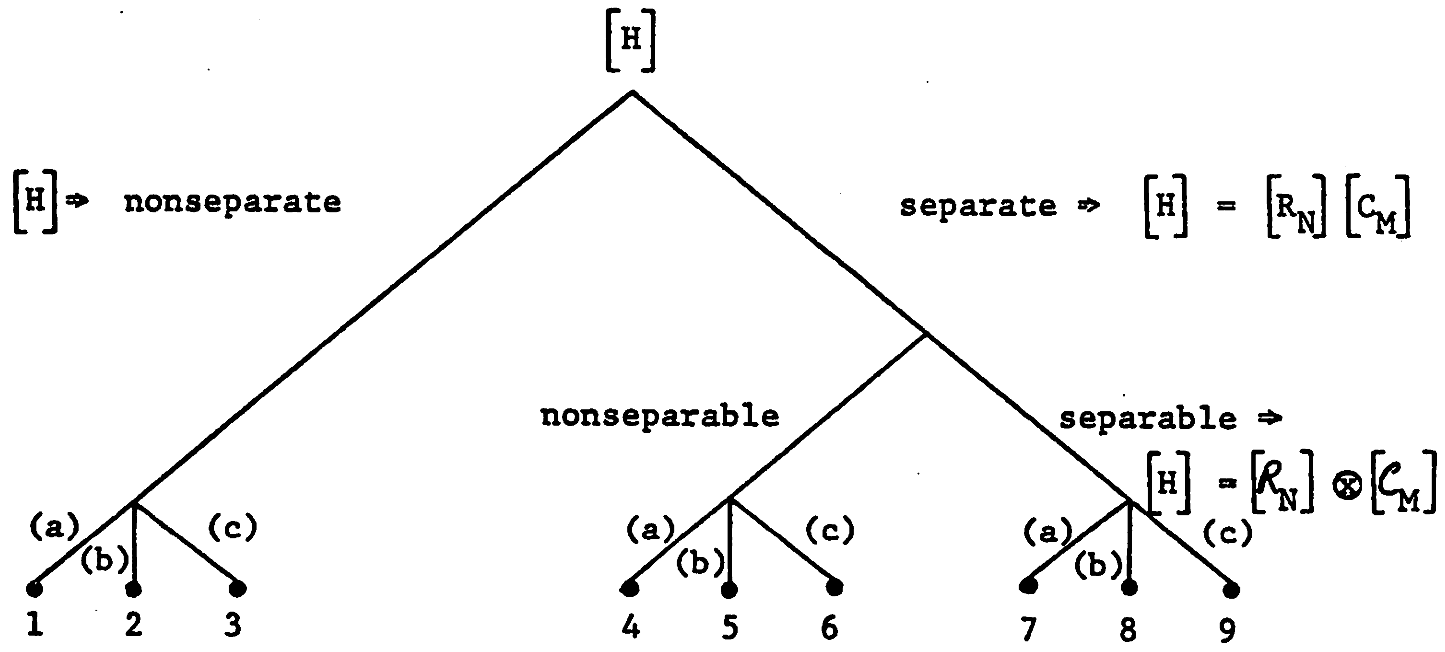

(a) Space variant in both dimensions
(b) Space invariant in one dimension only
(c) Space invariant in both dimensions

Figure 2-2(a). Classification of two-dimensional discrete linear systems

Fig.2-2. PSF matrix classification and decomposition

Case 1: Nonseparate space variant

$$h(i,k;p,q) = h(i,k;p,q)$$

$$\mathrm{DOF}_c([H]) = (NM)^2$$

$$[H] = \begin{bmatrix} [H]^{(1,1)} & \cdots & [H]^{(1,M)} \\ \vdots & \vdots & \vdots \\ [H]^{(M,1)} & \cdots & [H]^{(M,M)} \end{bmatrix} \qquad (2\text{-}4)$$

where $[H]^{(p,i)}$ is N×N.

Case 2: Nonseparate space invariant in one dimension

(assume invariant in (i,p) coordinate)

$$h(i,k;p,q) = h(i-p,k;q)$$

$$\mathrm{DOF}_c([H]) = (2M-1)N^2$$

$$[H] = \begin{bmatrix} [H]^{(0)} & [H]^{(-1)} & \cdots & [H]^{(1-M)} \\ [H]^{(1)} & [H]^{(0)} & & \vdots \\ \vdots & & \ddots & \vdots \\ [H]^{(M-1)} & & \cdots & [H]^{(0)} \end{bmatrix} \qquad (2\text{-}5a)$$

Here matrix (2-5a) is Toeplitz in the (i,p) superscript indices but each submatrix is still arbitrary (thus the N^2 factor in the degrees of freedom).

Had we chosen or been faced with a linear system that was nonseparate but invariant in the (k,q) dimension, then

$$H(i,k;p,q) = h(i,k-q;p)$$

$$\mathrm{DOF}_c[H] = (2N-1)M^2$$

$$[H] = \begin{bmatrix} [H]^{(1,1)} & \cdots & [H]^{(1,M)} \\ \vdots & \ddots & \vdots \\ [H]^{(M,1)} & \cdots & [H]^{(M,M)} \end{bmatrix} \tag{2-5b}$$

where each submatrix $[H]^{(i,p)}$ is Toeplitz, i.e.

$$[H]^{(i,p)} = \begin{bmatrix} h_0 & h_{-1} & \cdots & h_{1-N} \\ h_1 & h_0 & & \vdots \\ \vdots & & \ddots & \vdots \\ h_{N-1} & \cdots & & h_0 \end{bmatrix}^{(i,p)}$$

and aside from this fact, there are no constraints among different $[H]^{(i,p)}$'s.

Case 3: Nonseparate space invariant in both dimensions

$$h(i,k;p,q) = h(i-p,k-q)$$

$$\mathrm{DOF}_c([H]) = (2M-1)(2N-1)$$

$$[H] = \begin{bmatrix} [H]^{(0)} & [H]^{(-1)} & \cdots & [H]^{(1-M)} \\ [H]^{(1)} & [H]^{(0)} & & \vdots \\ \vdots & & \ddots & \vdots \\ [H]^{(M-1)} & & \cdots & [H]^{(0)} \end{bmatrix} \tag{2-6}$$

where

$$[H]^{(j)} = \begin{bmatrix} h_0 & h_{-1} & \cdots & h_{1-N} \\ h_1 & h_0 & & \cdot \\ \cdot & & \cdot & \cdot \\ \cdot & & \cdot & \cdot \\ \cdot & & \cdot & \\ h_{N-1} & & \cdots & h_0 \end{bmatrix}^{(j)}$$

The above matrix for [H] is known as block Toeplitz where the superscript indices are Toeplitz and the submatrices are also Toeplitz. This matrix structure is often approximated by block circulants which are then diagonalizable by the 2-D Fourier transform process [2-7].

Case 4: Separate space variant

(assume column operations first)

$$h(i,k;p,q) = h_N(k;q/i)h_M(i;p/q)$$

$$\mathrm{DOF}([H]) = N^2M+M^2N$$

$$[H] = [R_N][C_M] \tag{2-7a}$$

where

$$[R_N] = \begin{bmatrix} [R]^{(1)} & & & \\ & [R]^{(2)} & & 0 \\ & & \ddots & \\ & 0 & & [R]^{(M)} \end{bmatrix}$$

$$[C_M] = \begin{bmatrix} [C]^{(1,1)} & \cdots & [C]^{(1,M)} \\ \vdots & \ddots & \vdots \\ [C]^{(M,1)} & \cdots & [C]^{(M,M)} \end{bmatrix}$$

where

$$[C]^{(i,p)} = \begin{bmatrix} c_1 & & & 0 \\ & c_2 & & \\ & & \ddots & \\ 0 & & & c_N \end{bmatrix}^{(i,p)}$$

Here $[R_N]$ is a block diagonal and $[C_M]$ is made up of block submatrices which themselves are diagonal. Had we reversed the order of operations for case 4, i.e.

$$h(i,k;p,q) = h_M(i;p/k)h_N(k;q/p)$$

then we would have

$$[H] = [C_M][R_N] \tag{2-7b}$$

where again $[R_N]$ is block diagonal and $[C_M]$ consists of diagonal submatrices. We note that the sparse matrices of the form $[R_N]$ and $[C_M]$ are row operators and column operators, respectively, on lexicographically ordered two dimensional data. Decomposition into forms like (2-7a) or (2-7b) identifies a separate system with sequential row and column (or vice versa) operations which are not necessarily commutable.

Case 5: Separate space invariant in one dimension

(assume invariant in (i,p) coordinate and column operations first)

$$h(i,k;p,q) = h_N(k;q/i)h_M(i-p/q)$$

$$DOF_c([H]) = N^2M+(2M-1)N$$

$$[H] = [R_N]\,[C_M] \tag{2-8}$$

where $[R_N]$ is block diagonal as before but $[C_M]$ is Toeplitz in its subpartition index, i.e.

$$[C_M] = \begin{bmatrix} [C]^{(0)} & [C]^{(-1)} & \cdots & [C]^{(1-M)} \\ [C]^{(1)} & [C]^{(0)} & & \vdots \\ \vdots & & \ddots & \vdots \\ [C]^{(M-1)} & \cdots & & [C]^{(0)} \end{bmatrix}$$

and the $[C]^{(j)}$ are diagonal. Again if the role of the invariance in Case 5 is reversed, i.e., invariant in the (k,q) coordinate

$$h(i,k;p,q) = h_N(k-q/i)\,h_M(i;p/q)$$

then

$$\mathrm{DOF}_c[H] = (2N-1)M+M^2N$$

and

$$[H] = [R_N]\,[C_M]$$

where $[R_N]$ is block diagonal with block matrices being Toeplitz and $[C_M]$ is subpartitioned into arbitrary diagonal matrices as in Case 4. It should be clear that Case 5 is a subset of Case 4.

Case 6: Separate space invariant in both dimensions

(assume column operations first)

$$H(i,k;p,q) = h_N(k-q/i)\,h_M(i-p/q)$$

$$\mathrm{DOF}_c([H]) = (2N-1)M+(2M-1)N$$

$$[H] = [R_N][C_M] \tag{2-9}$$

Here $[R_N]$ is block diagonal with the matrices on the diagonal being Toeplitz and $[C_M]$ is subpartitioned into Toeplitz indices each submatrix of which is diagonal. Therefore Case 6 is a subset of both Case 5 and Case 4.

Case 7: Separable space variant

$$h(i,k;p,q) = h_M(i,p)h_N(k,q)$$

Unlike the separate cases separable operations can be performed regardless of their order. This is because of the independence of one dimensions's operations upon the other's. Thus

$$\mathrm{DOF}_C([H]) = M^2+N^2$$

$$[H] = [\mathcal{R}_N] \otimes [\mathcal{C}_M] \tag{2-10}$$

where ⊗ is the kronecker or direct product matrix operation [2-8]. Here $[\mathcal{R}_N]$ is N×N and $[\mathcal{C}_M]$ is M×M resulting in the M^2+N^2 degrees of freedom. Again $[\mathcal{R}_N]$ and $[\mathcal{C}_M]$ correspond to row and column operations respectively. An equivalent imaging system in non-lexicographic order for this and all separable cases would be to take the N×M object matrix [f] and form the N×M image matrix [g] as

$$[g] = [\mathcal{C}_M][f][\mathcal{R}_N]$$

or in lexicographically stacked notation

$$\underline{g} = [[\mathcal{R}_N] \otimes [\mathcal{C}_M]]\underline{f}$$

Case 8: Separable space invariant in one dimension

(assume invariant in (i,p) coordinate)

$$h(i,k;p,q) = h_M(i-p)h_N(k;q)$$

$$\mathrm{DOF}_C([H]) = (2M-1)+N^2$$

$$[H] = [\mathcal{R}_N] \otimes [\mathcal{C}_M] \qquad (2\text{-}11)$$

where $[\mathcal{C}_M]$ is now a Toeplitz matrix. If the space invariance were in the (k,q) coordinate, then we would have

$$h(i,k;p,q) = h_M(i;p)h_N(k-q)$$

$$\mathrm{DOF}_C([H]) = M^2+2N-1$$

and $[\mathcal{R}_N]$ would be Toeplitz rather than $[\mathcal{C}_M]$.

Case 9: Separable space invariant in both dimensions

$$h(i,k;p,q) = h_M(i-p)h_N(k-q)$$

$$\mathrm{DOF}_C([H]) = (2M-1)+(2N-1)$$

$$[H] = [\mathcal{R}_N] \otimes [\mathcal{C}_M] \qquad (2\text{-}12)$$

where both $[\mathcal{R}_N]$ and $[\mathcal{C}_M]$ are Toeplitz. This particular case is the well-known model for separable linear space invariant imaging systems in which approximations to $[\mathcal{R}_N]$ and $[\mathcal{C}_M]$ with circulants results in the familiar 2-D Fourier transform computation.

Note that $\mathrm{DOF}_C([H]) \leq M^2N^2$ for all nine cases above for all non-trivial 2-dimensional systems with $M \geq 2$ and $N \geq 2$.

If Cases 1-9 above are considered as sets, then there are covering relations among them as depicted in Table 2-1. From the table it is clear that Case 1 covers all other

(read from left to top)

Case \ Case	1	2	3	4	5	6	7	8	9
1	=	$\supset$	$\supset$	$\supset$	$\supset$	$\supset$	$\supset$	$\supset$	$\supset$
2		=	$\supset$	*	*	*	*	$\supset$	$\supset$
3			=	*	*	*	*	*	$\supset$
4				=	$\supset$	$\supset$	$\supset$	$\supset$	$\supset$
5					=	$\supset$	*	$\supset$	$\supset$
6						=	*	*	$\supset$
7							=	$\supset$	$\supset$
8								=	$\supset$
9									=

= : equality
$\supset$: strictly covering
* : partially covering

Examples: Case 4 strictly covers Cases 5,6,7,8,9.

Table 2-1. Covering relations among 9 cases proposed for two-dimensional systems cases. Case 4 covers all higher indexed cases (i.e. 5,6,7, 8,9) as does Case 7 (i.e. 8,9). In the cases of space variance in both dimensions (Cases 1,4,7), nonseparate case (Case 1) covers separate case (Case 4) which in turn covers separable case (Case 7). Similarly, within any group of the nonseparate or separate or separable cases the space variant case covers 1-D space invariant case which in turn covers 2-D space invariant case. They are straight covering relations. However, nonseparate space invariant (1-D or 2-D) cases do not cover the corresponding separate cases, e.g. Case 2 $\not\supset$ Case 5. This is because in the separate cases the sequential processing property, i.e., row operations followed by column operations, etc., allows a more general definition of space invariance in which the invariance is only in a column by column or row by row sense, in contrast to the traditional space invariance in which the processing or "blurring", if any, is uniform throughout the whole image plane.

To classify a given system into the simplest possible case, one could use Fig. 2-2(b) for sequential tests. The terminal nodes are the corresponding simplest cases classified. As an alternative, Fig. 2-2(a) can easily be modified to become a flow chart similar to Fig. 2-2(b). The difference is that in Fig. 2-2(a) the separability property is tested first while in Fig. 2-2(b) the invariance property is tested first. It is noted, however, that to identify

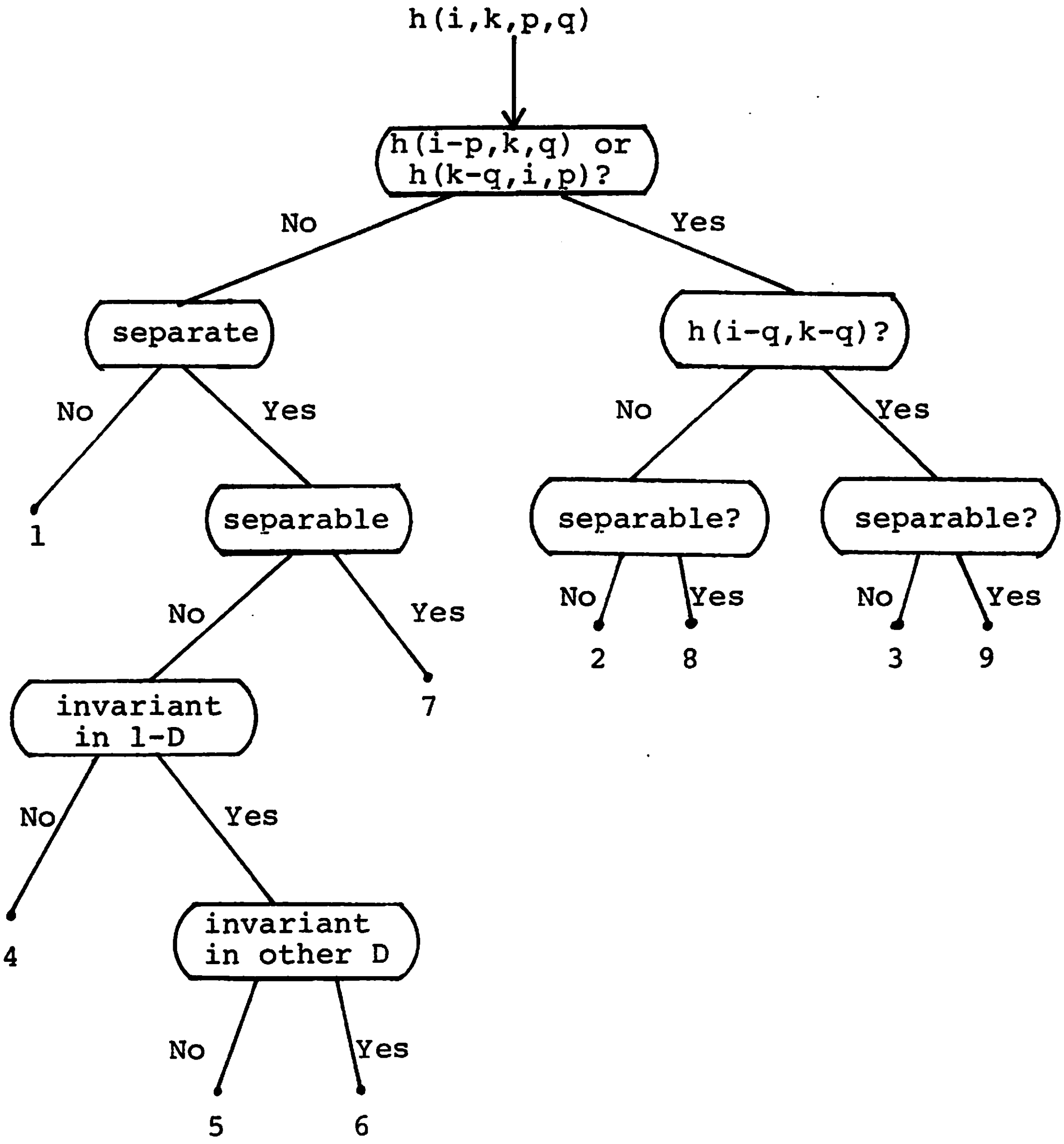

Figure 2-2(b). A possible flow chart for classification; terminal gives case number

Fig. 2-2. PSF matrix classification and decomposition

the separate (but not separable) space invariant cases (Cases 4 and 5), the separability has to be determined first due to the reason explained above.

The knowledge of the covering relations among the nine cases is important in the application of system decomposition. In discrete linear image reconstruction or object estimation from the sensor data or observations, the relation between the data and object, i.e. point spread function matrix [H] has to be determined from the data sensing geometry first and then its inverse estimated and multiplied to the data vector $\underline{g}$ to come up with an estimate of object function $\underline{f}$ as in Fig. 2-1. This reconstruction scheme, although straightforward in theory, usually involves huge amounts of computation because of the complexity of [H]. In the worst case, one would have to resort to a full singular value decomposition (SVD) to find a pseudoinverse $[H]^{-1}$[2-5]. Thus, it is usually desirable to decompose [H] in such a way that it becomes simpler to apply consecutive processings to $\underline{g}$ than $[H]^{-1}$ itself. One possible way is to do some preprocessing $[H_2]^{-1}$ upon $\underline{g}$, as in Fig. 2-2(d) such that $[H_2]^{-1}$ and the remaining processing, $[H_1]^{-1}$, would be much simpler than the $[H]^{-1}$ itself. This means that, if possible, the decomposed component matrices should be in cases covered by the case of [H] and the combined effort is still less than [H] itself. Examples of pre-processing in the radar imaging are motion compensation, range walking

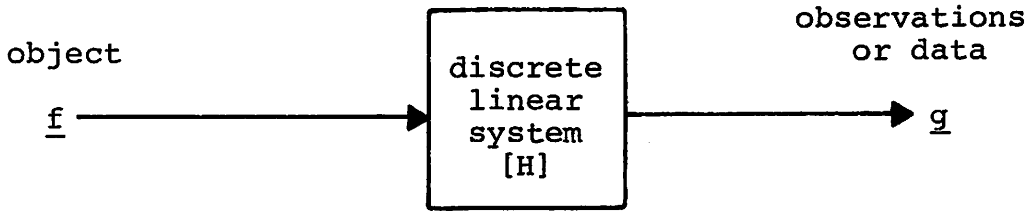

$$\underline{g} = [H]\,\underline{f}$$

Figure 2-2(c). Imaging system

Fig. 2-2. PSF matrix classification and decomposition

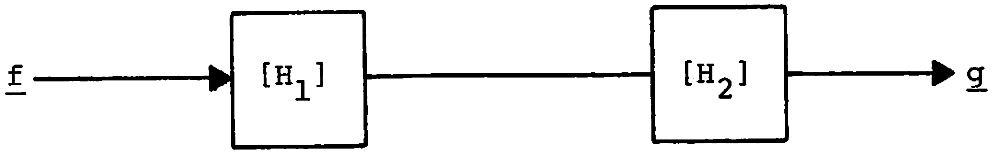

$$[H] = [H_2]\,[H_1]$$

$$[H]^{-1} = [H_1]^{-1}\,[H_2]^{-1}$$

$$\hat{\underline{f}} = [H]^{-1}\,\underline{g}$$

$$= [H_1]^{-1}\,[H_2]^{-1}\,\underline{g}$$

where $[H_2]^{-1}$: preprocessing

s.t. $[H_1]$ & $[H_2]$ are computationally simpler than $[H]$.

Figure 2-2(d). Preprocessing of image reconstruction

Fig. 2-2. PSF matrix classification and decomposition

compensation, data presuming, etc., as in [2-1].

Another existent technique of system decomposition is to process the data in the transformed domain as in Fig. 2-2(e). Sawchuk [2-14] proposed a geometrical transformation of [G] in the reconstruction of rotationally blurred images with successful results. Another simple example could be the processing of polar coordinate Fourier transformation which originally belongs to Case 2. An interpolation transformation [G] [2-17] from polar coordinates to rectangular coordinates could make the system separable.

It is pointed out that separability and invariance are not the only structure that can be utilized. In some situations, the structure within our categorization could be further scrutinized. For example although a 2-D FFT belongs to Case 7 which is space variant, the availability of fast algorithms make it competitive with the 2-D separable convolution which is Case 9. In fact, in the case of space-invariant processing, sometimes it is preferable to apply a transforming technique similar to Fig. 2-2(e) to do simple point by point operation in the transformed eigenspace, i.e., the Fourier domain. This is one of a few examples where a specific structure on top of the case structure could even be utilized to further speed up the processing within that case. It is the purpose of the system classification and decomposition to extract as much

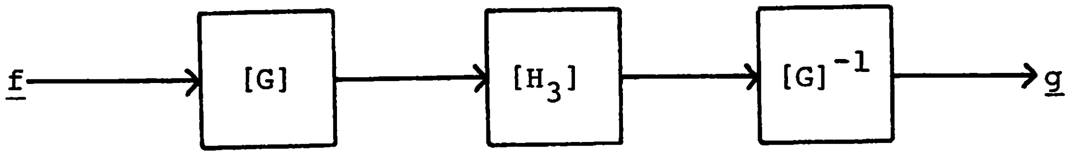

$$[H] = [G]^{-1}\,[H_3]\,[G]$$

$$[H]^{-1} = [G]^{-1}\,[H_3]^{-1}\,[G]$$

$$\hat{\underline{f}} = [H]^{-1}\,\underline{g}$$

$$= [G]^{-1}\,[H_3]^{-1}\,[G]\,\underline{g}$$

s.t. [G] and [H_3] are computationally simpler than [H]

Figure 2-2(e). Processing in transformed domain

Fig. 2-2. PSF matrix classification and decomposition

system structure as possible for the purpose of fast processing. However, although we have proposed a classification method, the general decomposition is the state of art which demands ingenuity. It suffices to say that, in general, the principle of the decomposition is such that more fast processing techniques can be applied upon the transformed data. However, some disadvantages might accompany the decomposition of the system in that one might have to sacrifice some degrees of freedom (in the information sense) for fast processing. This is because the optimal mean-square reconstruction is guaranteed only by the availability of singular values of [H] itself [2-6], which is usually very difficult to infer from singular values of product component matrices.

To summarize these 9 cases for linear two dimensional systems, Table 2-2 has been prepared. From the table it is clear that a large variety of systems and their computational degrees of freedom can be formulated depending on specific point spread function circumstances. To make these 9 cases more meaningful and relevant to actual imaging conditions, a group of examples are developed in the following section as illustration of some of the cases discussed here. However, before proceeding to the following section, the reader's attention is drawn to the mathematical examples of PSF's of Table 2-3 associated with the individual case numbers of Table 2-2. While these are

Case No.	Description	PSF	#DOF([H])	Equation	[H]
1	non-separate space variant	$h(i,k;p,q)$	M^2N^2	(2-4)	block structure
2	non-separate 1-D space invariant	$h(i-p,k;q)$ $h(k-q,i;p)$	$(2M-1)N^2$ $(2N-1)M^2$	(2-5a) (2-5b)	Toeplitz in 1 dimension Toeplitz in other dimension
3	non-separate 2-D space invariant	$h(i-p,k-q)$	$(2M-1)(2N-1)$	(2-6)	block Toeplitz
4	separate space-variant	$h_N(k;q/i)h_M(i;p/q)$ $h_N(k;q/p)h_M(i;p/k)$	N^2M+M^2N N^2M+M^2N	(2-7a) (2-7b)	$[R_N]\,[C_M]$, $[R_N]$=block diagonal $[C_M]\,[R_N]$, $[C_M]$=diagonal blocks
5	separate 1-D space invariant	$h_N(k;q/i)h_M(i-p/q)$ $h_N(k;q/p)h_M(i-p/k)$ $h_N(k-q/i)h_M(i;p/q)$ $h_N(k-q/p)h_M(i;p/k)$	$(2M-1)N+N^2M$ $(2M-1)N+N^2M$ $(2N-1)M+M^2N$ $(2N-1)M+M^2N$	(2-8)	$[C_M]$=diagonal blocks Toeplitz in 1-D $[R_N]$=block diagonal
6	separate 2-D space invariant	$h_N(k-q/i)h_M(i-p/q)$ $h_N(k-q/p)h_M(i-p/k)$	$(2M-1)N+(2N-1)M$ $(2M-1)N+(2N-1)M$	(2-9)	$[C_M]$=diagonal blocks Toeplitz in 1-D $[R_N]$=block diagonal Toeplitz matrices
7	separable space variant	$h_N(k;q)h_M(i;p)$	M^2+N^2	(2-10)	$[\mathbb{R}_N] \times [\mathbb{C}_M]$
8	separable 1-D space invariant	$h_N(k;q)h_M(i-p)$ $h_N(k-q)h_M(i;p)$	$(2M-1)+N^2$ $(2N-1)+M^2$	(2-11)	$[\mathbb{C}_M]$=Toeplitz $[\mathbb{R}_N]$=Toeplitz
9	separable 2-D space invariant	$h_N(k-q)h_M(i-p)$	$(2N-1)+(2M-1)$	(2-12)	both $[\mathbb{R}_N]$ and $[\mathbb{C}_M]$ Toeplitz

Table 2-2. Properties of the 9 cases

Case No.	Point Spread Function
1	$h(i,k;p,q) = \exp\{-(i+k+p+q)^2\}$
2	$h(i-p,k;q) = \exp\{-((i-p)+k+q)^2\}$ $h(k-q,i;p) = \exp\{-((k-q)+i+p)^2\}$
3	$h(i-p,k-q) = \exp\{-((i-p)+(k-q))^2\}$
4	$h_N(k;q/i)h_M(i;p/q) = \exp\{-(k+q+i)^2\}\exp\{-(i+p+q)^2\}$ $h_N(k;q/p)h_M(i;p/q) = \exp\{-(k+q+p)^2\}\exp\{-(i+p+k)^2\}$
5	$h_N(k;q/i)h_M(i-p/q) = \exp\{-(k+q+i)^2\}\exp\{-((i-p)+q)^2\}$ $h_N(k;q/p)h_M(i-p/k) = \exp\{-(k+q+p)^2\}\exp\{-((i-q)+k)^2\}$ $h_N(k-q/i)h_M(i;p/q) = \exp\{-((k-q)+i)^2\}\exp\{-(i+p+q)^2\}$ $h_N(k-q/p)h_M(i;p/k) = \exp\{-((k-q)+p)^2\}\exp\{-(i+p+k)^2\}$
6	$h_N(k-q/i)h_M(i-p/q) = \exp\{-((k-q)+i)^2\}\exp\{-((i-p)+q)^2\}$ $h_N(k-q/p)h_M(i-p/k) = \exp\{-((k-q)+p)^2\}\exp\{-((i-p)+k)^2\}$
7	$h_N(k;q)h_M(i;p) = \exp\{-(k+q)^2\}\exp\{-(i+p)^2\}$
8	$h_N(k;q)h_M(i-p) = \exp\{-(k+q)^2\}\exp\{-(i-p)^2\}$ $h_N(k-q)h_M(i;p) = \exp\{-(k+q)^2\}\exp\{-(i-p)^2\}$
9	$h_N(k-q)h_M(i-p) = \exp\{-(k-q)^2\}\exp\{-(i-p)^2\}$

Table 2-3. Mathematical examples of the 9 cases

mathematically correct, they may not be meaningful in a physical sense. For physically meaningful examples, the reader is referred to the following section.

2.4 Physical Examples

This section is designed to put the numeric structure of the point spread function matrices described above into physically meaningful perspective with respect to some typical realistic imaging configurations. While naturally not all imaging systems can be investigated, it is hoped that enough illustrations are presented to provide a firm grasp of the relationships of the real world physical phenomena with the numerical structure of the computer world computational phenomena in implementing restoration and/or reconstruction algorithms. Examples are taken from optical imaging, x-ray imaging, and radar imaging and range in complexity from Case 1 (i.e., arbitrary imaging) to Case 9 (that of separable space invariant imaging). The illustrations are presented below.

Case 1: Nonseparate space variant

This imaging configuration represents an arbitrarily complex system in which the object field f(p,q) is mapped into the image field g(i,k) by a point spread function matrix [H] of arbitrary entries. In the extremely precise higher order modelling of any linear imaging system, the limiting situation would result in this case. Naturally, such precision is not warranted in many situations, thereby leading to the simplification of succeeding examples.

Case 2: Nonseparate space invariant in one dimension

Three examples of imaging systems that fit into this category come from radar imaging and x-ray imaging. In the former situation consider the geometry of a synthetic aperture radar (SAR) operating in the "stripping" mode. This configuration is illustrated in Figure 2-3. After some analysis the point spread function can be shown to be [2-9]:

$$h(x_2,t;x_1,y_1) = \exp(j\omega_o t)A(x_1-x_2,y_1,z_2)f_s\left(t-\frac{2[(x_1-x_2)^2+y_1^2+z_2^2]^{\frac{1}{2}}}{c}\right)$$

$$\exp\left\{-j\omega_c\frac{2[(x_1-x_2)^2+y_1^2+z_2^2]^{\frac{1}{2}}}{c}\right\} \qquad (2\text{-}13)$$

where the parameters are defined as:

ω_o: range offset angular frequency
ω_c: carrier angular frequency
A: antenna beam pattern
f_s: modulating function of signal pulse
z_2: flight height
c: speed of light
x_2: takes on discrete values (nvT_s)
v: aircraft velocity
T_s: interpulse period

In Chapter 4 Eq. (2-13) will be rederived and becomes

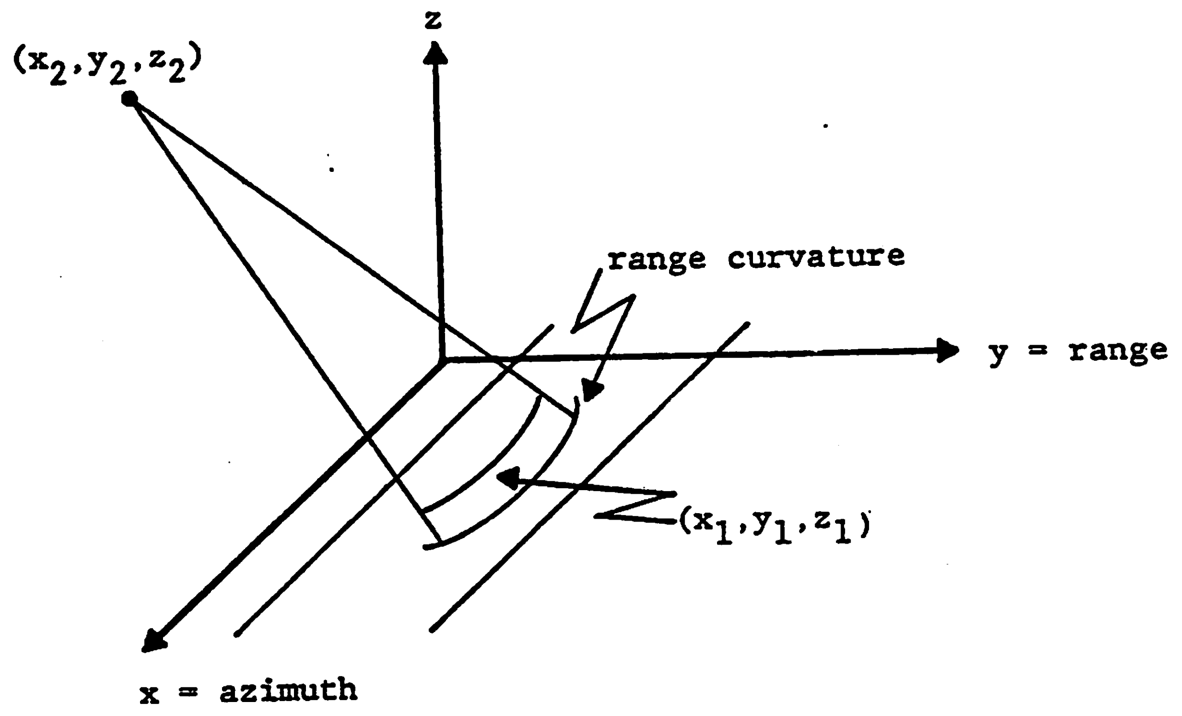

z_1, y_2, z_2: constants

a) SAR geometric configuration

Fig. 2-3. SAR stripping mode

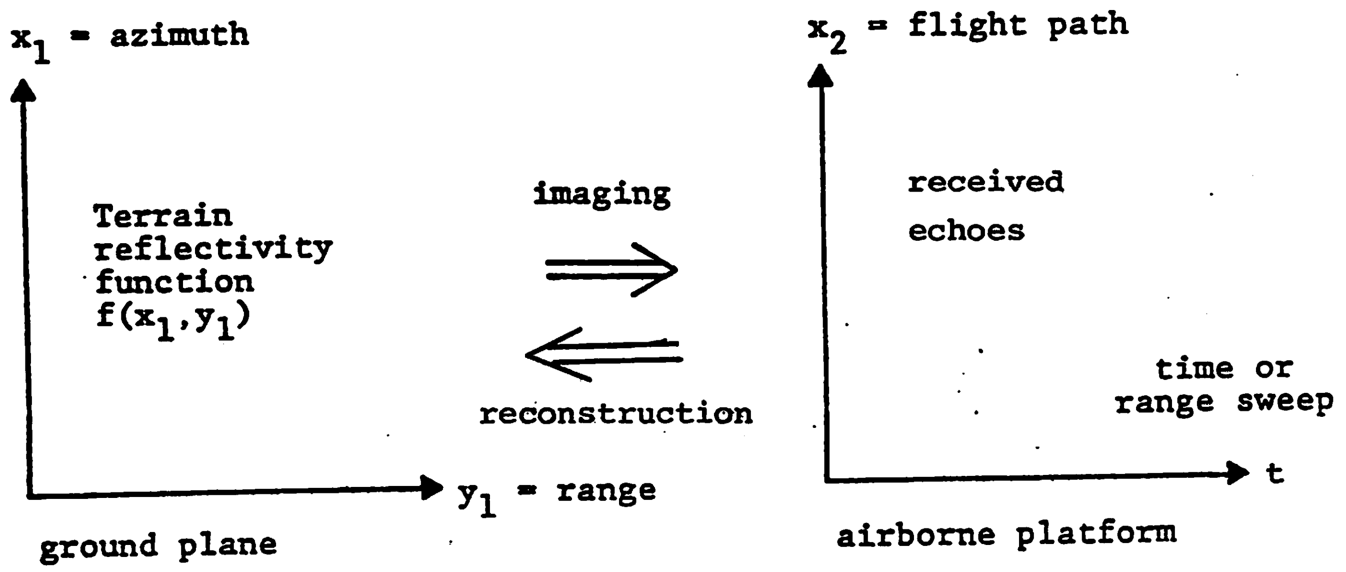

b) Imaging planes

Fig. 2-3. (Continued)

Eq. (4-10). With (x_1,y_1) being the input or object plane and (x_2,t) being the output or image plane we see that

$$h(x_2,t;x_1,y_1) = h(x_2-x_1,t;y_1) \qquad (2\text{-}14a)$$

or in our discrete numeric notation of the previous section

$$h(i,k;p,q) = h(i-p,k;q) \qquad (2\text{-}14b)$$

The above equation is referred to as the SAR imaging equation with range curvature. The range curvature forces the point spread function to be nonseparate. However, we will see in subsequent cases that, by ignoring such curvature, great simplification in processing can be achieved.

The second example for this case is obtained from computer aided tomography (CAT) scanners in which x-ray cross-section slices are obtained by computer reconstruction of radiation projections. Figure 2-4 illustrates the geometry of such systems. Essentially the imaging equation is given by

$$\rho(r,\theta) = \iint f(x,y)h(r,\theta;x,y)dxdy \qquad (2\text{-}15)$$

where the integration is taken over the unit circle as in [2-4]. Assuming the blur is space invariant along r and independent of θ, McCaughey and Andrews [2-4] have shown that once r and θ are sampled the PSF becomes

$$h(r,\theta;x,y) = h(x\cos\theta+y\sin\theta-r)$$

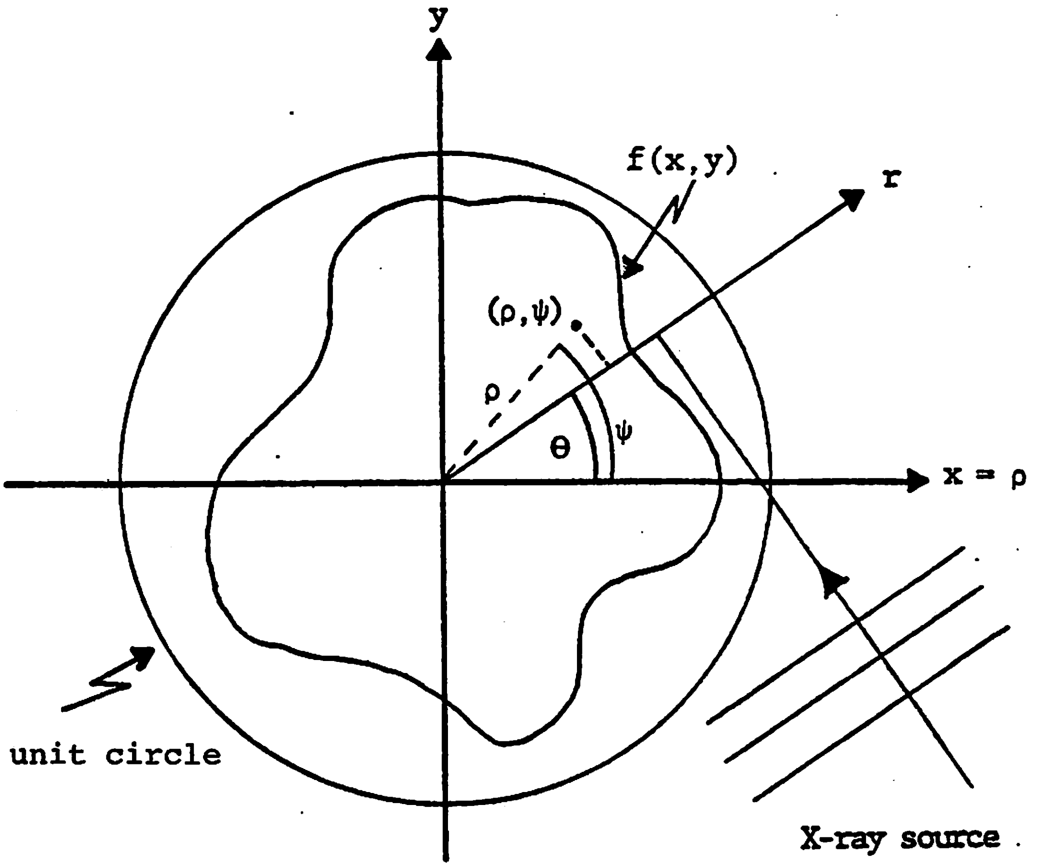

a) CAT imaging configuration $f(\rho,\psi) \xrightarrow{h(r,\theta;\rho,\psi)} g(\gamma,\theta)$

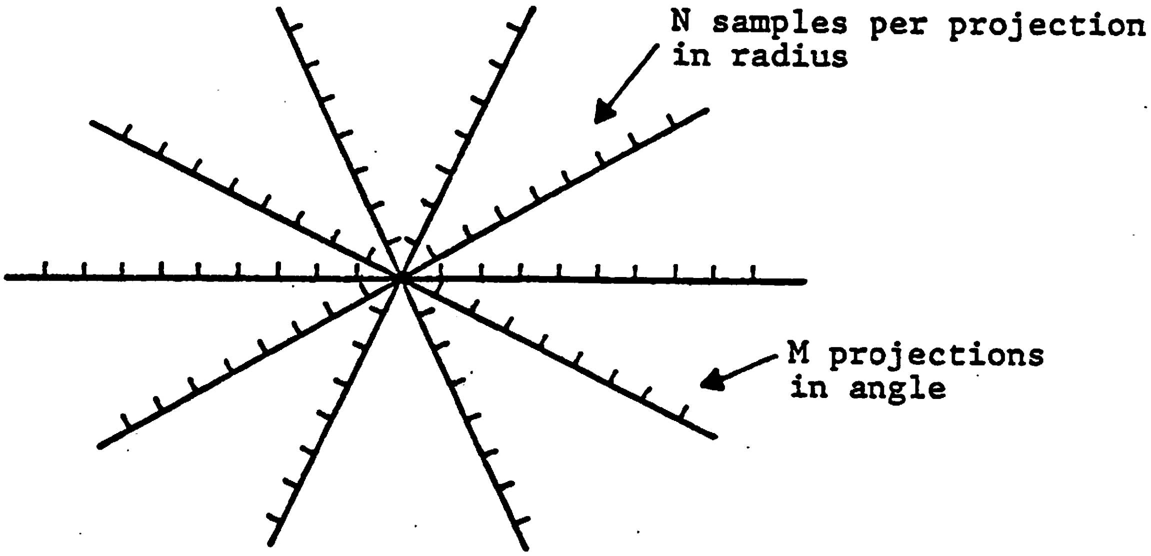

b) Data necessary for reconstruction

Fig. 2-4. CAT scanners

or

$$h(r,\theta;\rho,\psi) = h(\rho\cos(\theta-\psi)-r)$$

where

$$x = \rho\cos\psi$$

$$y = \rho\sin\psi$$

Hence the [H] matrix becomes

$$[H] = \begin{bmatrix} [H]^{(1,1)} & [H]^{(1,2)} & \cdots & [H]^{(1,2)} \\ [H]^{(1,2)} & [H]^{(1,1)} & & [H]^{(1,3)} \\ \vdots & & \ddots & \vdots \\ [H]^{(1,2)} & & \cdots & [H]^{(1,1)} \end{bmatrix} \tag{2-16}$$

where fixed azimuthal steps are assumed and the superscripts denote the azimuth variables. E.g. (i,m) means (θ_i,ψ_m). [H] is circulant in the index (i-m) because of the $(\theta-\psi)$ dependence in the PSF. Note that $\cos(\theta_i-\psi_m) = \cos(\theta_m-\psi_i)$. Because a circulant is a subset of a Toeplitz process we see that this PSF is a member of Case 2, equation (2-5a).

As for the third example, consider the astigmatism and curvature of field studied by Sawchuk [2-14]. The point spread functions behave in a rather complex fashion. Figure 2-6 illustrates the imaging geometry. It can be shown that the point spread function assumes the form

$$h(x_r,x_\theta;u_r,u_\theta) = \frac{1}{D(2C+D)u_r^4} ,$$

$$\frac{[x_r\sin(x_\theta-u_\theta)]^2}{D^2R^2u_r^4} + \frac{[x_r\cos(x_\theta-u_\theta)-u_r]^2}{(2C+D)^2u_r^4R^2} \leq 1 \qquad (2\text{-}17a)$$

$$h(x_r,x_\theta;u_r,u_\theta) = 0, \quad \text{otherwise}$$

where

C: degree of astigmatism

D: degree of field curvature

R: radius of a circular exit pupil.

A close examination of Eq. (2-17a) shows that it can be rewritten as

$$h(x_\theta,x_r;u_\theta,u_r) = h(x_\theta-u_\theta,x_r;u_r) \qquad (2\text{-}17b)$$

or in our discrete numeric notation

$$h(i,k;p,q) = h(i-p,k;q)$$

In the above formulation it should be noted that for no field curvature (D=0) and therefore only astigmatism, the point spread function becomes

$$h_a(x_\theta,x_r;u_\theta,u_r) = \frac{[4C^2R^2u_r^4-(x_r-u_r)^2]^{\frac{1}{2}}}{2C^2u_r^4} ,$$

$$u_r-2CRu_r^2 \leq x_r \leq u_r+2CRu_r^2$$

and zero elsewhere, which is separable and a one dimensional blur along (x_r, u_r).

Case 3: Nonseparate space invariant

This situation occurs most frequently in traditional linear space invariant optical imaging systems. The concepts of coherent transfer functions (CTF), optical transfer functions (OTF), and modulation transfer functions (MTF) all exist in this category of imaging situation. As an example consider the OTF for a diffraction limited system with circular exit pupils given in Figure 2-5. Goodman [2-10] has shown that the imaging equation are given by

$$g(x,y) = \iint_{-\infty}^{\infty} f(\xi,\eta) h(x-\xi, y-\eta) d\xi d\eta \qquad (2\text{-}18)$$

for a circular pupil function with diameter ℓ,

$$h(x-\xi, y-\eta) = \text{circ}\left\{ \sqrt{\frac{(x-\xi)^2 + (y-\eta)^2}{\ell/2}} \right\} \qquad (2\text{-}19a)$$

and in the notation of the previous section

$$h(i,k;p,q) = \text{circ}\left\{ \sqrt{\frac{(i-p)^2 + (k-q)^2}{\ell/2}} \right\} \qquad (2\text{-}19b)$$

Such an imaging system has a PSF matrix with (2M-1)(2N-1) degrees of freedom arranged in a block Toeplitz fashion. As mentioned earlier, approximations to such block Toeplitz forms with block circulant forms results in the use of fast Fourier transform processing [2-7].

Case 4: Separate space variant

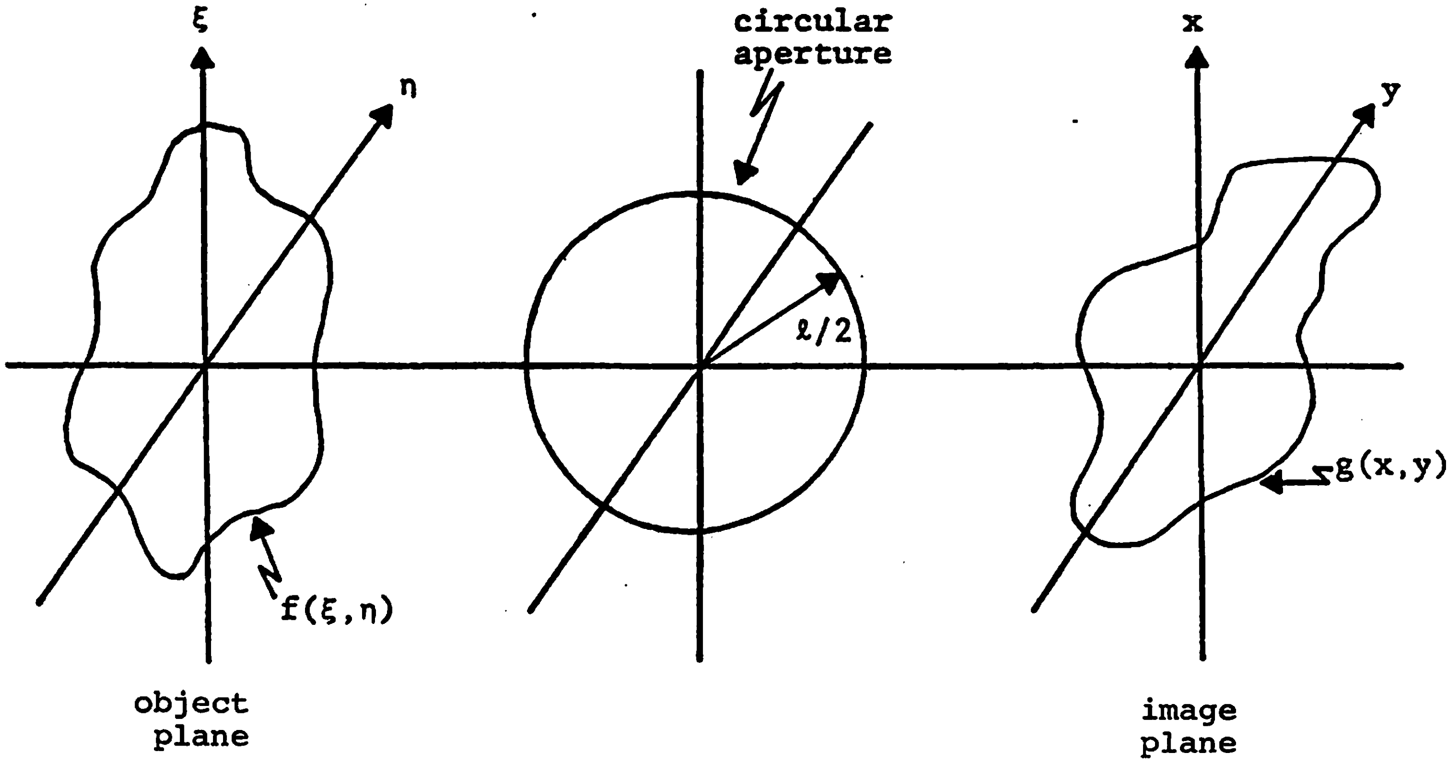

Fig. 2-5. Diffraction limited OTF

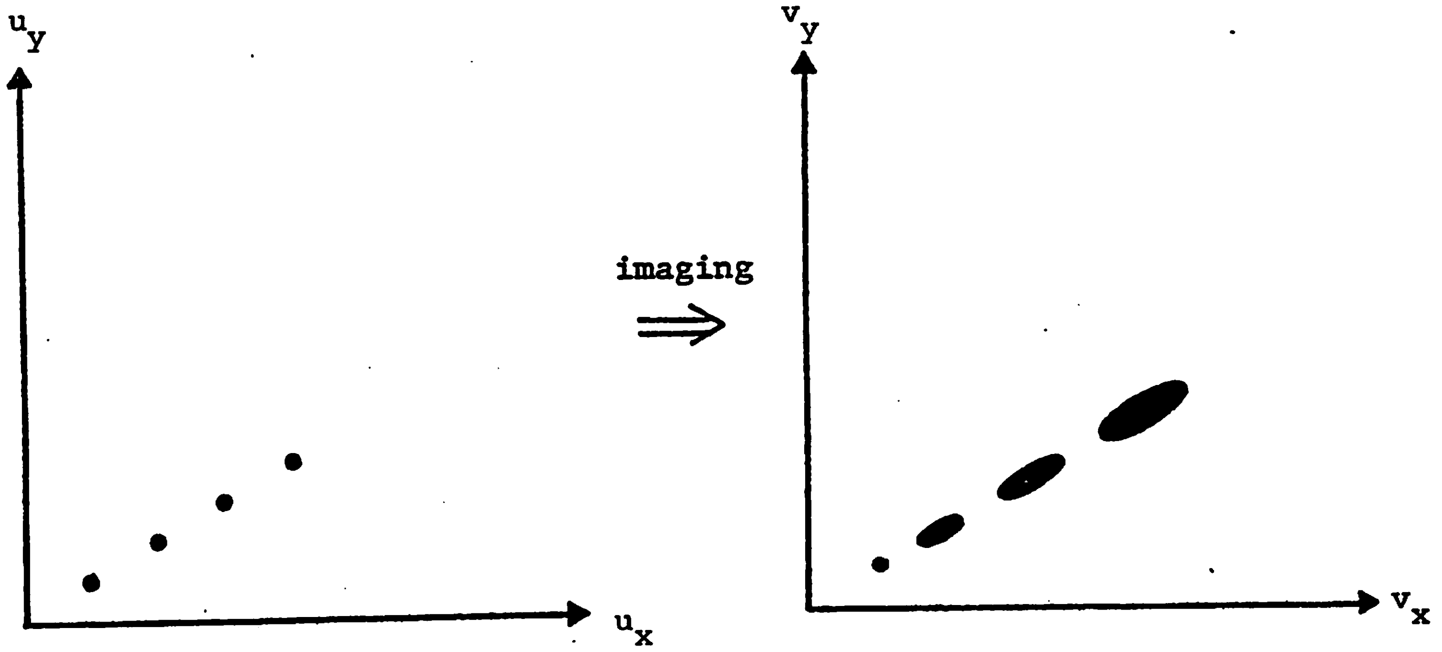

$$\begin{cases} u_x = u_r \cos u_\theta \\ u_y = u_r \sin u_\theta \end{cases} \qquad \begin{cases} v_x = x_r \cos x_\theta \\ v_y = y_r \sin x_\theta \end{cases}$$

Fig. 2-6. Astigmatism and curvature of field

No meaningful examples come to the minds of the author. Interested readers are invited to contribute to this illustration with examples from their own experience.

Case 5: Separate space invariant in one dimension

This class of imaging systems has examples from pushbroom sweep arrays (as in ERTS and LANDSAT data) and SAR radar imaging configurations. Proceeding with the radar example, referring back to Figure 2-3 we see that the effect of range curvature caused the SAR model to be nonseparate. However, if our geometry and requirement is such that the range curvature effect is negligible, then our point spread function becomes decoupled [2-9,2-11,2-12] and

$$h(x_2,t;x_1,y_1) = h_N(t;y_1)h_M(x_2-x_1/y_1) \qquad (2\text{-}20a)$$

$$= \exp(j\omega_o t)A(x_1-x_2,y_1,z_2)f_s\left(t-\frac{2}{c}\left(y_1^2+z_2^2\right)^{\frac{1}{2}}\right)$$
$$\exp\left\{-j\omega_c\frac{2}{c}\left((x_1-x_2)^2+y_1^2+z_2^2\right)^{\frac{1}{2}}\right\} \qquad (2\text{-}20b)$$

which will be repeated as Eq. (4-12) in chapter 4. In this situation with N samples in time (range) and M samples in azimuth, we obtain $(2M-1)N+N^2$ degrees of freedom (see Table 2-2). While this system is "separate" it is nonseparable. This means that the order of the processing is still important. Specifically, one should process the range data first and then process the azimuth data in the image reconstruction effort. The azimuth processing is a function of range which explains the conditioning on y_1 in equation (2-20) and the need for the conical lens in optical reconstruction of SAR imagery. (See for instance Goodman [2-10], Harger [2-11], and Rihaczek [2-13]).

Case 6: Separate space invariant in both dimension

Two examples are presented for this case, an astigmatic processor from Goodman [2-10] and rotational motion blur from Sawchuk [2-15]. Figure 2-7 presents the optical chain for the astigmatic processor. The imaging equation is

$$g(x_3,y_3) = \iint f(x_1,y_1)h(x_3-x_1)\delta(y_3-y_1)dx_1dy_1 \qquad (2\text{-}21)$$

This is an astigmatic process in one dimension only. Likewise, a two-dimensional (sequential) astigmatic process is a straightforward extension.

The second example for this case is that of rotational motion blur as illustrated in Figure 2-8. Here the blur is greater the further away from the origin. The blur is an angular spreading in θ resulting in an imaging system of

$$g(r,\theta) = \iint f(\rho,\phi)h(\rho,\phi;r,\theta)\rho d\rho d\phi \qquad (2\text{-}22a)$$

where

$$h(\rho,\phi,r,\theta) = \frac{1}{\rho}h_\theta(\theta-\phi)\delta(\rho-r) \qquad (2\text{-}22b)$$

and the factor $1/\rho$ is due to the nonuniform rotational speed. In terms of the polar coordinate system (ρ,ϕ) into (r,θ), the imaging system is a blurring along θ only and is

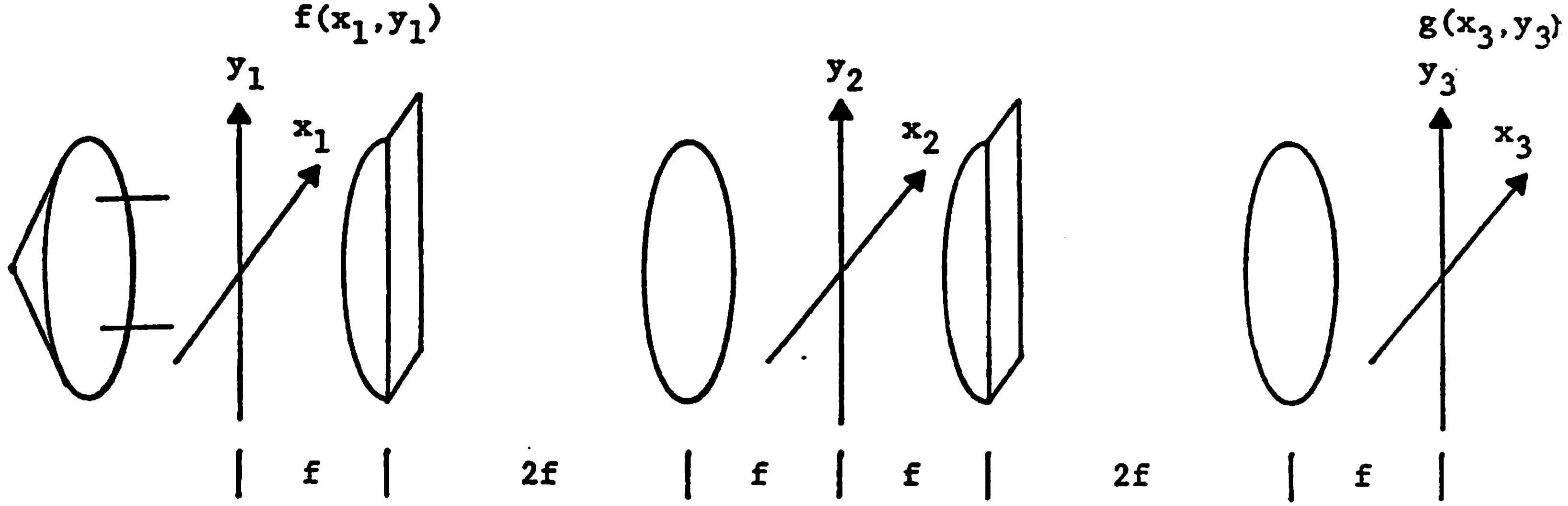

Fig. 2-7. Astigmatic processor

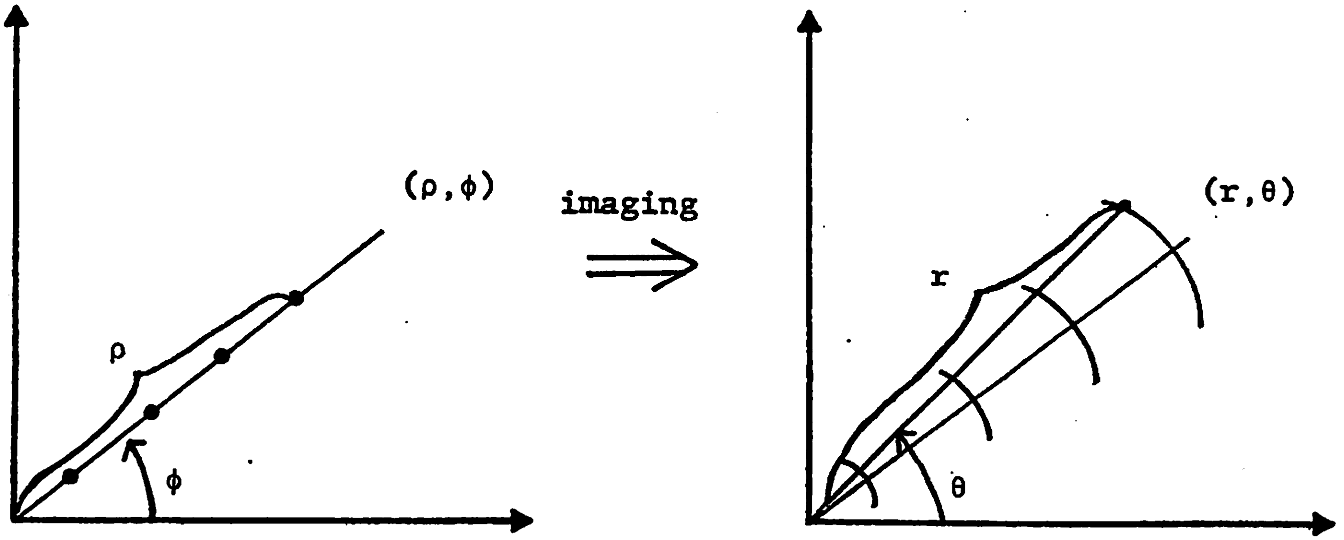

Fig. 2-8. Rotational motion blur

two dimensionally invariant. However, in terms of coordinate system $(\rho,\rho\phi)$ into $(r,r\theta)$ which has a Jacobian of unity with respect to the rectangular coordinate system, the system is invariant along the mapping from $\rho\phi$ to $r\theta$, but changes its form as the other coordinate ρ or r changes. Intuitively the points farther away from the origin are subject to more blur as a result of nonuniform rotational velocity which results in a nonseparable blurring in accordance with our definition.

Case 7: Separable space variant

Separable space variant processes occur quite frequently in digital computation simply as a convenience for computational simplicity. Thus two dimensional unitary transforms for image coding fall into this example. However more relevant imaging situations in this category include imaging lenses with square apertures and the Fourier transforming properties of lenses themselves.

Consider a lens imaging system with square aperture such that $p(x,y) = p_x(x)p_y(y)$ is separable into x and y coordinate and magnification factor $m \neq -1$. Goodman [2-10] has shown this system to have a PSF (see Figure 2-9) in coherent light of

$$h(x_i,y_i,x_0,y_0) = \frac{1}{\lambda^2 d_0 d_i} \iint p(x,y) \exp\left\{-j\frac{2\pi}{\lambda d_i}(x_i+Mx_0)x+(y_i+My_0)\right\} dxdy \tag{2-23a}$$

$$= \frac{1}{\lambda^2 d_0 d_i} \int p_x(x) \exp\left\{-j\frac{2\pi}{\lambda d_i}(x_i+Mx_0)x\right\}dx$$

$$\int p_y(y) \exp\left\{-j\frac{2\pi}{\lambda d_i}(y_i+My_0)y\right\}dy \qquad \text{(2-23b)}$$

$$= h_x(x_i;x_0)h_y(y_i;y_0) \qquad \text{(2-23c)}$$

Note that when M=-1 we obtain Class 9 imaging.

As a second example, consider the Fourier transforming properties of lenses. Figure 2-10 presents the optical system for this illustration. Here the output image (i.e., the Fourier transform of the object) is given by

$$g(x_f,y_f) = \frac{A}{j\lambda f}\iint f(x_0,y_0) \exp\left\{-j\frac{2\pi}{\lambda f}(x_0x_f+y_0y_f)\right\}dx_0dy_0 \qquad \text{(2-24a)}$$

Consequently

$$h(x_f,y_f;x_0,y_0) = \frac{A}{j\lambda f}\exp\left\{-j\frac{2\pi}{\lambda f}x_0x_f\right\}\exp\left\{-j\frac{2\pi}{\lambda f}y_0y_f\right\} \qquad \text{(2-24b)}$$

$$= h_x(x_0,x_f)h_y(y_0,y_f) \qquad \text{(2-24c)}$$

Case 8: Separable space invariant in one dimension

For this case we return to our SAR stripping mode radar and make some additional simplifying assumptions. If the difference of y_{1max} and y_{1min} on the ground (Figure 2-3) is fairly small, then let y_{1n} be the nominal value of y_1 in $h_M(x_2-x_1/y_1)$ of Eq. (2-20a) and after some manipulations we obtain [2-9]

$$h(x_2,t;x_1,y_1) = h_N(t;y_1)h_M(x_2-x_1) \qquad \text{(2-25a)}$$

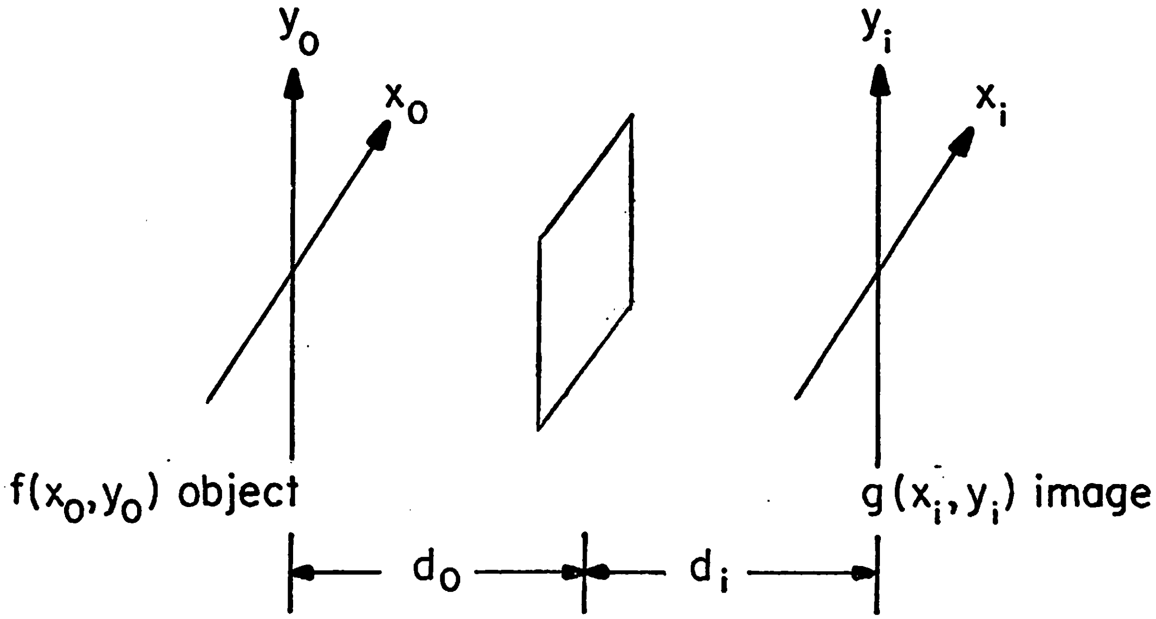

Fig. 2-9. Square aperture magnification

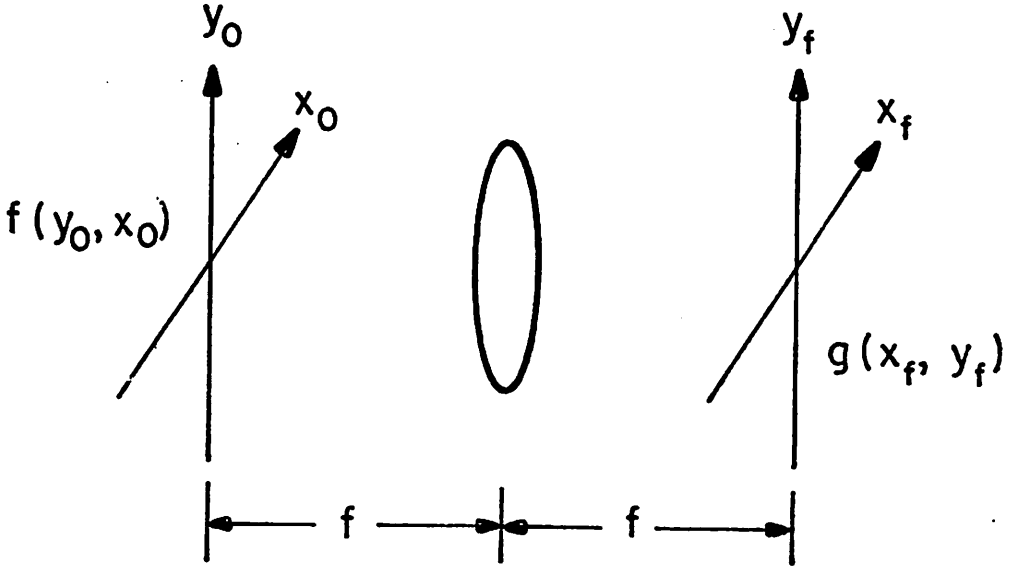

Fig. 2-10. Fourier transforming properties of lenses

where

$$h_N(t;y_1) = \exp\{j\omega_o t\} f_s\left(t-\frac{2}{c}(y_1+z_2^2)^{\frac{1}{2}}\right) \tag{2-25b}$$

$$h_M(x_2-x_1) = A(x_1-x_2,z_2)\exp\left\{-j\frac{2\omega_c}{c}\frac{(x_1-x_2)^2}{(y_{1n}^2+z_2^2)^{\frac{1}{2}}}\right\} \tag{2-25c}$$

Derivations of above Equations can also be found in Chapter 4.

Case 9: Separable space invariant in both dimensions

Pursuing our SAR example, a further simplification of the range offset frequency equal to zero and $y_1^2+z_1^2 \approx y_1^2$ results in the following PSF [2-9]

$$h(x_2,t;x_1,y_1) = h_N\left(t-\frac{2y_1}{c}\right)h_M(x_2-x_1) = h_N(t-t_2)h_M(x_2-x_1) \tag{2-26}$$

where $t_2 \triangleq \frac{2y_1}{c}$.

A second example of a separable space invariant imaging system is a television raster display. The horizontal dimension is electronically filtered (due to the frequency response of the components) and the PSF of the electron gun. The vertical dimension is blurred or "interpolated" by the PSF of the electron guns. Both dimensions are space invariant in a well tuned monitor. The system will be separable if the PSF of the electron gun is separable. This is usually the situation for a Gaussian CRT spot.

The above examples are tabulated in Table 2-4 as a summary. It is clear that many other examples exist, but in the interest of brevity, these will not be presented here.

2.5 Conclusions

This chapter has attempted to present an analysis of the numeric computational aspects of linear imaging systems from the viewpoint of the computational degrees of freedom of such imaging systems. A matrix-lexicographic structure was developed and the DOF_c of the PSF matrix was then analyzed. These degrees of freedom were shown to range from the most complex imaging situations (N^2M^2) down to the simplest imaging systems with $(2N-1)+(2M-1)$ degrees of freedom. The inherent structure of each PSF matrix was analyzed for 9 cases ranging from the most general block structure down to the simplest form of kronecker products of Toeplitz matrices.

Following the section on the analysis of the algebraic structure of each PSF matrix, a set of illustrations from the physical world of imaging systems was developed. Examples from x-ray, radar, coherent, and incoherent optical systems were presented as illustrative material to exemplify the various cases developed in the earlier sections of the chapter. It is hoped that this chapter has aided in the ever growing marriage of computational algorithms and their use for complex image reconstruction. As future imaging systems are developed, it should be possible to utilize the

Case No.	Imaging System	Reference
1	Arbitrarily Complex Imaging System	
2	SAR Stripping Mode with Range Curvature	[2-9],[2-11],[2-12]
	CAT Scanner	[2-4]
	Astigmatism and Curvature of Field	[2-14]
3	OTF,MTF,CTF	[2-5],[2-10]
4	None Presented	
5	Pushbroom Sweep Arrays	
	SAR no Range Curvature	[2-9]
6	Astigmatic Processor	[2-10]
	Rotational Motion Blur	[2-15]
7	Lens with Square Aperture	[2-10]
	Fourier Properties of Lenses	[2-10],[2-16]
8	SAR Stripping Constant Range	[2-9]
9	SAR Stripping Low Altitude	[2-9]
	TV Displays	

Table 2-4. Physical examples of imaging systems for the 9 cases

framework developed here to readily anticipate the complexity of computational reconstruction of imagery once the structure of the PSF matrix is discovered.

Chapter 3

PRINCIPLES OF RADAR IMAGING

3.1 Imaging Systems

The general two-dimensional imaging system, as depicted in Fig. 3-1 is a transformation of the target or object function $f(\xi,\eta)$ into the observation function $g(x,y)$ through a point spread function $h(x,y;\xi,\eta)$, which could be linear or nonlinear and its variables discrete or continuous or a mixture of both [3-1]. The purpose behind the imaging system is to reconstruct or estimate the object function f as close as possible in some sense from the observation g. There are various imaging systems in the real world, e.g. optical, infrared, x-ray, and radar systems; with a wide range of characteristics and limitations, the most conventional one being the passive optical system in which a camera records the reflectivities or transmissivities of the object. In this case relatively little reconstruction effort is required because the point spread function is almost space invariant and in most situations has an impulse-like shape which gives a g closely resembling f as one usually experiences from taking photographic pictures in his daily life. On the other hand, the radar imaging

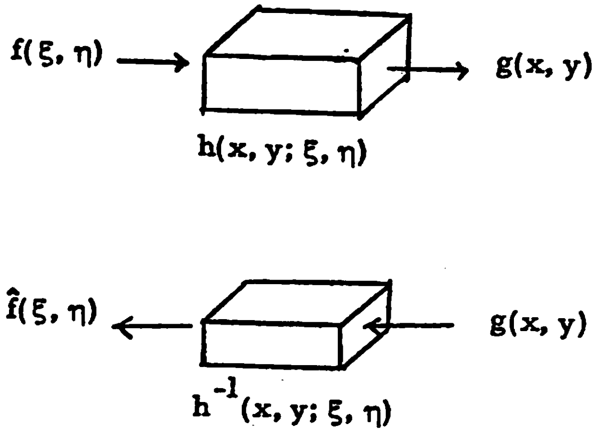

Fig. 3-1. Imaging system and reconstruction

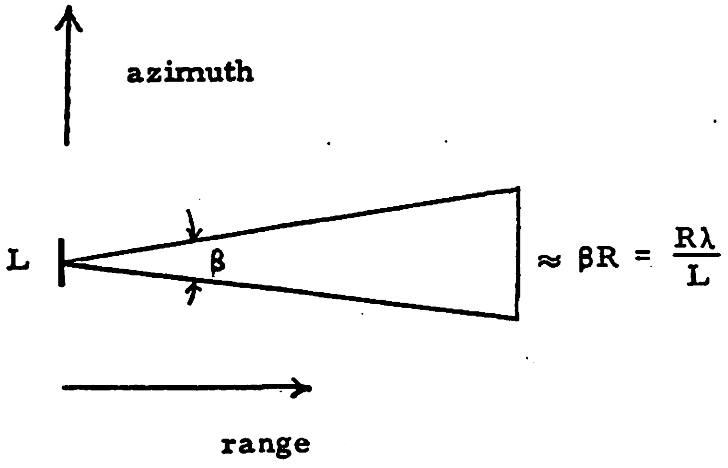

Fig. 3-2. Antenna illumination geometry

system uses an active device to radiate signals whose returns usually have to be processed by complicated procedures to reconstruct the object function.

3.2 Principles of Radar Imaging Systems

There are three major physical parts in a radar system: the transmitter, the receiver and the target. The transmitter, which is required for all active imaging systems, is used to illuminate the target. The receiver is a sensing device which records the signals reflected from the target and is followed or accompanied by a data processing unit. The target is the object some physical properties of which are to be calculated from the received data. In fact the functions of the radar systems can be dichotomized as target detection and parameter estimation. Detection of a target is the determination of its presence in the unavoidably noisy situation, and parameter estimation is the measuring of the characteristics of the targets, e.g. their ranges, velocities, angular positions, sizes, etc. by the extraction of available information from the received echoes when the presence of the targets has been determined or assumed [3-2]. By this token, the radar imaging in which shape and size of the target are of concern belongs to the second category.

In order to reconstruct a radar image of some target from its signal returns, two prerequisites have to be satisfied from the system point of view. First, the returned data has to have a two-dimensional format. Second, radar imaging geometry must be such that the return from each pulse or signature contains different information about the target. In fact, degrees of freedom (DOF) analysis on the radar returns as explored in some detail in this dissertation provides an attempt at evaluating the information-carrying capability of the system by analyzing the extent to which the above conditions are satisfied.

The two geometrical coordinates associated with the radar or the targets in a 2-D radar imaging system are usually called range and azimuth (or cross-range). (In 3-D, there is one more called elevation). Range is the direction along which the radar signal is transmitted, reflected and received. Range information is provided by the return from a single pulse resolved by timing (when a short pulse waveform is used) or range compression technique (when a linear-FM-like waveform is used). Azimuth is the direction orthogonal to the range direction in the surface of interest. It is the component of the relative motion between the radar and target through which an effective target rotation is created.

In the simplest geometry of radar imaging, the processing of the data is separable along the azimuth and the range directions. Although the coupling of the two dimensions has to be taken into account in a complicated radar imaging geometry, this chapter will discuss processing principles when the system is assumed separable and hence decomposable into two consecutive 1-D processes because the understanding of processing principles along individual dimensions is basic to comprehending sophisticated radar imaging systems. In the separable radar imaging systems the operations in the two dimensions could be any combination of incoherent and coherent processing depending on the waveform and antenna pattern used. Incoherent processing assumes incoherence of those signal returns from a single target point and makes no attempts at processing the phase part of the returns, whereby coherent processing uses the phase relations among different returns to "compress" the pulse to achieve high resolutions, as will be explained. We now describe the principles of the four possible operations along the range and the azimuth directions individually.

(A) Incoherent range operation.

The returns of a single pulse from a particular target point are assumed incoherent in phase. Thus no compression technique (as this would require the knowledge of the phase relation) could be applied and the only range resolving ability comes from the actual timing of the strong magnitude pulse return. If τ is the time duration of the pulse then the ideal range resolution ρ_τ will be half the time on target (TOT) of that pulse translated into the spatial domain, i.e.

$$\rho_\tau \approxeq \frac{1}{2} c\tau \qquad (3\text{-}1)$$

where c is the propagation speed of the EM wave. For example, to achieve a range resolution of 1 ft. τ must be less than 2 nanoseconds. Thus for high range resolving ability very narrow pulses have to be used, which requires very high peak powers to keep a sufficiently large signal noise ratio. Obviously the requirements of an extremely short pulse and high peak power could not easily be met from a technical viewpoint as the resolution pursued becomes higher and higher. The main difficulty lies in the fact that the duration of a rectangular pulse is inversely proportional to its bandwidth making a simultaneous large bandwidth and a high SNR very difficult. One way to get around with this conflict is to use phase modulated waveforms which results in what we call a coherent range operation as follows.

(B) Coherent range operation.

In fact, it is the bandwidth B_r, and not the time duration of a pulse waveform that determines the range resolution, i.e.

$$\rho_r \cong \frac{c}{2B_r} \qquad (3\text{-}2)$$

Equation (3-2) is a universal relation which applies to the special case of rectangular waveforms of incoherent range operation. Combining Eqs. (3-1) and (3-2) gives

$$B_r \cdot \tau \cong 1 \qquad (3\text{-}3)$$

for a rectangular pulse with time duration τ and bandwidth B_r and without any phase modulation. The quantity $B_r \cdot \tau$ is called the time-bandwidth product (TBP) which is an indication of the compression capacity of the pulse [2-3].

Coherent range processing uses phase modulation on the transmitted pulses to enlarge its TBP. For example in the case of a linear-FM modulation it can be shown that for large bandwidth the signal bandwidth is proportion to $k \cdot \tau$ where k is the linear FM rate which determines how fast the frequency is changing within a pulse [3-3] and τ is the pulse duration. Thus in contrast to Eq. (3-3) the bandwidth and the pulsewidth are now in proportion to each other and the S/N will not suffer, but benefit instead, from using a larger bandwidth pulse which is accompanied by a longer pulse duration. Other forms of phase modulation are also possible to "stretch" the pulse duration while increasing its bandwidth, but usually the linear FM or chirp modulation is preferred because of its high efficiency in terms of TBP, easy analysis and implementation. Upon receiving the echo of a modulated pulse, the data processor "compresses" or "decodes" it to get high resolution profiles. The resultant de-modulated signal is in the decoded time domain and consists of pulses whose width or resolution is determined by the bandwidth of the transmitted signal and whose locations determined by relative ranges of the target points. The compression ratio, or the ratio between the original pulse duration and the duration of the compressed pulse from a point target, is equal to the TBP in the ideal case [3-3]. An intuitive explanation of the high resolution advantage of a coherent radar processing is as follows: Conceive that the point spread function in the range direction of a radar system is essentially a scaled form of the transmitter signal waveform. Although the linear FM is relatively long in time duration and hence the PSF wide in the range domain, high range resolution is possible because of the high bandwidth of the signal due to the phase modulation.

This is the key point of coherent radar signalling. Hence the simultaneous achievements of a high resolution and a large signal energy are possible by a phase modulated long duration pulse. It is noted that, however, because the transmitted signal is in a coded form (e.g., linear FM modulated), a decoding scheme (e.g., pulse compression) which is a coherent processing, has to be applied upon the received echoes, in contrast to noncoherent processing (simple range grating) for straight short pulse signalling.

The compression or decoding of the return of a linear FM signal from the target can be decomposed into two conceptual steps [3-4]: a quadratic phase removal followed by a Fourier transforming. The former is to compensate for the linear-FM modulation of the signal and the latter is to localize or resolve the various target points.

Because of the strong mathematical similarity between a linear FM signal and the quadratic phase delaying property of the lens [3-8], optical or hologram processing techniques can be used to compress the radar returns and to reconstruct the target images. The analogy between a linear FM waveform and the phase delay of a lens is that both of them are quadratic in phase, with the linear FM rate analogous to the inverse of the focal length of the lens. Thus a lens of suitable focal length (or a conical lens if the focal lengths change in a linear fashion, as described in a later chapter) can be used to remove the quadratic phases associated with the linear FM, followed by a Fourier transforming to complete compressing the signal [3-3].

(C) Incoherent azimuth operation.

Before the development of the synthetic aperture radar (SAR) techniques, incoherent processing was the only way to obtain the azimuthal information of the target by a radar technique. At that time, the traditional imaging radar achieved azimuth resolution by using an antenna with illumination pattern very narrow in azimuth. Physically speaking, the narrower the beam width, the "narrower" the point spread function and thus the better the resolution obtainable. There is no coherent processing necessary along the azimuth direction because the illumination patches are independent azimuthally and no fixed phase relations are maintained among different pulses.

From the antenna theory it is well known that the half power beam width β in radians of a physical antenna of length L is (See Fig. 3-2).

$$\beta = \lambda / L \tag{3-4}$$

Thus fine azimuth resolution (β small) demands a very long physical antenna (L large), not practically available in many situations as higher and higher azimuth resolutions are required in recent years.

(D) Coherent azimuth operation.

From the analysis of the coherent range operation in (B) it can easily be conjectured that a high azimuth resolution could be achieved by phase coding, e.g., a linear FM modulation along the azimuth direction just as in the range direction. However since the object of interest is two dimensional (range and azimuth) while the signal is only one dimensional (a function of time only), and because only one dimensional (i.e., the range) information can be inferred from a pulse return, no explicit phase modulation upon the transmitted signals along the azimuth can be realized. Fortunately, an implicit modulation is made possible by the relative motion of the target and the radar which creates quadratic phase history to each target point in the azimuth direction. In fact, the range history of any rotating target point as a function of the time generates quadratic or linear FM phases for small angle changes as a first order approximation [3-5]. This is the baseline of the principle of synthetic aperture radars (SAR).

The azimuth resolving ability of the SAR can also be explained from the antenna point of view. The radar radiates pulses at different target aspect angles and receives their echoes from the targets shortly after. Because of the relatively short TOT of any pulse it can be assumed that during any single TOT the motion of the targets or the radar is negligible. The returns of different pulses from the same target point are azimuthally modulated by the relative motion between the radar and that particular point. The induced linear-FM returns can be compressed to yield high azimuthal resolution as in the range case. This is analogous to the case of a physical antenna array where the received signals at each array element are coherently processed and summed to yield a sharp effective antenna pattern [3-6]. The analogy between a physical antenna array and a synthetic antenna is depicted in Fig. 3-3.

From Fig. 3-3(b) it is observed that the whole physical azimuthal beam width at range R gives the length of the synthetic aperture available at that range. If L and L_{eff} are the physical and synthetic antenna width along azimuth then

$$L_{eff} \cong R \cdot \beta = \frac{R\lambda}{L} \qquad (3\text{-}5)$$

where β is the physical antenna width in radians. Since the

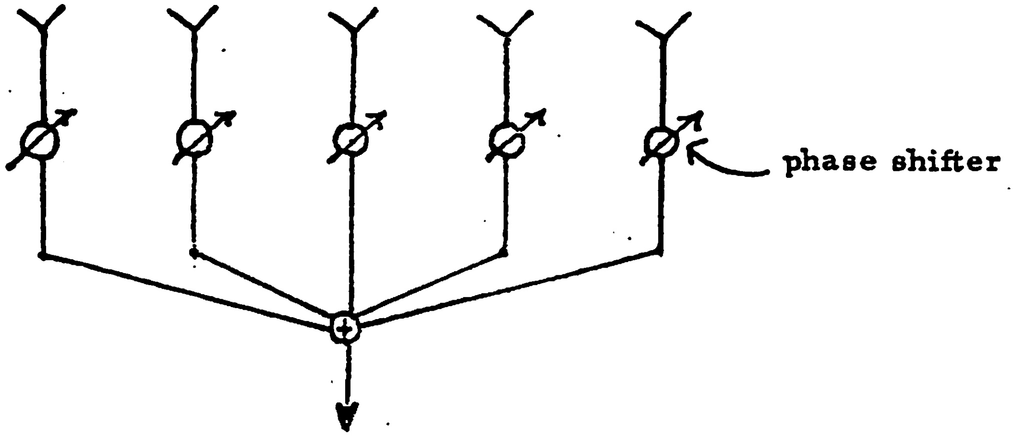

(a) physical antenna array

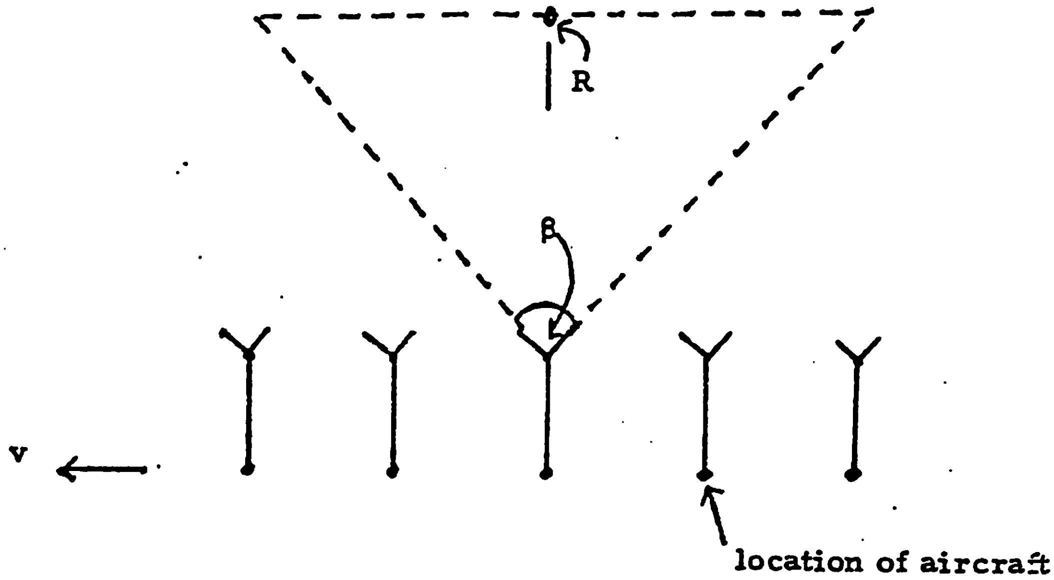

(b) synthetic antenna

Fig. 3-3. Analogy between a physical antenna array and a synthetic antenna operation of SAR utilizes the two-way beam pattern in the sense that the phase shift is introduced on both the paths to and from the targets, the round-trip phase shift effectively reduces the wavelength by a factor of 2. Thus the effective antenna pattern width is, from Eq. (3-1),

$$\beta_{eff} = \frac{\lambda}{2L_{eff}} \tag{3-6}$$

The azimuth resolution ρ_a is the effective beam width projected on the target at range R

$$\rho_a \cong \beta_{eff} R = \frac{L}{2} \tag{3-7}$$

which is proportional to the azimuth size of the physical antenna, and is independent of λ and R. Thus in the SAR to achieve higher azimuth resolution a shorter antenna has to be used, in contrast to a single antenna in a traditional incoherent case as in (C). This is because a smaller antenna has a wider illumination pattern which generates a wider bandwidth available, a characteristic of linear-FM signals [2-7].

3.3 Conclusions

This chapter analyzed one-dimensional radar signal processing principles assuming system separability. In a radar system coherent in both the range and azimuth dimensions, linear FM modulation exists in both dimensions. In the range direction it is created by actually modulating the transmitted waveform whereby in the azimuth direction by an effective rotation of the target. However, the returns are processed in the receiver end by the same compression technique to resolve the target points in both dimensions.

As the analysis goes from one dimensional processing to a two-dimensional one as will be done in the following chapters, new problems could generate many difficulties. Coupling between the two dimensions, e.g. range curvature, range alignment, relative scaling, is a typical example. Also, motion compensation and focusing problems adds the complexity to the system analysis.

System classification and decomposition principles proposed in Chapter 2 will prove very useful tools in the subsequent chapters in obtaining practical and efficient radar image reconstruction procedures under the various imaging geometries.

Chapter 4

SAR STRIPPING MODE

4.1 Introduction

Synthetic aperture radar can map two-dimensional areas with high azimuth resolution achieved by the use of coherent signal processing upon the target point phase histories induced by a relative motion between radar and target. In imaging a large sized target which is usually stationary, e.g., the ground terrain, the radar is carried on a moving vehicle, e.g., an airplane or spacecraft, to get radar echoes from different aspect angles of the target points. Based on the same synthetic aperture principle, there are basically three modes of SAR ground mapping depending on the imaging geometry: spotlight mapping, strip mapping, and Doppler beam-sharpening [4-1,2]. This chapter concerns the stripping mode of SAR terrain imaging which is the most interesting mode having obtained great attention since its birth in early 1950's.

In its operation an airplane or spacecraft flies straight over the ground of interest, radiates pulses at different locations and records the returned echoes. As shown in Fig. 4-1, let (x,y,z) be a rectangular coordinate system with (x,y) being the ground, and assume unless other-

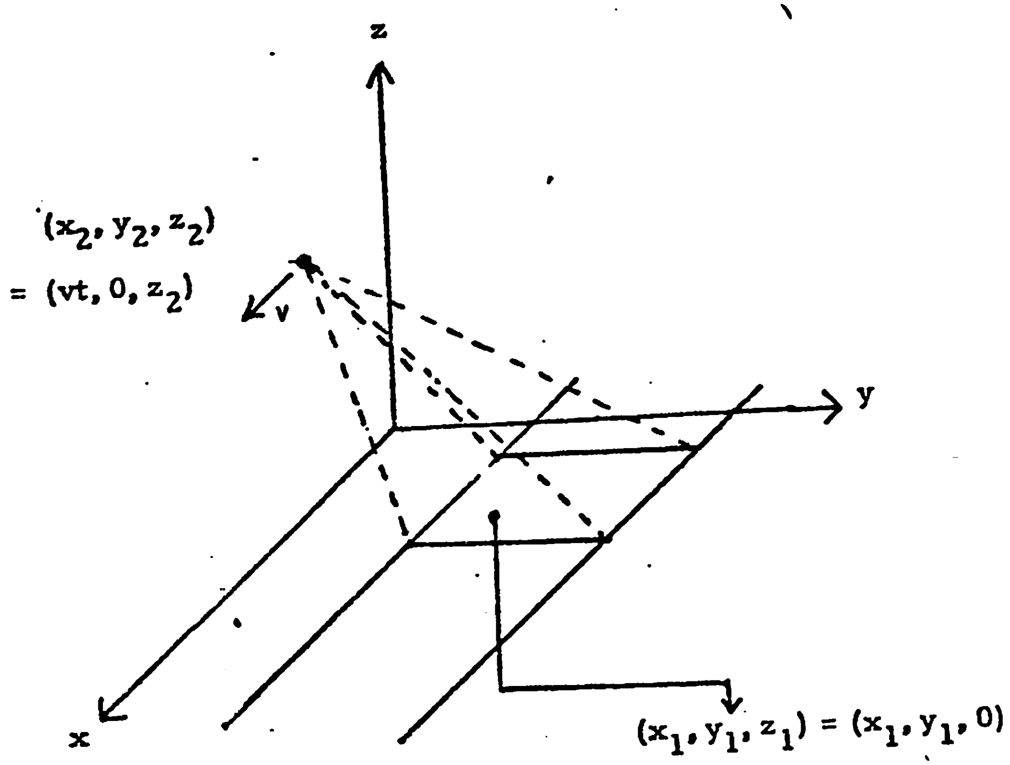

Fig. 4-1. Flight-path geometry of stripping mode

wise stated that the flight is along the x axis, with y=0 and at a constant velocity. For simplicity a side-looking radar is also assumed, although it could as well be squint [4-2]. In the geometry depicted in Fig. 4-1, we use (x_1, y_1, z_1) and (x_2, y_2, z_2) to denote the coordinates of an arbitrary target point and the radar receiver on the aircraft, respectively. We will assume that the effect of the height of mountains and structures on the ground are negligible and that the curvature of the earth surface can be ignored such that $z_1=0$ for all the ground points to be mapped. Furthermore we assume that the time origin coincides with the x origin of the aircraft. Thus $x_2=vt$ where v is the velocity of the aircraft. As is generally the case, the antenna is assumed to be shared by the transmitter and the receiver. This necessitates the pulsed nature of the signal waveform and inevitably creates blind ranges [4-3]. Echoes from targets in blind ranges reach the radar while it is transmitting and not receiving and thus are lost. Also, the pulse repetition frequency (PRF) sets an upper bound to the maximum range without range ambiguities. For simplicity of analysis we assume that the signal pulse train consists of pulses of identical waveform at a constant PRF. Thus let $f_s(t)$ be the modulation function of a single pulse centered at t=0 then the infinite lengthed pulse train wave function will be, in its analytic form,

$$f(t) = \sum_{n=-\infty}^{\infty} f_s(t-nT_s)\exp(j\omega_c t) \qquad (4\text{-}1)$$

where T_s is the pulsing period and ω_c the angular frequency of the carrier. As described in Fig. 4-2, if the "effective" time width of $f_s(t)$ is T_p then the length of the time during which the transmitter is not in use between consecutive pulses is T_s-T_p which decides the maximum range deviation of the radar returns without range ambiguities.

In addition to above timing factors, the depression angle ψ, or the angle between the horizontal plane and the radiated beam, and the antenna pattern are major parameters of the system with its geometry depicted in Figs. 4-3 and 4-4. The point spread function is naturally a complicated expression with many parameters interacting mutually and hence precise image reconstructions demand formidable efforts. However, depending on the degree of accuracy pursued, if we model the PSF of the system in some desirable way by appropriate geometrical considerations and approximations, we will be able to simplify the description of the system, making the system evaluation work the purpose of which will be described in the next section relatively easier and the reconstruction more feasible. Of course, by so doing we inevitably distort the system by using an inexact model, and an incomplete or nonoptimal (in some sense) reconstruction of the target image is to be expected.

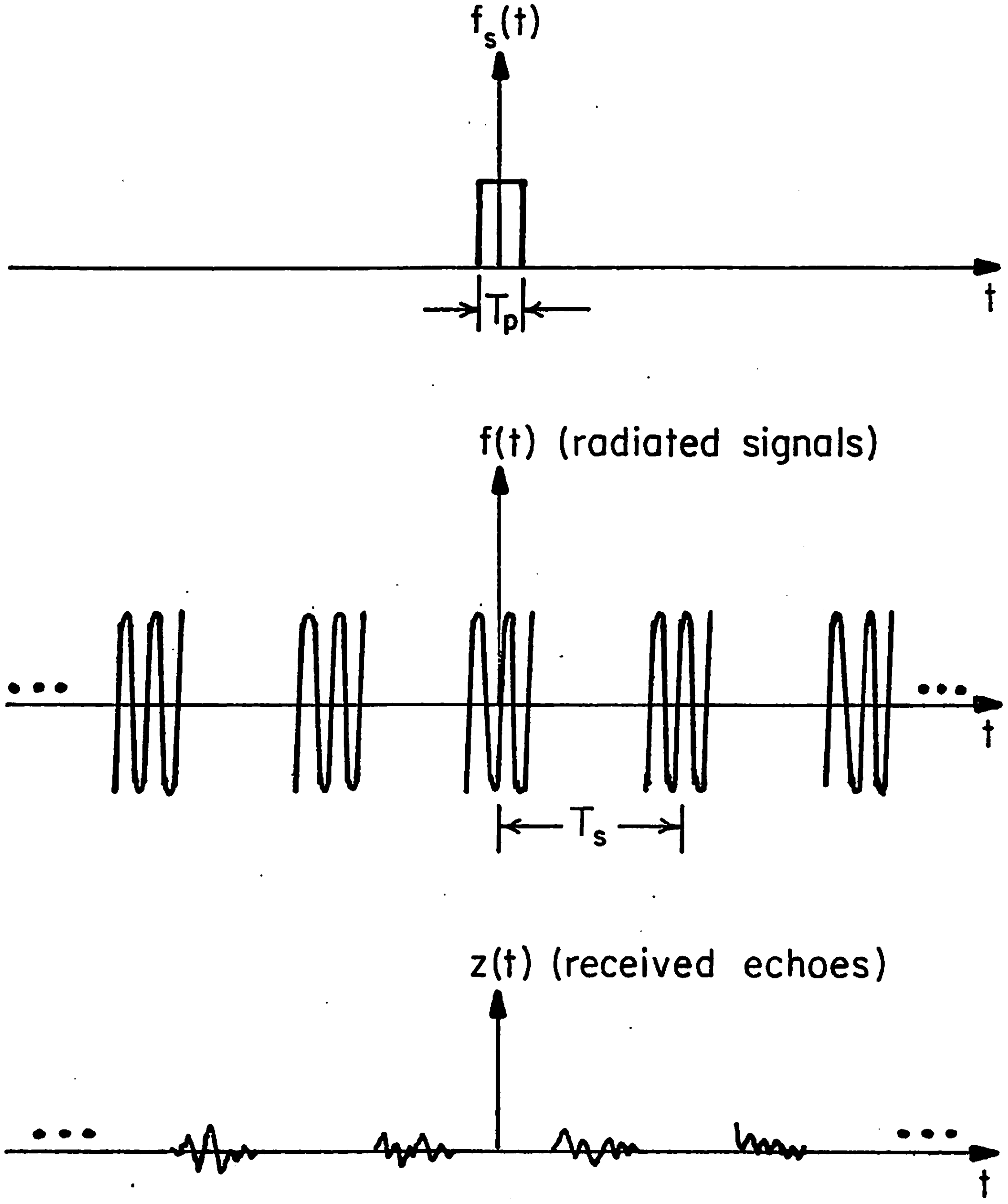

Fig. 4-2. Waveforms of pulsed signals

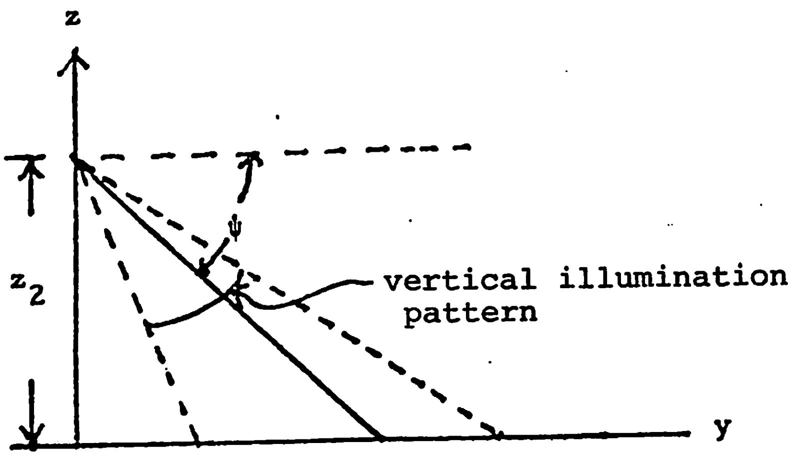

Fig. 4-3. Flight-path geometry on vertical plane

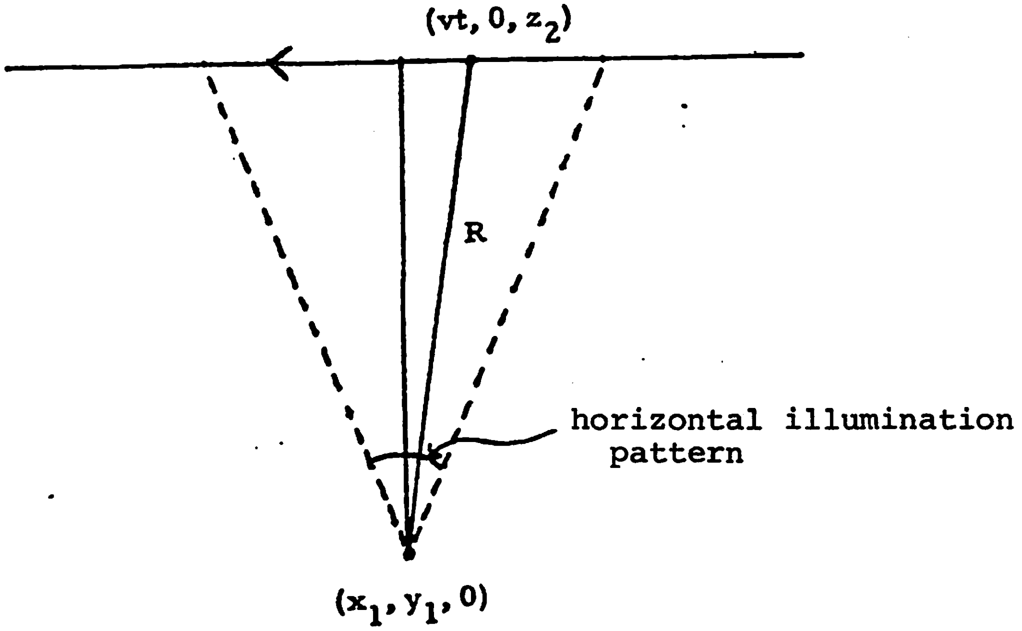

Fig. 4-4. Flight-path geometry on slant range plane

It is obvious that the more approximations one makes, the more degradation will result in the reconstructed image. In this chapter we will give a hierarchy of the SAR system models in progressive inaccuracies. We will show that these models fit the system classification categories in Chapter 2 nicely so that the reconstructions can be done readily by using the appropriate algorithms summarized in Chapter 2. We will also tabulate the approximations made and their justifications at each step. It will be shown that in its simplest form the system is separable and space-invariant.

An imaging system has two kinds of DOF's; one of them is computational (DOF_c) as studied in Chapter 2 and the other is informative (DOF). We now explain the latter and differentiate the two.

4.2 System Evaluation

In general, gathering more data provides more information to solve for the unknowns at the expense of increased requirements in storage and complexity in computation. On the other hand, intuition suggests that after some "threshold amount" of data is obtained, the additional observations do not always provide equal amounts of new information. This is due to the inherent "blurring" of the imaging systems and observation noise, etc. Thus the concept of degrees of freedom (informative DOF) has arisen to measure the number of truly independent samples of data one gathers under a particular imaging system [4-4,5].

In the system evaluation the concept of eigenvalues of a correlation matrix or the Gramian matrix is usually adopted [4-6,4-8]. For example, in the continuous-discrete case, we equate the degrees of freedom with the number of eigenvalues of the Gramian matrix larger than some threshold determined by the noise level of the system. This is equivalent to the singular value analysis of the system. For the purpose which will be clear later we now show that orthogonal transforming the input and/or output data of a linear system will not change its eigenvalue spectrum and hence its system performance, other than a possible reordering of its singular values. Consider the discrete-discrete case for the sake of ease in proof: Let [H] be the matrix of the linear system and [P], [Q] be orthogonal matrices multiplied with the output and input vectors, respectively; $P^tP = PP^t = I$ and $Q^tQ = QQ^t = I$ where the superscript t denotes a transposition. The set of eigenvalues of $PHQ(PHQ)^t = PHQQ^tH^tP^t = PHH^tP^t$ is the same set of eigenvalues of $P^tPHH^t = HH^t$ except for additional zeroes due to possible size difference of P and Q [4-8]. Note that the sets of eigenvalues of PHQ and H differ in general, though.

To differentiate the DOF_c and DOF, we note first that both of them are derived from the system PSF. However, the DOF_c is usually determined before DOF and it needs only the structural information of the PSF and can be determined by identifying the PSF with the simplest case in Chapter 2. The DOF_c is used to determine the amount of effort required to estimate the DOF which requires the actual numeric values of the PSF in the matrix diagonalization manipulation.

4.3 Derivation of Point Spread Function for the SAR Imaging System

Referring to Fig. 4-1, $z_1 = 0$, $x_2 = vt$, $y_2 = 0$ and z_2 is the flight height. Define the ground range

$$\begin{aligned} R_g &\triangleq \left[(x_1-x_2)^2+(y_1-y_2)^2\right]^{\frac{1}{2}} \\ &= \left[(x_1-vt)^2+y_1^2\right]^{\frac{1}{2}} \qquad (4\text{-}2) \end{aligned}$$

and the slant range

$$\begin{aligned} R &= \left[(x_1-x_2)^2+(y_1-y_2)^2+(z_1-z_2)^2\right]^{\frac{1}{2}} \\ &= \left[(x_1-vt)^2+y_1^2+z_2^2\right]^{\frac{1}{2}} \qquad (4\text{-}3) \\ &= \left[R_g^2+z_2^2\right]^{\frac{1}{2}} \end{aligned}$$

The propagation delay associated with a point target at (x_1,y_1,z_1) with range R is $\frac{2R}{c}$ where the factor 2 is because of the round trip of the wave propagation. Let $\rho(x_1,y_1)$ be the reflectivity function of the terrain and $A(x_1,y_1,x_2,z_2)$ be the illuminating intensity of the antenna beam on the terrain point (x_1,y_1) when the receiver is at $(x_2,0,z_2)$. If the antenna pattern remains the same during the flight, it is easily seen that

$$A(x_1,y_1,x_2,z_2) = A(x_1-x_2,y_1,z_2).$$

The received echoes are the product of the illuminating pattern A, the terrain reflectivity ρ and the delayed signal function f, summed over the ground coordinates (x_1,y_1), where the propagation decay has been assumed uniform in the (x_1,y_1) plane and neglected

$$z(t) = \int_{-\infty}^{\infty}\!\!\int A(x_1-x_2,y_1,z_2)\,\rho(x_1,y_1)\,f(t-\tfrac{2R}{c})\,dx_1dy_1 \qquad (4\text{-}4)$$

Substituting Eq. (4-1) into Eq. (4-4),

$$z(t) = \int_{-\infty}^{\infty}\!\!\int A(x_1-x_2,y_1,z_2)\,\rho(x_1,y_1) \sum_{n=-\infty}^{\infty} f_s(t-\tfrac{2R}{c}-nT_s) \exp\left\{j\omega_c(t-\tfrac{2R}{c})\right\} dx_1dy_1 \qquad (4\text{-}5)$$

If we interpret Eq. (4-5) as a two variable to one variable system with $\rho(x_1,y_1)$ as its input and $z(t)$ as its output, it is obvious that the system is linear with point spread function

$$h(t;x_1,y_1) = \sum_{n=-\infty}^{\infty} A(x_1-x_2,y_1,z_2)\,f_s\left(t-nT_s-\frac{2\left[(x_1-x_2)^2+y_1^2+z_2^2\right]^{\frac{1}{2}}}{c}\right) \exp\left\{j\omega_c\left(t-\frac{2\left[(x_1-x_2)^2+y_1^2+z_2^2\right]^{\frac{1}{2}}}{c}\right)\right\} \qquad (4\text{-}6)$$

$$= \exp\{j\omega_c t\}\sum_{n=-\infty}^{\infty} A(x_1-nvT_s,y_1,z_2)\,f_s\left(t-nT_s-\frac{2\left[(x_1-nvT_s)^2+y_1^2+z_2^2\right]^{\frac{1}{2}}}{c}\right)\exp\left\{-j\omega_c\frac{2\left[(x_1-nvT_s)^2+y_1^2+z_2^2\right]^{\frac{1}{2}}}{c}\right\}$$

where $x_2=nvT_s$ is a discrete radar coordinate and it has been assumed that during the transmission and receiving of a single pulse the aircraft is approximately stationary so that x_2 is substituted by nvT_s in Eq. (4-6). This is valid if (sufficient conditions)

a) $A(x_1-nvT_s,y_1,z_2)\approx A(x_1-nvT_s\pm\Delta x_2,y_1,z_2)$

b) $(|x_1-nvT_s|+\Delta x_2)^2-(x_1-nvT_s)^2<<(y_1+\Delta y_1)^2-y_1^2$ and

c) $2\left[(|x_1-nvT_s|+\Delta x_2)^2+y_1^2+z_2^2\right]^{\frac{1}{2}}-2\left[(x_1-nvT_s)^2+y_1^2+z_2^2\right]^{\frac{1}{2}}<<\lambda_c$

for all x_1 and y_1 under illumination, where Δx_2 is the maximum distance the aircraft travelled during the receiving of a single pulse. Δy_1 is the range resolution desired. See Fig. 4-5. Note that $\Delta x_2<vT_s$ as assumed earlier. The above relations assume that the movement of the radar during the receiving of a single pulse is so small that a) illumination pattern is effectively fixed, b) no range walking within one pulse and c) induced phase error is much less than one wavelength, respectively.

(a) is easily satisfied by noting that $L_{eff}=\frac{R\lambda}{L}$ is of the order of hundred or thousand meters, and is therefore greatly larger than Δx_2, which is of the same order of the azimuth resolution desired.

(b) $$(|x_1-nvT_s|+\Delta x_2)^2-(x_1-nvT_s)^2$$
$$= 2\Delta x_2|x_1-nvT_s|+\Delta x_2^2$$
$$\leq 2\Delta x_2(L_{eff}+\Delta x_2) \approx 2\Delta x_2 L_{eff}$$
while

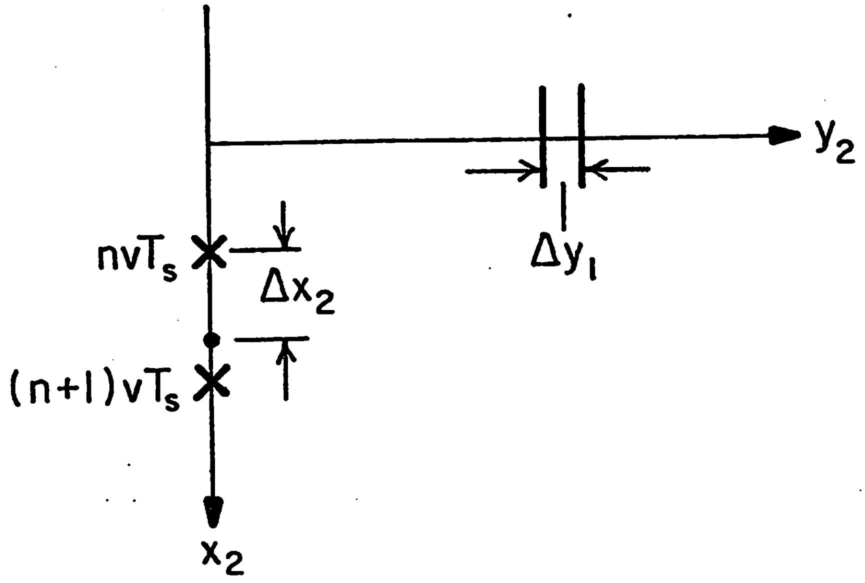

Fig. 4-5. Justification of the stationarity of radar within one pulse time

$$(y_1+\Delta y_1)^2-y_1^2 = 2\Delta y_1\cdot y+\Delta y_1^2 \approx 2\Delta y_1\cdot y$$

Since Δx_2 is of the same order as Δy_1(azimuth resolution vs. range resolution), (b) will be valid if

$$L_{eff} << y_1 \tag{4-7}$$

(c) $$2\left\{\left[(|x_1-nvT_s|+\Delta x_2)^2+y_1^2+z_2^2\right]^{\frac{1}{2}} - \left[(x_1-nvT_s)^2+y_1^2+z_2^2\right]^{\frac{1}{2}}\right\}$$

$$\approx 2\left\{(y_1^2+z_2^2)^{\frac{1}{2}}+\frac{1}{2}\frac{(|x_1-nvT_s|+\Delta x_2)^2}{(y_1^2+z_2^2)^{\frac{1}{2}}} - (y_1^2+z_2^2)^{\frac{1}{2}}-\frac{1}{2}\frac{(x_1-nvT_s)^2}{(y_1^2+z_2^2)^{\frac{1}{2}}}\right\}$$

$$= \frac{2}{(y_1^2+z_2^2)^{\frac{1}{2}}}\,(|x_1-nvT_s|\cdot\Delta x_2+\Delta x_2^2)$$

$$\approx \frac{2|x_1-nvT_s|\cdot\Delta x_2}{(y_1^2+z_2^2)^{\frac{1}{2}}}$$

$$\leq \frac{2L_{eff}\cdot\Delta x_2}{(y_1^2+z_2^2)^{\frac{1}{2}}} << \Delta x_2$$

where validity of Eq. (4-7) has been assumed. Thus if we let Δx_2 be of the same order as λ_c, (c) will be satisfied. In fact, the achievable azimuth resolution is of the same order as λ_c [4-11].

Because the sinusoidal phase term $\exp\{j\omega_c t\}$ in Eq.(4-6) does not carry any information on $\rho(x_1,y_1)$, a preprocessing can shift it to any lower frequency ω_o desired. In optical processing upon SAR data, the "offset" frequency $\omega_o\neq 0$ is to separate reconstructed twin images from each other and from other useless images [4-9,10].

Thus,

$$
\begin{aligned}
h(t;x_1,y_1) = \exp\{j\omega_o t\} \sum_{n=-\infty}^{\infty} & A(x_1-nvT_s,y_1,z_2) \\
& f_s\left(t-nT_s-\frac{2\left[(x_1-nvT_s)^2+y_1^2+z_1^2\right]^{\frac{1}{2}}}{c}\right) \\
& \exp\left\{-j\omega_c\frac{2\left[(x_1-nvT_s)^2+y_1^2+z_2^2\right]^{\frac{1}{2}}}{c}\right\} \qquad (4\text{-}8)
\end{aligned}
$$

Although the return of the pulse train from the two dimensional target field is one dimensional - i.e., function of t only, the recording of data is usually two dimensional. For example, because of its huge capability for 2-D data storage, film has been widely used for SAR data recording. This is conveniently done for latter processing because the signal returns from different pulses do not overlap in time. The returns of each transmitted pulse are arranged side by side as in Fig. 4-6(b) in which the data lines are contained between 0 and T_s in the new t axis and extends along the flight path axis x which is perpendicular to the t axis. Equivalently, the original one dimensional t axis denoting the data collecting time is transformed into two dimensions, discrete x_2 and continuous t. Because the coordinate transformation above is a reordering of the data which is an orthogonal transformation, nothing has been changed from a DOF point of view from the analysis in section 4.2.

Now $S(x_2,t)$ is nonzero only for $0 \leq t \leq T_s$ and x_2 is a discrete variable occuring at nvT_s only. Note that x_2 and t, which are the variables in the data domain, have dimen-

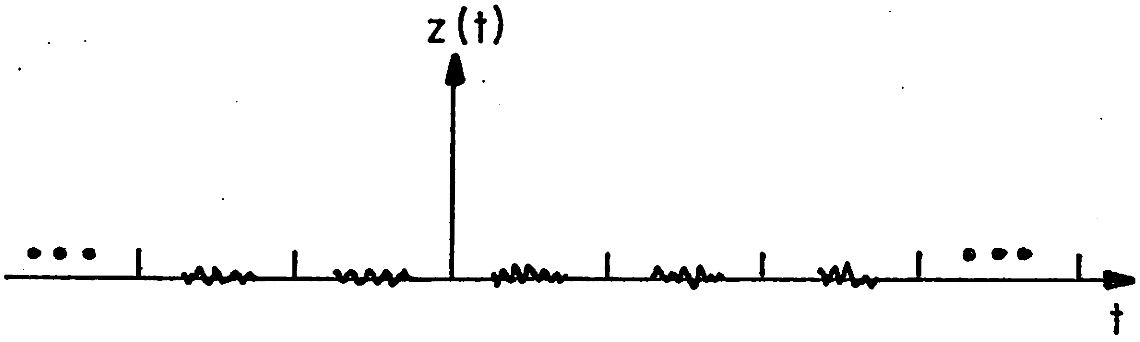

(a) received signal

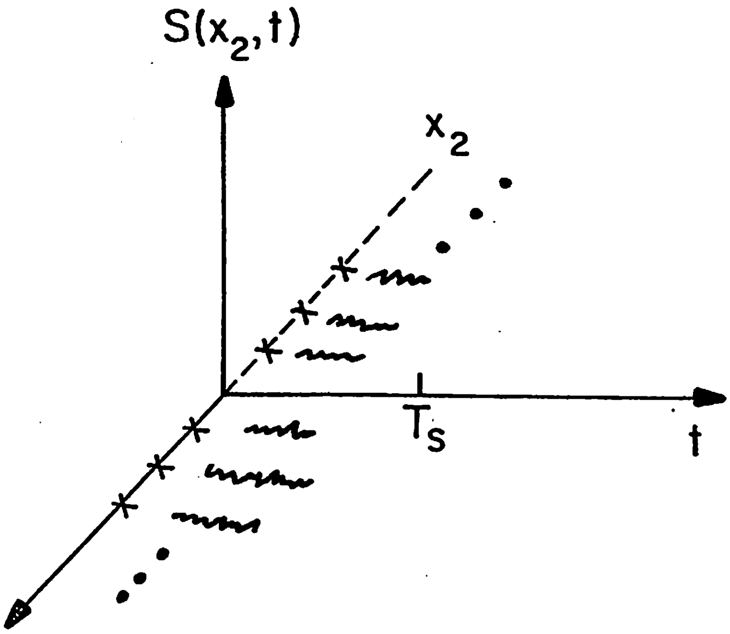

(b) reordering of (a)

Fig. 4-6. Reordering of received signal

sions of length and time, respectively.

The PSF expressed in (x_2,t) variables now becomes

$$h(x_2,t;x_1,y_1) = \exp\left[j\omega_0(t+nT_s)\right]A(x_1-x_2,y_1,z_2)$$
$$f_s\left(t-\frac{2\left[(x_1-x_2)^2+y_1^2+z_2^2\right]^{\frac{1}{2}}}{c}\right)$$
$$\exp\left\{-j\omega_c\frac{2\left[(x_1-x_2)^2+y_1^2+z_2^2\right]^{\frac{1}{2}}}{c}\right\} \qquad (4\text{-}9)$$

where $0 \leq t \leq T_s$, $x_2 = nvT_s$.

Eq. (4-9) can easily be identified with the kernel of a two-dimensional transformation, ω_0, ω_c, v, T_s, z_2, c, A and f_s being parameters. Sometimes it is desirable that the data obtained from the system kernel Eq. (4-9) be multiplied with $\exp(-j\omega_0 nT_s) = \exp(-j\omega_0\frac{x_2}{v})$, or $\exp(-j\omega_0 t)$ yielding range offset case and azimuth offset case, respectively [4-12]. Although the multiplication is not necessarily an orthogonal transformation and thus would affect the true DOF of the imaging system, the exact effect on the DOF will not be investigated here. As will be explained in Chapter 7 this is one of the preprocessors designed to make subsequent processings or presentation easier. The offset data has equivalent kernels

$$h(x_2,t;x_1,y_1) = \exp(j\omega_0 t)A(x_1-x_2,y_1,z_2)$$
$$f_s\left(t-\frac{2\left[(x_1-x_2)^2+y_1^2+z_2^2\right]^{\frac{1}{2}}}{c}\right)\exp\left\{-j\omega_c\frac{2\left[(x_1-x_2)^2+y_1^2+z_2^2\right]^{\frac{1}{2}}}{c}\right\}$$

range offset case (4-10)

$$h(x_2,t;x_1,y_1) = \exp\left(j\frac{\omega_0}{v}x_2\right)A(x_1-x_2,y_1,z_2)$$
$$f_s\left(t-\frac{2\left[(x_1-x_2)^2+y_1^2+z_2^2\right]^{\frac{1}{2}}}{c}\right)\exp\left\{-j\omega_c\frac{2\left[(x_1-x_2)^2+y_1^2+z_2^2\right]^{\frac{1}{2}}}{c}\right\}$$

azimuth offset case (4-11)

In the following analysis we shall assume that the range offset case is used.

4.4 Simplification of PSF

In this section we try to simplify the PSF (Eq. (4-10)) of the SAR imaging system from several physical considerations. Along with the simplifications, a hierarchy of models of PSF's with decreasing complexity will be derived along with their associated assumptions and approximations.

We start by noting the strong relations between variables x_1 and x_2, y_1 and t, respectively: in Eq. (4-10), the argument of f_s, $t-\left[2\left[(x_1-x_2)^2+y_1^2+z_2^2\right]^{\frac{1}{2}}\right]/c$, were it not for the factor $(x_1-x_2)^2$, would yield a simple one dimensional relation which connects y_1 with t to provide the range information independent of azimuth modulation. This is the only way which makes $h(x_2,t;x_1,y_1)$ nonseparate in azimuth and range in Eq. (4-10). If this fact can be ignored, e.g., if the propagation delay induced by the variation in (x_1-x_2) is much smaller than the range resolution interested, then the PSF can be considered separate in azimuth (from x_1 to x_2) and range (from y_1 to t):

$$h(x_2,t;x_1,y_1) = \exp(j\omega_0 t)A(x_1-x_2,y_1,z_2)\, f_s\!\left(t-\frac{2(y_1^2+z_2^2)^{\frac{1}{2}}}{c}\right)\exp\left\{-j\omega_c\frac{2\left[(x_1-x_2)^2+y_1^2+z_2^2\right]^{\frac{1}{2}}}{c}\right\} \tag{4-12}$$

Physically this means that the range resolution cells under antenna illumination do not move to overlap each other as the flight continues. The situation is depicted in Fig. 4-7, where the range γ of a target point is plotted as a function of the azimuth distance x_1-x_2 of that point. Various ways have been proposed to alleviate the problem of range-azimuth coupling [4-13,14,15] where the range curvature is not to be ignored. However, if ρ_r is the range resolution pursued and β the effective beam width then this range curvature will be negligible if

$$\left|\left[(x_1-x_2)^2+y_1^2+z_2^2\right]^{\frac{1}{2}}-(y_1^2+z_2^2)^{\frac{1}{2}}\right| \le \rho_r$$

for all x_1-x_2 and y_1 illuminated by the radar. Assuming $(x_1-x_2) << (y_1^2+z_2^2)^{\frac{1}{2}}$ as in Eq. (4-7) and β small, we have

$$\begin{aligned}\left[(x_1-x_2)^2+y_1^2+z_2^2\right]^{\frac{1}{2}}-(y_1^2+z_2^2)^{\frac{1}{2}} &\approx (y_1^2+z_2^2)^{\frac{1}{2}}+\frac{1}{2}\frac{(x_1-x_2)^2}{(y_1^2+z_2^2)^{\frac{1}{2}}}-(y_1^2+z_2^2)^{\frac{1}{2}}\\ &= \frac{1}{2}\frac{(x_1-x_2)}{(y_1^2+z_2^2)^{\frac{1}{2}}}\\ &\le \frac{1}{8}\,\frac{L_{eff}^2}{(y_1^2+z_2^2)^{\frac{1}{2}}}\\ &\approx \frac{\beta}{8}\,L_{eff}\end{aligned}$$

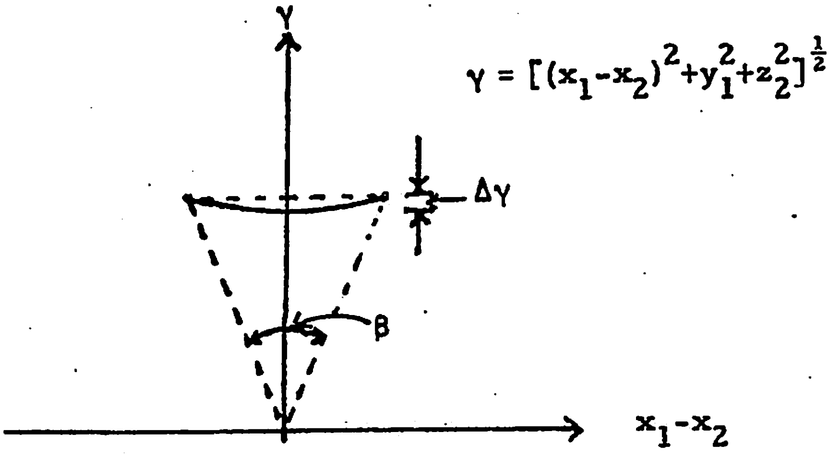

Fig. 4-7. Range variation of a point target

So we require that

$$\rho_r > \frac{\beta}{8} L_{eff} \tag{4-13}$$

for negligible range curvatures. I.e., PSF can be approximated by Eq. (4-12), which is separate in azimuth and range, if the inequality (4-13) holds.

To see that the system with kernel Eq. (4-12) is separate in azimuth and range, we rewrite Eq. (4-12) as

$$h(x_2,t;x_1,y_1) = \exp(j\omega_0 t) f_s \left(t - \frac{2(y_1^2+z_2^2)^{\frac{1}{2}}}{c}\right)$$

$$A(x_1-x_2,y_1,z_2) \exp\left\{-j\omega_c \frac{2\left[(x_1-x_2)^2+y_1^2+z_2^2\right]^{\frac{1}{2}}}{c}\right\}$$

$$= h_t(t;y_1) h_z(x_2;x_1,y_1) \tag{4-14}$$

where $h_t(t;y_1) \triangleq \exp(j\omega_0 t) f_s\left(t-\frac{2(y_1^2+z_2^2)^{\frac{1}{2}}}{c}\right)$ is the response of a unit point source (impulse response) at y_1, which is independent of azimuth dimension; and

$$h_z(x_2;x_1,y_1) \triangleq A(x_1-x_2,y_1,z_2) \exp\left\{-j\omega_c \frac{2\left[(x_1-x_2)^2+y_1^2+z_2^2\right]^{\frac{1}{2}}}{c}\right\}$$

is the azimuth response of a unit point source at (x_1,y_1). Note that $h_z(x_2;x_1,y_1) = h_z(x_1-x_2;y_1)$ is space invariant in x_1 and x_2, but varies its form as y_1 changes. If we use Eq. (4-14) as the kernel of the SAR, then the input-output relation will be

$$z(x_2,t) = \int\int_{-\infty}^{\infty} h_t(t;y_1)h_z(x_1-x_2;y_1)\rho(x_1,y_1)dx_1dy_1$$

$$= \int_{-\infty}^{\infty} h_t(t;y_1)\left[\int_{-\infty}^{\infty} h_z(x_1-x_2;y_1)\rho(x_1,y_1)dx_1\right]dy_1 \tag{4-15}$$

Thus equivalently the imaging system of SAR is a transformation of $\rho(x_1,y_1)$ into $z(x_2,t)$ in a sequential order: azimuth transformation followed by range transformation. Because of the dependence of h_z upon y_1, h_t and h_z are not separable and thus their order cannot be interchanged in modelling the system. Accordingly, the reconstruction of the ground reflectivity function $\rho(x_1,y_1)$ from its image $z(x_2,t)$ has to follow the reversed order.

To put Eq. (4-14) in a more practical form, we note from inequality (4-7) that $|x_1-x_2| << y_1^2+z_2^2$ and hence

$$\exp\left\{-j\omega_c\frac{2\left[(x_1-x_2)^2+y_1^2+z_2^2\right]^{\frac{1}{2}}}{c}\right\}\approx\exp\left\{-j\omega_c\frac{2(y_1^2+z_2^2)^{\frac{1}{2}}+\frac{(x_1-x_2)^2}{(y_1^2+z_2^2)^{\frac{1}{2}}}}{c}\right\}$$

$$= \exp\left\{-j\omega_c\frac{2(y_1^2+z_2^2)^{\frac{1}{2}}}{c}\right\}\exp\left\{-j\omega_c\frac{(x_1-x_2)^2}{(y_1^2+z_2^2)^{\frac{1}{2}}}\right\} \tag{4-16}$$

and thus $h_z(x_2;x_1,y_1)$ can be approximated by

$$h_z(x_2;x_1,y_1) \approx \exp\left\{-j\omega_c\frac{2(y_1^2+z_2^2)^{\frac{1}{2}}}{c}\right\}A(x_1-x_2,y_1,z_2)$$

$$\exp\left\{-j\frac{\omega_c}{c}\,\frac{(x_1-x_2)^2}{(y_1^2+z_2^2)^{\frac{1}{2}}}\right\} \tag{4-17}$$

Because the phase term $\exp\left\{-j\omega_c \frac{2(y_1^2+z_2^2)^{\frac{1}{2}}}{c}\right\}$ is independent of azimuth its effect can be taken out and absorbed in the reflectivity function $\rho(x,y)$. In terms of the system block diagrams, we now have Fig. 4-8 where

$$\begin{aligned} h_t(t;y_1) &= \exp(j\omega_0 t) f_s\left(t-\frac{2(y_1^2+z_2^2)^{\frac{1}{2}}}{c}\right) \\ h_z'(x_1-x_2,y_1) &\triangleq A(x_1-x_2,y_1,z_2) \\ &\qquad \exp\left\{-j\frac{\omega_c}{c}\frac{(x_1-x_2)^2}{(y_1^2+z_2^2)^{\frac{1}{2}}}\right\} \end{aligned} \qquad (4\text{-}18)$$

Eq. (4-18) is the form assumed for most SAR processing. The equation clearly expressed the separability of the PSF in which the range information is provided by the timing of the returns whereby the azimuth information is provided by the phase history induced by the motion x_1-x_2.

All the assumptions required so far can usually be justified in practical SAR systems of stripping mode. We proceed to approximate Eq. (4-18) by a PSF separable in azimuth and range, i.e., such that h_z is independent of y_1 in Eq. (4-18). This will be true if

(A) $A(x_1-x_2,y_1,z_2) = A(x_1-x_2,z_2)$

(B) $\exp\left\{-j\frac{\omega_c}{c}\frac{(x_1-x_2)^2}{(y_1^2+z_2^2)^{\frac{1}{2}}}\right\} \cong \exp\left\{-j\frac{\omega_c}{c}\frac{(x_1-x_2)^2}{(y_1'^2+z_2^2)^{\frac{1}{2}}}\right\}$

where y_1 and y_1' are azimuth coordinates for any two target points under the antenna illumination. (A) can be made

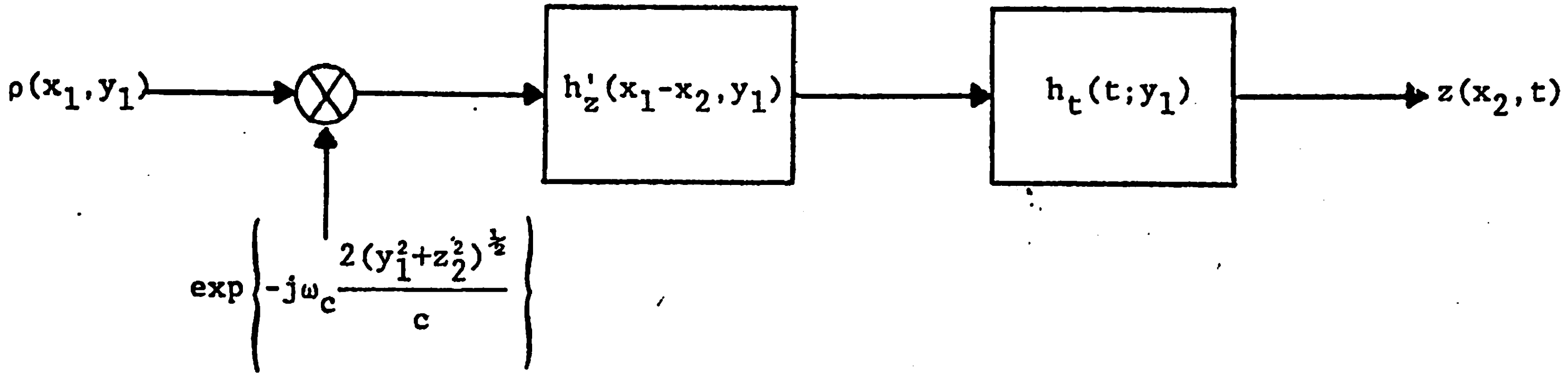

Fig. 4-8. Block diagram of Equation (4-15)

approximately true by an appropriate antenna pattern tailored for the imaging geometry.

(B) will be true if $\frac{y_{1max}^2+z_2^2}{y_{1min}^2+z_2^2} \approx 1$ where y_{1min} and y_{1max} are the y_1 coordinates of the target points at maximum and minimum ranges covered by the antenna beam, respectively. In that case, the azimuth modulation would be same linear FM at all range bins. We shall not elaborate on the exact requirements for the inequality.

It is pointed out that in general (B) cannot hold. However, if it could, then the system of Eq. (4-18) would be separable:

$$h(x_2,t;x_1,y_1) = h_t(t;y_1)h_z(x_2-x_1) \qquad (4\text{-}19)$$

Further theoretical reduction of the PSF is still possible: if we make the offset frequency 0 and assume that $y_1 >> z_2$ for all valid y_1 such that $z(y_1^2+z_2^2)^{\frac{1}{2}}/c$ can be approximated by $\frac{2y_1}{c}$, then by changing variable $t_2 \triangleq \frac{2y_1}{c}$ we will have

$$h_t(t;y_1) = f_s\left(t-\frac{2y_1}{c}\right)$$

or

$$h_t(t;t_2) = f_s(t-t_2)$$

so

$$\begin{aligned} h(x_2,t;x_1,y_1) &= h_1(x_2,t;x_1,t_1) \\ &= h_t(t-t_2)h_z(x_2-x_1) \qquad (4\text{-}20) \end{aligned}$$

EQUATION NUMBER	FORM OF PSF	CASE 1	ASSUMPTIONS²
(4-9) (4-10) (4-11)	$h(x_2-x_1;t,y_1)$	2	1. different pulse return do not overlap 2. aircraft stationary in Δx_2 time
(4-12) (4-14) (4-15)	$h_t(t;y_1)h_z(x_2-x_1\|y_1)$	5	1. $\rho_r > \frac{\beta}{8} L_{eff}$
(4-19)	$h_t(t;y_1)h_z(x_2-x_1)$	8	1. $A(x_1-x_2,y_1,z_2) \approx A(x_1-x_2,z_2)$ 2. $\frac{y_{1max}^2+z_2^2}{y_{1min}^2+z_2^2} \approx 1$
(4-20)	$h_t(t-t_2)h_z(x_2-x_1)$	9	1. range offset frequency $\omega_o=0$ 2. $\frac{(y_1^2+z_2^2)^{\frac{1}{2}}}{y_1} \approx 1$

1. Cases defined in Chapter 2.
2. All assumptions in upper blocks remain ture in lower ones.

Table 4-1. Summary of PSF Simplifications which is a separable space invariant PSF (SSIPSF).

A summary of the properties of the PSF's under various assumptions is listed in Table 4-1.

4.5 Conclusions

This chapter presents the analysis of the stripping mode of the SAR from a PSF point of view. A series of PSF's of the imaging system is derived based on various geometrical and mathematical assumptions. Depending on the degree of precision one pursues the PSF's vary from the most complicated case of a non-separate one-dimensional invariant processing to a separable two-dimensional invariant processing. The requirements for most of the approximations are derived. Many parameters are present in the radar equations which look formidably complicated in some of its most precise forms. By classifying the equations according to the method in Chapter 2, parameters can be clearly separated from the variables associated with the imaging equations and great insight into the image formation methods is readily provided.

The concept of preprocessing is briefly mentioned in this chapter. Details of processing techniques for the reconstruction are not presented until later chapters.

Chapter 5

TURNTABLE RADAR IMAGING

5.1 Introduction

Synthetic aperture radars achieve high azimuth resolution by coherently processing the phase histories of the target points. Based on this principle there are three modes of SAR: the stripping mode, the doppler beam sharpening mode and the spotlight mode. In the previous chapter the stripping mode has been analyzed and many radar parameters introduced. In this chpater we study a radar imaging geometry closely resembling the spotlight mode and in a well controlled environment where the relative motion between the radar and target is a strict circle.

We will show that the underlying radar imaging system is very similar to a computer aided tomographic (CAT) system from the PSF point of view. Unfortunately, physical limitations, e.g. the aspect-angle-dependence of the target reflectivities and the shadowing effect from 3-D obscuration, discourage one from applying a tomography-like reconstruction to the reflected signals. Hence, instead the SAR principles will be applied directly to small angle looks and several looks will then be registered and incoherently summed to give the full reconstruction of the object reflectivity function. A DOF as well as Nyquist rate analysis in the frequency domain will be derived to show the minimum number of data points required for image reconstruction under specified physical constraints and requirements. Basic relations between bandwidth and resolution will also be discussed.

5.2 The RAT SCAT Facility and Data Acquisition

The original design purpose of the RAT SCAT (standing for RAdar Target SCATter Site) facility is to measure radar cross section (RCS) of various targets at different distances, angles, elevations and frequencies [5-1]. In operation, the target (say a model airplane) is placed on a rotator at a distance r_0 from the radar to its rotation center as shown in Fig. 5-1. A reference sphere S is sitting at distances r_1 from the radar R and r_2 from the rotation center C. The angle between line RS and the target line of sight RC is α. Let (ξ,η), (x,y) be two rectangular coordinate systems with origins at C. Let (ξ,η) be fixed on the target and (x,y) on the ground at an angle θ from the former coordinates, as depicted in Fig. 5-2. At discrete angle θ_i the radar radiates continuous waves (CW's) single frequencies f_k for various k. The radar receiver at the reference sphere S takes the signal directly from R to S as a reference and beats it with the signal reflected from the target. The resultant in-phase and quadrature phase

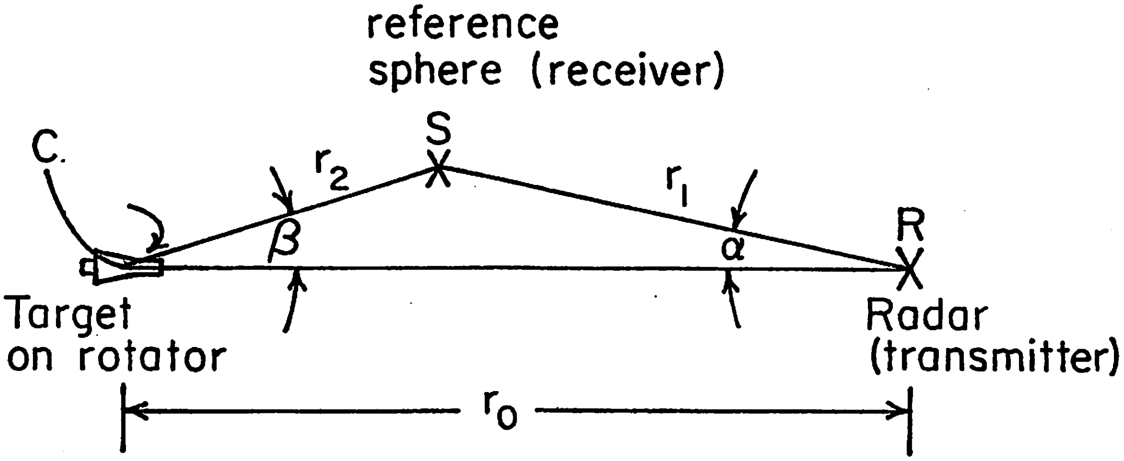

Fig. 5-1. Relation among radar, target and reference sphere

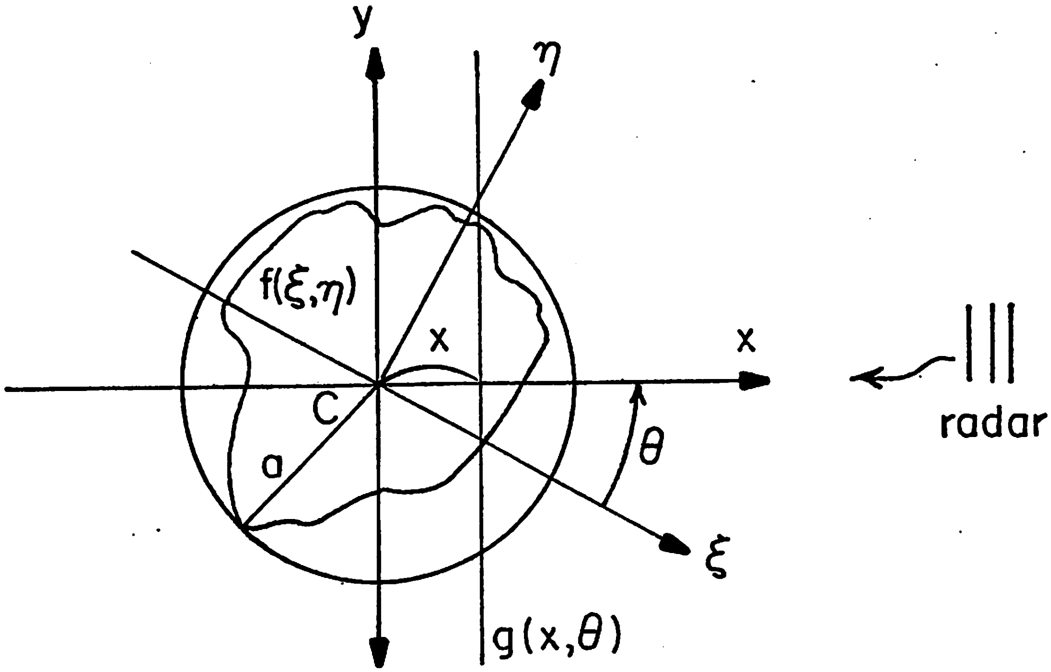

Fig. 5-2. Geometry of coordinate systems (ξ,η): target, (x,y): ground or radar

components become the data. This process continues for different k and i to form a 2-D data array. For simplicity we shall assume that at each aspect angle the radar radiates the same set of M frequency waves at a fixed frequency step Δf. We shall assume that the angle step $\Delta\theta$ is also constant as one advances the aspect orientation.

5.3 Hypothetical Target Reflectivity Function

Referring to Fig. 5-2, let $f(\xi,\eta)$ be the reflectivity function of the target, where by reflectivity function $f(\xi,\eta)$ we mean the ratio of the received signal due to a point target at (ξ,η) with the radiating signal. At wavelengths λ small compared with the curvature of the target body, as used in our experiments, the target looks specular to the radar [5-2] so that only those surfaces at appropriate orientations to the radiation path reflect strong energy back to the radar receiver. In addition, wherever a point (ξ,η) is blocked by some other points or surfaces in the line of sight (LOS) to the radar, shadowing occurs. In other words, the shadowing effect occurs because of the non-convexity of the surface of the target. Thus $f(\xi,\eta)$ is actually a function of aspect angle θ. Nevertheless, for ease of analysis we assume that $f(\xi,\eta)$ is independent of θ and we shall see a close resemblance of this imaging system to that of a tomography. A great deal of insight can be obtained by this theoretical assumption. Even if we release this assumption, as we shall do later, the DOF analysis based on fixed $f(\xi,\eta)$ is still valid in the real situation.

5.4 PSF of the Imaging System

In Fig. 5-1 let's assume that the angles α and β are so small (in our experiments they are $\approx 1^0$) that the signal reflected to S would essentially be the same as if S were in the line RC at the same distance from C. The distance between the object point at (ξ,η) and the radar is a function of r_0, θ, ξ and η.

$$\begin{aligned} r(r_0,\theta,\xi,\eta) &= [(r_0-x)^2+y^2]^{\frac{1}{2}} \\ &\simeq (r_0-x), \end{aligned} \qquad (5\text{-}1)$$

where we have assumed that $r_0-x >> y$ for all target point coordinates (x,y) or (ξ,η) and

$$\begin{aligned} x &= \xi\cos\theta+\eta\sin\theta \\ y &= \eta\cos\theta-\xi\sin\theta \end{aligned} \quad \text{or} \quad \begin{aligned} \xi &= x\cos\theta-y\sin\theta \\ \eta &= y\cos\theta+x\sin\theta \end{aligned} \qquad (5\text{-}2)$$

where θ is the angle from ξ axis (on the target) to the x axis (on the imaging device). Thus

$$\begin{aligned} \frac{\partial r(r_0,\theta,\xi,\eta)}{\partial\theta} &= \frac{\partial[(r_0-\xi\cos\theta-\eta\sin\theta)^2+(\eta\cos\theta-\xi\sin\theta)^2]^{\frac{1}{2}}}{\partial\theta} \\ &= \tfrac{1}{2}\frac{2(r_0-x)(\xi\sin\theta-\eta\cos\theta)+2y(-\eta\sin\theta-\xi\cos\theta)}{r(r_0,\theta,\xi,\eta)} \\ &\cong \xi\sin\theta-\eta\cos\theta = -y \end{aligned} \qquad (5\text{-}3)$$

where we have assumed $r_0 - x \approx r(r_0, \theta, \xi, \eta)$.

Equations (5-1) and (5-3) reveal that the lines of constant range and lines of constant doppler are parallel to the y,x axis, respectively. Lines of constant range can be separated or resolved by range or timing processing while lines of constant dopplers can be separated by azimuth or doppler processing, roughly speaking.

We proceed to find the PSF's of the imaging system.

Let a be the maximal radial extent of the target. Define line projection at angle θ and range x by

$$g(x,\theta) = \int_{-a}^{a} f(\xi,\eta)dy \qquad (5\text{-}4)$$

which is the integration of the reflectivity function $f(\xi,\eta)$ over all target points at distance $r_0 - x$ to the radar when the x axis is at an angle θ from ξ axis. The radar transmits signals of the forms

$$f_k(t) = A\cos(2\pi f_k t + \Phi) \qquad k = 1,2,\ldots,M \qquad (5\text{-}5)$$

at discrete θ_i, $i = 1,2,\ldots,N$, where A is an amplitude factor and Φ a phase term. The signal reflected to the reference sphere from the "line mass" at range $r_0 - x$ is

$$z(x,i,k,t) = Bg(x,\theta_i)\cos\left[2\pi f_k\left(t - \frac{r_0 + r_2 - 2x}{c}\right) + \Phi\right] \qquad (5\text{-}6)$$

where the signal power, propagation decay and reflectivity phase have been absorbed into the complex constant B. The return from the whole object is a summation of the contributions from different ranges:

$$\begin{aligned} z(i,k,t) &= \int_{-a}^{a} z(x,i,k,t)\,dx \\ &= B\int_{-a}^{a} g(x,\theta_i)\cos\left[2\pi f_k\left(t-\frac{r_0+r_2-2x}{c}\right)+\Phi\right]dx \end{aligned} \tag{5-7}$$

which is again a CW.

The signal received by S along path RS assumes the form

$$y(k,t) = C\cos\left[2\pi f_k\left(t-\frac{r_1}{c}\right)+\Phi\right] \tag{5-8}$$

When signals in Eqs. (5-7) and (5-8) are mixed or multiplied at S, they become

$$\begin{aligned} z(i,k,t)y(k,t) &= BC\int_{-a}^{a} g(x,\theta_i)\cos\left[2\pi f_k\left(t-\frac{r_0+r_2-2x}{c}\right)+\Phi\right]\cdot \\ &\qquad \cos\left[2\pi f_k\left(t-\frac{r_1}{c}\right)+\Phi\right]dx \\ &= \frac{BC}{2}\int_{-a}^{a} g(x,\theta_i)\cos\left[2\pi\left(2f_k t-\frac{r_0+r_1+r_2-2x}{c}\right)+2\Phi\right]dx+ \\ &\quad \frac{BC}{2}\int_{-a}^{a} g(x,\theta_i)\cos\left[2\pi f_k\left(\frac{r_1-r_0-r_2}{c}+\frac{2x}{c}\right)\right]dx \end{aligned} \tag{5-9}$$

The first term in Eq. (5-9) is a high temporal frequency term which can be filtered out to leave only

$$I(i,k) = D\int_{-a}^{a} g(x,\theta_i)\cos\left(2\pi f_k\frac{2x}{c}+2\pi f_k\frac{r_1-r_0-r_2}{c}\right)dx \tag{5-10}$$

Similarly by beating z(i,k,t) in Eq. (5-7) with 90^0 shifted version of y(k,t), one obtains

$$Q(i,k) = -D\int_{-a}^{a} g(x,\theta_i)\sin\left(2\pi f_k\frac{2x}{c}+2\pi f_k\frac{r_1-r_0-r_2}{c}\right)dx \tag{5-11}$$

Define

$$\mathscr{F}_k\{g(x,\theta_i)\} = \int_{-a}^{a} g(x,\theta_i)\exp\left(-j\frac{2\pi f_k x}{c}\right)dx \qquad (5\text{-}12)$$

and compare Eqs. (5-10) and (5-11) with (5-12). $2\pi f_k \frac{r_1-r_0-r_2}{c}$ in (5-10) and (5-11) is a linear phase term with respect to f which if compensated for would make I(i,k) and Q(i,k) the Fourier component of the shadow gram $g(x,\theta_i)$ at angle θ_i and frequency $\frac{2f_k}{c}$. According to the circular projection theorem [5-5], the data [I(i,k),Q(i,k)] takes on the value in the ring in Fourier frequency domain as shown in Fig. 5-3 with the extra linear phases mentioned.

Mathematically the structure of the data obtained has a considerable similarity to that of the Fourier transformed data of an infinitely narrow parallel-beam tomographic imaging system [5-4,5]:

In the computer aided tomographic system, let $p(\gamma,\theta)$ denote the integral of the object transmission (in the radar system it would be the reflectivity) function $f(\xi,\eta)$ or $f(x,y)$ along the line $L(r,\theta)$, as shown in Fig. 5-4. As before, coordinates (ξ,η) are assumed fixed on the object or target and (x,y) fixed on the data gathering device (in the radar system it would be the transmitter and receiver). The two coordinate systems are related by

$$\begin{aligned} x &= \xi\cos\theta+\eta\sin\theta \\ y &= \eta\cos\theta-\xi\sin\theta \end{aligned} \quad \text{or} \quad \begin{aligned} \xi &= x\cos\theta-y\sin\theta \\ \eta &= y\cos\theta+x\sin\theta \end{aligned} \qquad (5\text{-}13)$$

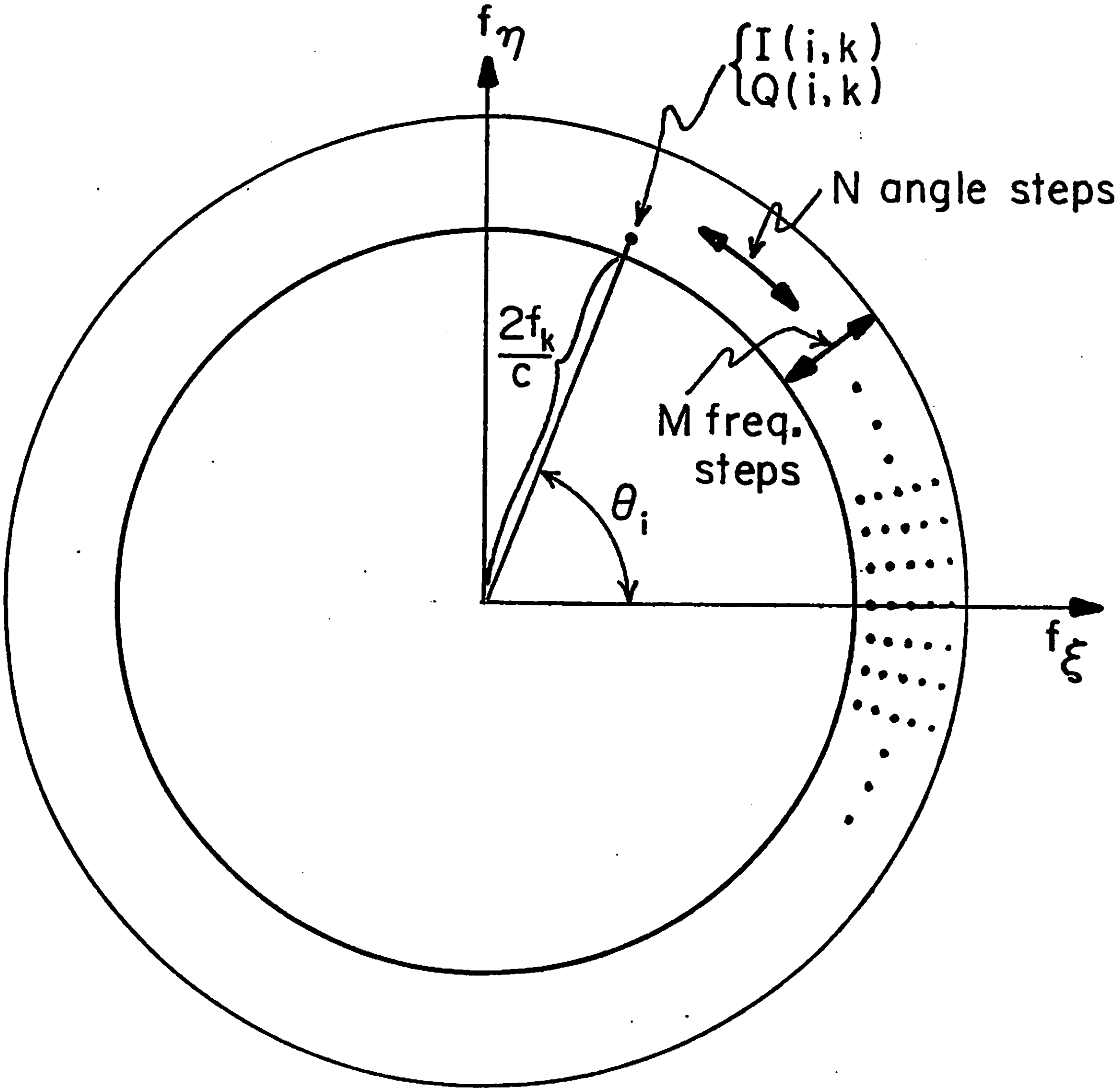

Fig. 5-3. Raw data in frequency domain

as in Eq. (5-2). The equation for the line $L(r,\theta)$ is $x-r=0$ or $\xi\cos\theta+\eta\sin\theta-r=0$. Thus

$$p(r,\theta) = \int_{L(r,\theta)} f(\xi,\eta)ds \qquad (5\text{-}14)$$

where s is along line $L(r,\theta)$

The set $S=\{p(r,\theta)\,|\,-\infty<r<\infty,\ 0<\theta\leq\pi\}$ is called the shadowgram which is a transformation of the object function $f(\xi,\eta)$ or $f(x,y)$, and is the data one obtains from a parallel beam tomographic system. A famous way to reconstruct $f(\xi,\eta)$ from $p(r,\theta)$ is to use the back projection convolutional method [5-6]. Other reconstruction algorithms can be found in [5-7]. However, if we take the Fourier transform of $p(r,\theta)$ with respect to r,

$$P(\omega,\theta) = \int_{-\infty}^{\infty} p(r,\theta)\exp(-j\omega r)dr = \int_{-\infty}^{\infty}\int_{L(r,\theta)} f(\xi,\eta)\exp(-j\omega r)dsdr,$$

and compare with

$$F(\omega,\theta) = \int\int_{-\infty}^{\infty} f(\xi,\eta)\exp[-j\omega(\xi\cos\theta+\eta\sin\theta)]d\xi d\eta \qquad (5\text{-}15)$$

where $F(\omega,\theta)$ is the two-dimensional Fourier transform of f in polar coordinates, it is obvious that

$$P(\omega,\theta) = F(\omega,\theta)$$

Hence $f(\xi,\eta)$ can be reconstructed by taking a 2-D inverse FFT upon $F(\omega,\theta)$ or $P(\omega,\theta)$:

$$f(\xi,\eta) = \frac{1}{4\pi^2}\int_0^{\pi}d\theta\int_{-\infty}^{\infty} P(\omega,\theta)\exp[j\omega(\xi\cos\theta+\eta\sin\theta)\omega d\omega] \qquad (5\text{-}16)$$

Thus it seems the RAT-SCAT image could be obtained by a 2-dimensional inverse Fourier transformation upon the data, just as in the transformed tomographic system. There are, however, several differences which should not be overlooked:

(1) The validity of the hypotheses made in Section 5.3.

(2) A linear phase factor (if not compensated for) in RAT SCAT as in Eq. (5-11).

(3) Bandpass (instead of low pass) property of data gathering ability of RAT SCAT as in Fig. 5-2.

Because of (1) and (2) one has to seek algorithms other than those from tomography to reconstruct our RAT SCAT images. Becuase of (3) the radar images have no "DC" term and magnitudes or intensity of complex reflectivities have to be taken in order to display the final stages. We'll next derive the minimal number of data required to reconstruct a target of given size and required resolution, show the relation between resolution and bandwidth and then propose a reconstruction algorithm which turns out basic to all modes of SAR's.

5.5 DOF of the Data

The DOF problem of an imaging system arises because the data available for image reconstruction are not independent. In other words, there are overlappings among different PSF's of the data acquisition system. A common method to tackle the DOF problem is to form the correlation matrix [Γ] of the imaging system and try to diagonalize it. The eigenvalue spectrum and the rank of [Γ] give a quantitative measure of the DOF.

The degrees of freedom problem of a tomographic projection system has been analyzed in detail by McCaughey and Andrews [5-5]. Because of its mathematical similarity, we will apply some of their results to the RAT SCAT data.

First, for the purpose of clearity and convenience, let's normalize the spatial extent of the target as in [5-5]. We assume that the object has a maximal radial extent of a meters and that the minimal and maximum radar frequencies applied at each aspect angle are f_{min} and f_{max}, respectively, which give respective 2 way wavelengths

$$\begin{aligned} \lambda_{max} &= \frac{1}{f_{min}} \times \frac{c}{2} \\ \lambda_{min} &= \frac{1}{f_{max}} \times \frac{c}{2} \end{aligned} \qquad (5\text{-}17)$$

where c is the speed of EM waves. The normalized frequencies have a spectrum from

$$f_1 = \frac{a}{\lambda_{max}} \qquad \text{to} \qquad f_2 = \frac{a}{\lambda_{min}} \qquad (5\text{-}18)$$

Refer to Fig. 5-5.

For the circular imaging system on the unit-radius object it has been shown in [5-5] that the (i,m,k,l)th

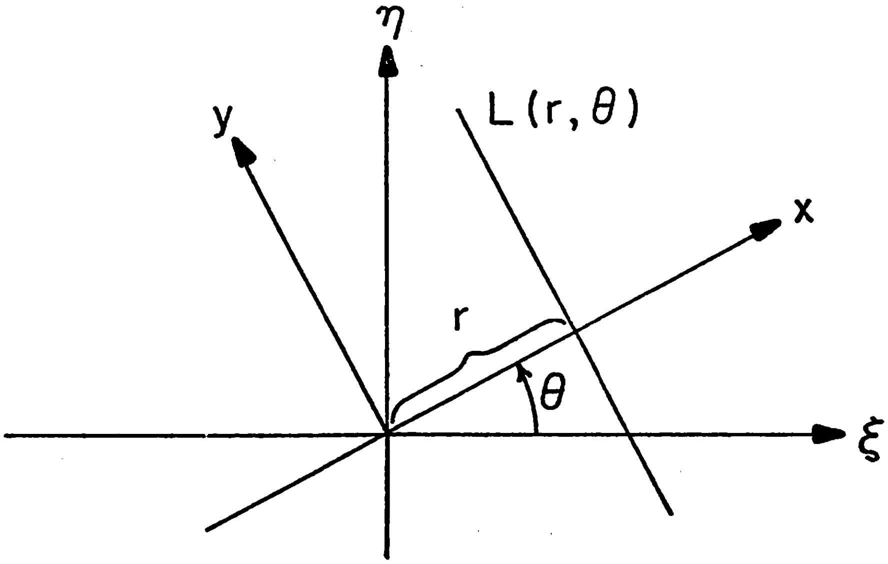

Fig. 5-4. Projection imaging geometry

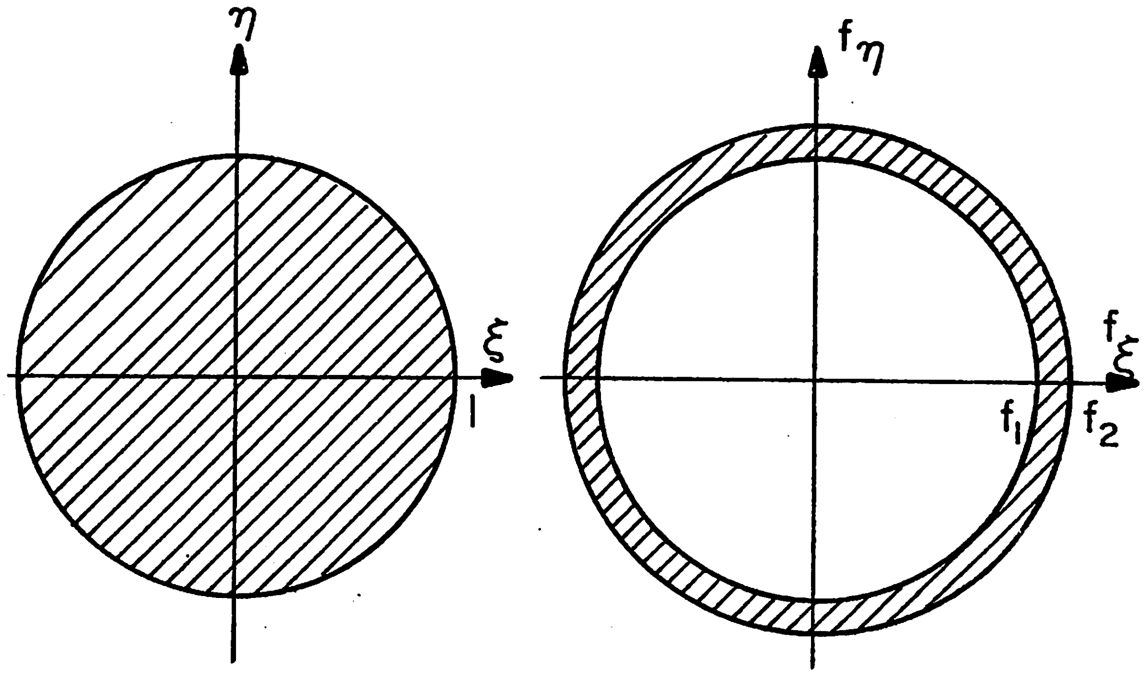

(a) spatial domain (b) frequency domain

Fig. 5-5. Spatial and frequency domains of a spatially normalized target entry $r_{k,l}^{i,m}$ of $[\Gamma]$ is

$$r_{k,l}^{i,m} = \iint_R \exp[-j2\pi u_k(\xi\cos\theta_i+\eta\sin\theta_i)]\exp[+j2\pi u_l(\xi\cos\theta_m+\eta\sin\theta_m)]d\xi d\eta$$

$$= \frac{J_1[2\pi(u_k^2-2u_k u_l\cos(\theta_i-\theta_m)+u_l^2)]^{\frac{1}{2}}}{[u_k^2-2u_k u_l\cos(\theta_i-\theta_m)+u_l^2]^{\frac{1}{2}}} \qquad (5\text{-}19)$$

where (i,k) and (m,l) are indexes of any two, possibly same, data points; i and m are azimuth angle indices and k and l are frequency indices along radial direction. $J_1(\cdot)$ is the first order Bessel function of the first kind, R is the unit circle and $0 \leq \theta_i,\ \theta_m < 2\pi$, $f_1 \leq u_k, u_l \leq f_2$. Eq. (5-19) can be rewritten as

$$r_{k,l}^{i,m} = \frac{J_1[2\pi\rho(k,l,i,m)]}{\rho(k,l,i,m)} \qquad (5\text{-}20)$$

where $\rho(k,l,i,m) = [u_k^2-2u_k u_l\cos(\theta_i-\theta_m)+u_l^2]^{\frac{1}{2}}$, which is nothing but the distance between two points (i,k) and (m,l) in the frequency plane. In other words, $r_{k,l}^{i,m}$ is only a function of the distance between the two data points. Therefore, one can think of the data as samples of a two-dimensional stationary process with correlation function $\frac{J_1(2\pi\rho)}{\rho}$ which is the Fourier transform of the unit circle which defines the object spatial extent. The correlation pattern is the same no matter where the points are considered and manipulation methods of stationary processes such as the Nyquist sampling theorem can be applied to easily solve the DOF problem.

A stationary process with correlation function $\frac{J_1(2\pi\rho)}{\rho}$ has a power spectrum (Fourier transform of the correlation function) circ(r) and is bandlimited with radial cutoff frequency 1, as shown in Fig. 5-6. According to the Nyquist sampling theorem, the sampling interval in the frequency domain must be $\leq 1/2$ in order to avoid any aliasing in the spatial domain. This coincides with the more intuitive fact that to adequately represent an object of maximum spatial extent S, the sampling interval in its frequency domain should not be larger than 1/S (note that S=2 in our case of a normalized target). This information can be used to determine the maximum allowable frequency step in the radial direction and maximum angle step in azimuth without ambiguities. As an alternative way of analysis the "effective correlation region" in the data domain can be determined from Eq. (5-20) and approximate DOF of the data band in Fig. 5-5b can be determined by dividing the ring area by the effective correlation region.

Because of the stationarity of the random process in the data space, an interesting phenomenon results when one, say, doubles the initial frequency in Fig. 5-5b while keeping other parameters unchanged. The area in the ring will be approximately doubled and thus the same to the DOF. Although the range (along the radial direction) resolution doesn't change by such a new arrangement, the azimuth or along angle direction does double its DOF by the doubling

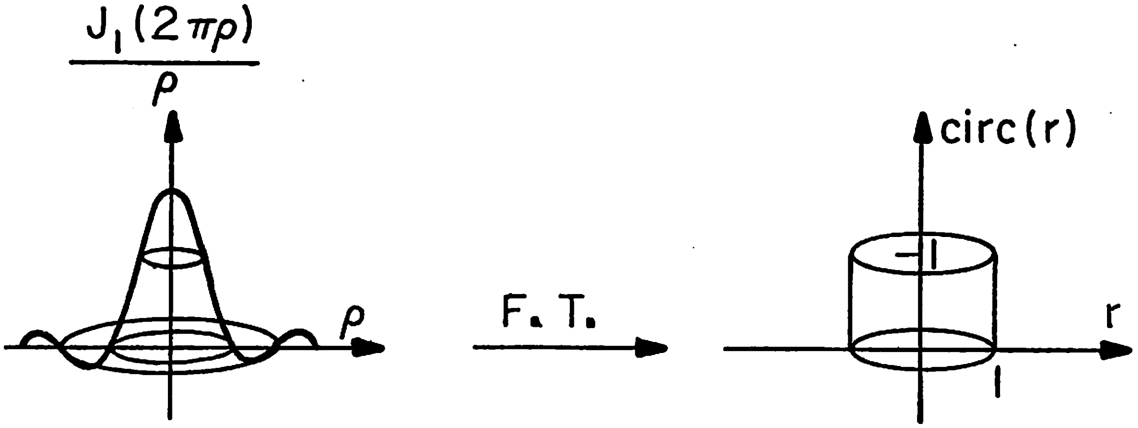

Fig. 5-6. Correlation of the data and its Fourier transform

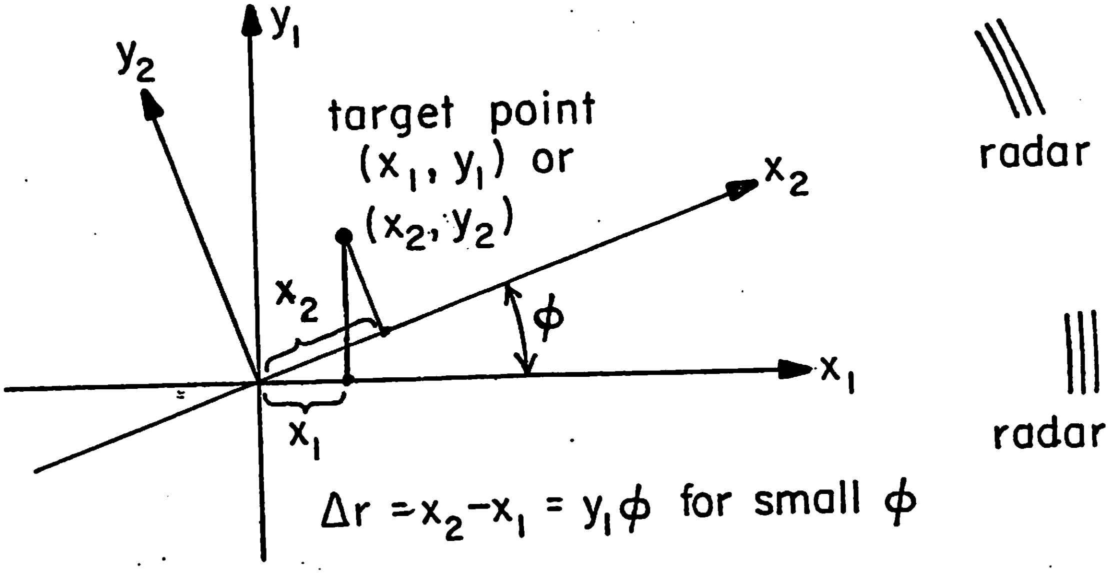

Fig. 5-7. Separability of azimuthal and range processing at small angle variation Φ. (Target coordinates fixed on paper)

of its circumference and hence number of independent samplings. This means twice (better) the azimuth resolution although the radial resolution remains the same. This phenomena does not exist in one-dimensional radar pulsing where the range data is the only information sought. In that case the only purpose of the carrier frequency is to carry a signal of certain bandwidth and it is the bandwidth and not the carrier frequency which determines the range resolution. However, in our 2-D radar system the carrier frequency comes into the radar imaging equation directly and manifests itself as a major azimuthal parameter. In terms of radar terminology, a raise in carrier frequency increases the doppler rate and thus will widen the potential azimuth bandwidth of the frequency spectrum generated by a single target point. However in some situations, e.g. the stripping mode of SAR in which the antenna pattern width is inversely proportional to the wavelength the two factors cancel, leaving the doppler spectral width, and hence the system performance independent of the carrier frequency. [5-2]

5.6 Actual Reconstruction Method

Physically the radar imaging system has lots of differences from the tomography projection system because of the many widely different imaging characteristics. Some of the differences have been described in the end of Section 5.4.

In the radar imaging system range resolution is obtained by the "timing" of the signal return from the target point. In RAT SCAT multiple frequency signature (MFS) is used and the timing information is resolved by taking Fourier transformation along the stepped frequencies. Ideally, the relative motion between the target points and the radar should be zero to obtain range resolution with any high degree of precision desired. On the other hand, the azimuthal resolution is introduced by the created different doppler histories at different azimuthal points by way of a relative motion between the target points and the radar. The seemingly conflicting requirements are resolved in the RAT SCAT system in which different frequency components at an aspect angle θ are obtained during which there is no relative target motion. Azimuthal information is then provided by the phase differences of the same frequency components at different θ's due to the range change of target points induced by the target rotation.

In Fig. 5-7 let (x_1,y_1) and (x_2,y_2) be the coordinates of the same point with the aspect angle difference being Φ. Similar to Eq. (5-13) we have

$$\begin{aligned} x_2 &= x_1\cos\Phi+y_1\sin\Phi & \qquad x_1 &= x_2\cos\Phi-y_2\sin\Phi \\ & & \text{or} & & \qquad (5\text{-}21) \\ y_2 &= y_1\cos\Phi-x_1\sin\Phi & \qquad y_1 &= y_2\cos\Phi+x_2\sin\Phi \end{aligned}$$

Thus the range of the point undergoes a change of

$$\begin{aligned}\Delta r(x_1,y_1x_2,y_2) &= x_2-x_1\\ &= x_1\cos\phi+y_1\sin\phi-x_1\\ &= x_1(\cos\phi-1)+y_1\sin\phi \qquad (5\text{-}22)\end{aligned}$$

which creates different phse histories to each target point in going from one radar coordinate (x_1,y_1) to the other (x_2,y_2). In Eq. (5-22) if Φ is small enough, then

$$\cos\Phi \approx 1 \quad \text{and} \quad \Delta r(x_1,y_1,x_2,y_2) \approx y_1\sin\Phi \approx y_1\Phi \qquad (5\text{-}23)$$

which is independent of x_1 or the range. The phase variation as a function of Φ induced by $r(\Phi)$ creates a doppler frequency $\frac{dr}{d\Phi} = y$. Because different y are associated with different doppler shifts, the azimuth targets can be resolved by taking Fourier transforms on the data along small azimuthal angles, as long as the data are taken from appropriate range bins. Usually separability of azimuthal and range processings are desired because of its high efficiency in computation [5-13], in which the two processings can even be interchanged if so desired. To insure the separability range curvature* has to be avoided by limiting Δr in [5-22] to be less than one range bin width or max $\Delta r<1$ range bin width. This amount to a coherence aspect angle $\Phi<$one range bin width in the target with normalized size. Since both the range and azimuth require

---

*The term "range curvature" in the subsequent chapters bears the same meaning as "motion through resolution cells" in [4-13].

Fourier transformation as explained, separability implies using 2-D Fast Fourier Transformations (FFTs') which transforms the data in frequency domain to the reflectivity function in spatial domain.

Fig. 5-8 shows a section of data for such a small fan angle Φ. B_r is the range bandwidth with range frequency step Δf_r and B_{z_1} and B_{z_2} are the minimum and maximum azimuth bandwidths at f_1 and f_1 respectively, with azimuth frequencies step Δf_{z_1} and Δf_{z_2}. Note that

$$B_r = M \times \Delta f_r = f_2 - f_1$$

$$B_{z_1} = N_a \times \Delta f_{z_1} = N_a \times f_1 \Delta\theta \qquad (5\text{-}24)$$

$$B_{z_2} = N_a \times \Delta f_{z_2} = N_a \times f_2 \Delta\theta$$

where $\Delta\theta$ is the azimuth step angle in radian and N_a is the number of azimuth points coherently processed.

Discrete Fourier transforms on M number of data along range frequency with frequency step Δf_r and bandwidth B_r give the range profile with unambiguous spatial dimension R and range bin width Δr where

$$R = \frac{1}{\Delta f_r} \qquad (5\text{-}25)$$

and

$$\Delta_r = \frac{1}{B_r} \qquad (5\text{-}26)$$

Eqs. (5-24) and (5-25) are dual relations of sampling theorem. Similarly in the azimuth direction

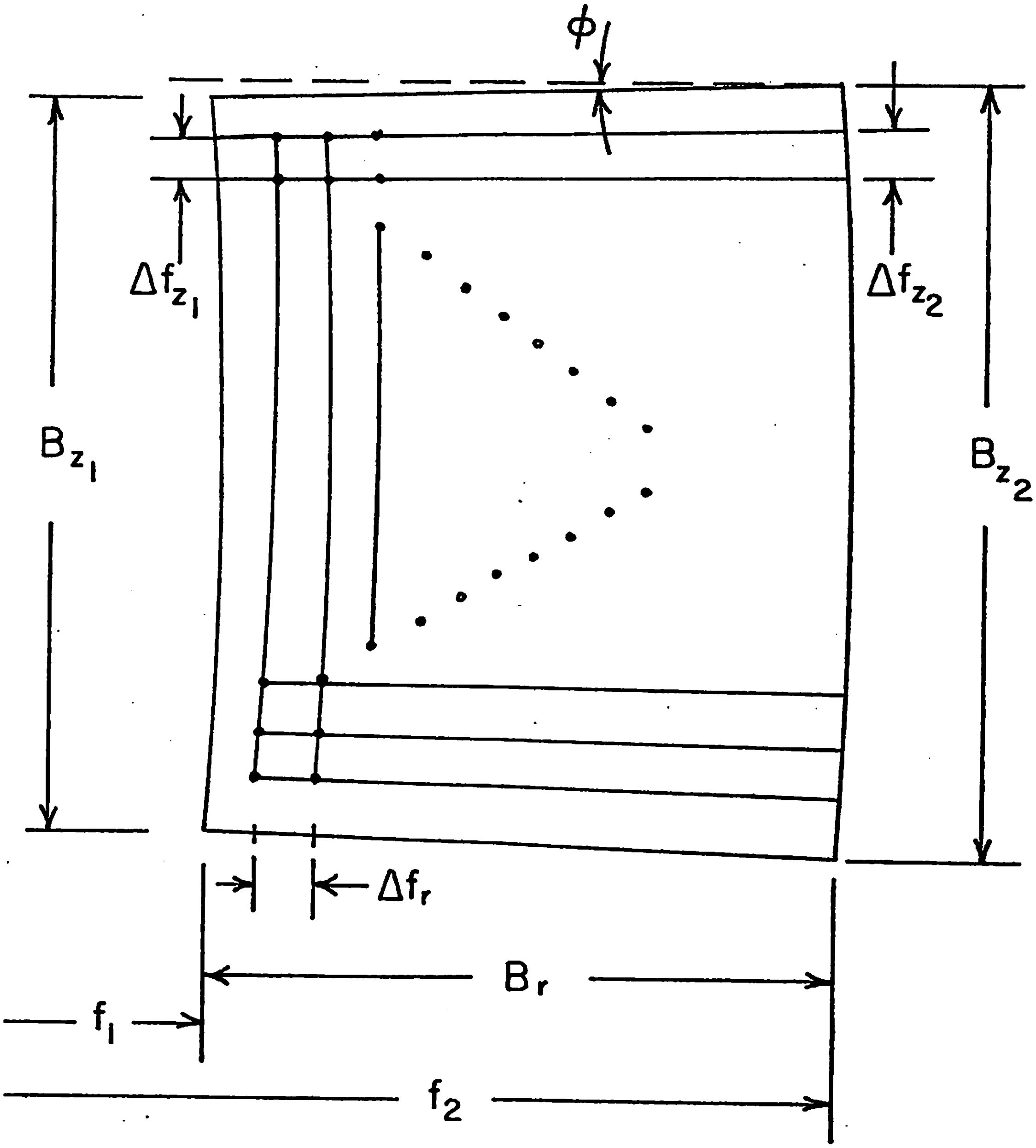

Fig. 5-8. Separable processing of range and azimuth, small fan angle Φ

$$Z_1 = \frac{1}{\Delta f_{z_1}} \quad , \quad Z_2 = \frac{1}{\Delta f_{z_2}}$$

and

$$\Delta z_1 = \frac{1}{B_{z_1}} \quad , \quad \Delta z_2 = \frac{1}{B_{z_2}}$$

where Z_1, Z_2 are the unambiguous spatial dimensions of the Fourier transformed data along azimuth direction at the lowest and highest range frequency (i,e., f_1 and f_2), respectively and Δz_1 and Δz_2 are the azimuth bin widths at frequencies f_1, f_2 respectively. Note that $\Delta z_1 \approx \Delta z_2$ or $Z_1 \approx Z_2$, if the 2-D FFT which is separable is valid and creates little image distortion.

In summary, the reasons for taking the 2-D FFT on small angle data are:

1. The reflectivity function is a function of aspect angle.

2. Satisfactory phase compensation for the propagation between the radar and the target center is extremely difficult, if not impossible.

3. However, the reflectivity function can be assumed constant over small aspect angle Φ during which the azimuth and range processing can be separated and FFT techniques can be employed.

4. The shadowing effect can be reduced to a minimum by adopting the technique of coherent processing over small angles and then incoherent summing over large angles, as

described in the next section.

5.7 Incoherent Summation of Different Looks

Coherent processing should be applied to only those radar returns from target points of fixed reflectivity during the imaging. As the azimuth aspect changes by more than a certain amount, speckle and blocking effect change the target reflectivity by so much that the data can no longer be deemed as coherent. Coherent processing on the data of a small aspect angle span gives the "look" of the target from that particular angle and shows only those target surfaces approximately normal to that particular LOS. Those looks could be integrated incoherently to enhance the final target image. The procedure will be further explained in the following chapter.

5.8 Conclusions

This chapter presents the theory of a high resolution radar imaging from both a radar systems viewpoint and a degrees of freedom or numerical analysis viewpoint. Similarity with the computer aided tomographic scanner imaging technology is pointed out. However the differences between the two systems are emphasized and a radar unique reconstruction algorithm is developed for combined coherent and noncoherent imaging. The actual reconstruction method is presented which will be used in Chapter 6 on the data obtained from the RAT-SCAT facility. The pictorial images resulting from the computational procedures as shown in Chapter 6 are surprisingly recognizable and suggest that these techniques may have some practical application in the future.

Chapter 6

EXPERIMENTAL RESULTS OF RADAR TURNTABLE IMAGING

6.1 Introduction

This chapter presents the experimental results of the radar turntable imaging in Chapter 5. A complete sequence of processing techniques is introduced starting with the photographic presentation of the raw data. Explanations as well as conjectures of the intermediate results are given along the way towards the final images. Many processing parameters are tested against the qualities of images resulted.

Three aircraft targets are individually imaged using actual data which are the complex returns (in-phases and quadrature-phases) of the radar signals from the targets. Two of them are model airplanes (F-102, F-5E) of reduced sizes and the other is a full-sized real F-102 plane. Experiments are done for two setups of the targets, i.e., horizontal and vertical positions, resulting in azimuth and vertical images, respectively. All notations bear the same meanings as in Chapter 5.

6.2 Imaging a Model F-102 Airplane

6.2.1. Physical properties of the imaging geometry

A real F-102 has an overall length and a wing-to-wing width approximately 68 ft. and 38 ft. respectively. The model F-102 is 0.29 times the real size. Other numerical values used in the experiments are listed in Table 6-1. The imaging geometry is depicted in Fig. 5-1. The bandwidth in the range direction is approximately 870 MHz which has an ideal range resolution ρ_r

$$\rho_r = \frac{c}{2\times B_r} \cong \frac{9.84\times10^8\text{ft/sec}}{2\times870\times10^6/\text{sec}} \cong 0.57 \text{ ft.} \qquad (6\text{-}1)$$

The frequency step $\Delta f_r = 3.4$ MHz corresponds to an unambiguous range interval I_r

$$I_r = \frac{c}{2\times\Delta f_r} \cong 132 \text{ ft.} \qquad (6\text{-}2)$$

which is approximately 6.7 times the largest dimension of the target. This means that the data has been oversampled by a factor of 6.7 in the MFS frequency domain. The same conclusion could also be reached from the DOF analysis in the previous chapter by applying Eq. (5-12). The step frequencies in the azimuth direction are between

$$\Delta f_{z_1} \approx f_{min}\times\Delta\theta = 31.87 \text{ MHz} \qquad (6\text{-}3)$$

to

$$\Delta f_{z_2} \approx f_{max}\times\Delta\theta = 36.91 \text{ MHz} \qquad (6\text{-}4)$$

with corresponding unambiguous intervals 12.9 ft. and 14.1 ft. Refer to Fig. 5-8. The unambiguous azimuth intervals are longer than the target dimension, which means that $\Delta\theta = 0.2^o$ is adequate to sample the data in the azimuth

γ_0 : 1652 ft.

γ_1 : 1112 ft.

γ_2 : 540 ft.

f_{min} : 9.13 GHz

f_{max} : 10 GHz

Δf_r : 3.4 MHz

M : 256

$\Delta\theta$: $0.2^{\circ} \approx 0.0035$ rad.

Table 6-1. Model F-102 imaging parameters direction. However, the sampling is barely dense enough because the unambiguous interval is only slightly larger than the target size.

6.2.2 Source data from model F-102 airplane

The source data, which are the returns of each single frequency waveform at each particular azimuth angle of the target, are complex numbers consisting of both the in-phase and quadrature-phase components, which can be transformed into polar coordinates to become the magnitude and phase components. Fig. 6-1 shows the phase and square root of the magnitude of the source data from a horizontally mounted model F-102 target. They are 256 data points along lines of constant azimuth angle and approximately 900 points along the azimuth direction from 0° to 180° of the target orientation. Note that only 180° of data is sufficient for the whole target reconstruction since the target was presumed symmetric horizontally. The square rooting is necessary to reduce the gigantic dynamic range of the radar cross section (RCS) of an airplane as a function of the aspect angle or radar frequency [6-1], at wavelengths (≈ 1.5 cm in our case) much smaller than the average curvature of the airplane. Note that at approximately 60° of the data there were strong returns probably due to the strong reflectivities of the delta wing structure. Similar phenomenon happened close to 90° or broadside position where the fuselage served as

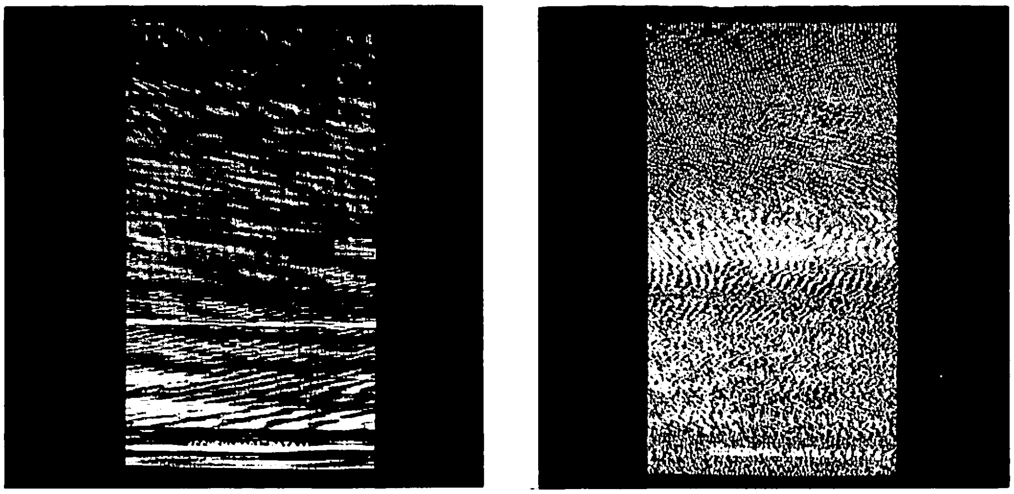

a) Square root of magnitude (0°-90°)

b) Phase (0°-90°)

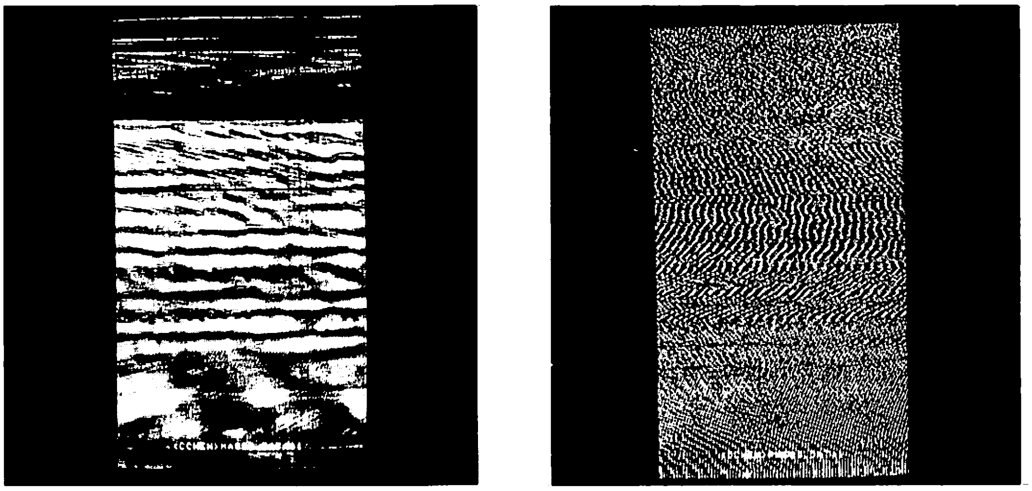

c) Square root of magnitude (90°-180°)

d) Phase (90°-180°)

Fig. 6-1. Source data of the horizontal model F-102;
horizontal direction: range step frequency
vertical direction: azimuth angle
200 x 469 points each image

strong reflectors. Starting from approximately 120° the gain of the radar system seemed raised resulting in higher brightness of the magnitude part of the photographs. The phase part of the source data are linearly coded from $-\pi$ to π for the photograph. The data is in the frequency domain in both the range and the azimuth dimensions. Because of the linear phase due to $\gamma_1 - \gamma_0 - \gamma_2$ as explained in Chapter 5 the oversampling phenomenon along the range is not very obvious. It turns out, as shown in Fig. 6-2, that this linear phase contributes a fixed amount of shift in the spatial domain. The highly structured phases are probably a result of a large signal noise ratio of the radar system.

6.2.3 Fourier transforming in the range direction

Because the source data was in two-dimensional frequency domain, some form of two-dimensional transformation was necessary to bring the data into the spatial domain. As explained in Chapter 5, we segment the data according to their azimuth angle into sectors and then apply 2-D Fourier transformations on each sector which is approximately rectangular or separable. Fourier transforming the data along a fixed aspect angle gives the "projections" of the target onto that line of sight (LOS) at that angle. If the processing is assumed separable between the range and the azimuth then the magnitude parts of the projections provide the range information (range profiles) while the phase

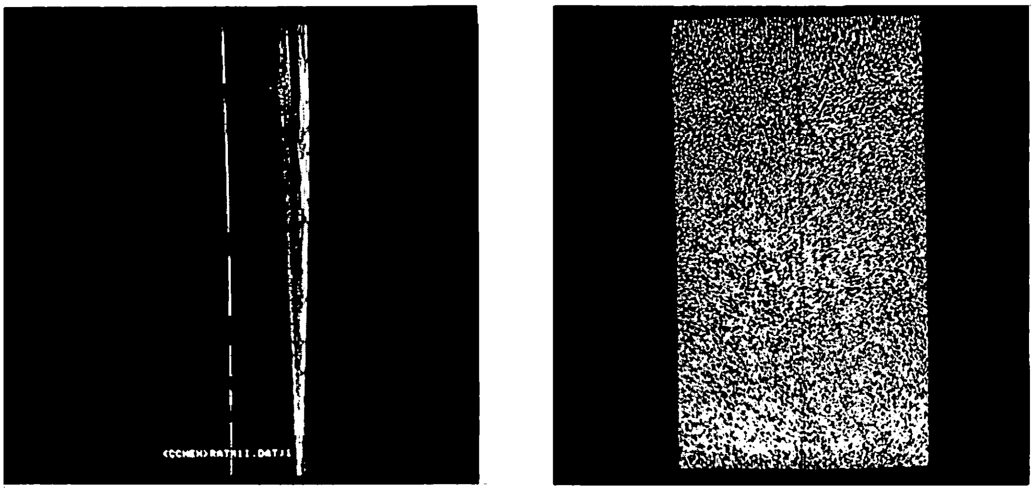

a) Square root of magnitude (0°-90°)

b) Phase (0°-90°)

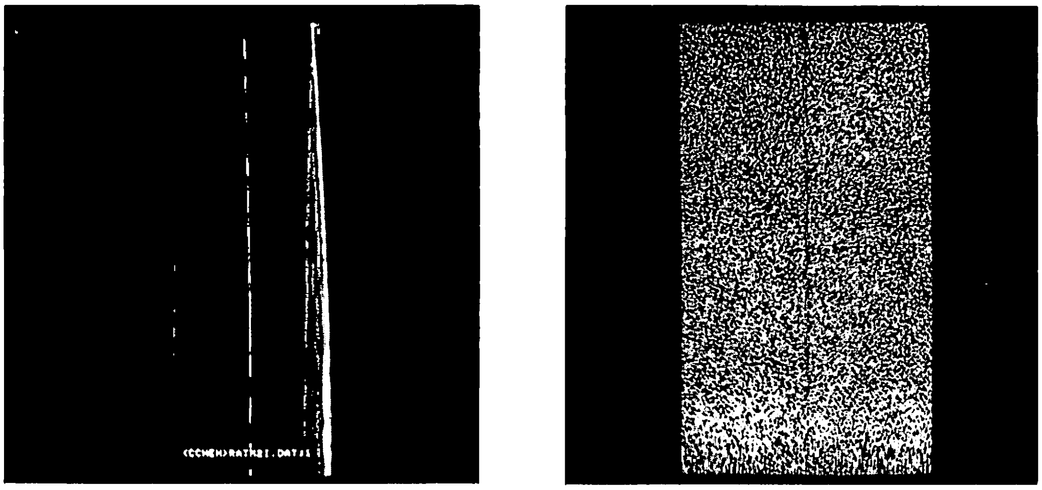

c) Square root of magnitude (90°-180°)

d) Phase (90°-180°)

Fig. 6-2. Fourier transformation along range; radar: to the right parts, when processed with the phases at neighboring aspect angles, will resolve the azimuth information. Toward this assumption our source data was Fourier transformed along the range direction for each azimuth angle and the phase and the magnitude parts of the resultant data are then shown in Fig. 6-2. Note that now the data is in spatial domain along the range and still in frequency domain along the azimuth. Again for a better presentation square rooting is applied to the magnitude parts, which assume a dynamic range of more than 30 dB. The magnitude parts clearly show the location of the target which is off the center of the picture because of the linear phase and the target occupies $\frac{1}{6.7}$ of the whole range dimension as a result of the oversampling in the range frequency domain of the source data. Note the strong returns curving in and out in the figure along the azimuth angle. The bright lines in the center of the magnitude pictures account for the DC bias of the radar receiver and processing unit. The faint mirror images of the target with respect to the central DC line are due to the imbalance of the in-phase and quadratic-phase circuitry of the radar system. To show this, let D_i and D_q be the gains of in-phase and quadrature phase circuitries of the mixer of the radar receiver. From Eq. (5-10), the actual complex data becomes

$$
\begin{aligned}
&I(i,k)+j\theta(i,k)\\
&= D_i \int_{-a}^{a} g(x,\theta_i)\cdot\left[\cos\left(2\pi f_k \frac{2x}{c}+2\pi f_k \frac{\gamma_1-\gamma_0-\gamma_2}{c}\right)\right]dx\\
&\quad + D_q \times j\int_{-a}^{a} g(x,\theta_i)\cdot\left[\sin\left(2\pi f_k \frac{2x}{c}+2\pi f_k \frac{\gamma_1-\gamma_0-\gamma_2}{c}\right)\right]dx\\
&= D_i\cdot G\left(\frac{2f_k}{c},\theta_i\right)\exp\left(j2\pi f_k \frac{\gamma_1-\gamma_0-\gamma_2}{c}\right)\\
&\quad + \frac{(D_g-D_i)}{2j}\left[G\left(\frac{2f_k}{c},\theta_i\right)\exp\left(j2\pi f_k \frac{\gamma_1-\gamma_0-\gamma_2}{c}\right)-G^*\left(\frac{2f_k}{c},\theta_i\right)\cdot\right.\\
&\qquad\qquad\qquad\left.\exp\left(-j2\pi f_k \frac{\gamma_1-\gamma_0-\gamma_2}{c}\right)\right] \qquad (6\text{-}5)
\end{aligned}
$$

where

$$
G(k,i) \triangleq \int_{-a}^{a} g(x,i)\exp(j2\pi kx)dx \qquad (6\text{-}6)
$$

The imbalance of the second term in Eq. (6-5) causes the mirror images in Fig. 6-2. It is reasoned that in Fig. 6-2(a) the strong returns closest to the radar (which is to the right of the photographs) are due to the nose and those in Fig. 6-2(c) are due to the tail of the target. In Fig. 6-2(a) observe a bright tiny spot very close to the nose line at approximately 60° azimuth. Again, it is due to the returns from the delta wing.

The phase figures 6-2(b) and (d) are correlated with their counterparts (a) and (c) in that prominant structures exist only in those regions where there are strong magnitudes due to target points of high reflectivity. In other regions the phases look random and noise like.

There are two ways to remove the redundancy of the data in the range dimension. One is to choose a larger frequency step Δf from the DOF analysis in Chapter 5 to keep only minimum frequency components required in the source data. The other is to retain in the spatial domain the portion containing the target. The latter option has the advantage of offering a higher S/N in the reduced data. In our experiments we always keep 64 range bins in the spatial domain which gives a data reduction of 4:1. The windowing of the data is visually determined from Fig. 6-2(a) and (c). Fine tuning of the target center is necessary because of the unavailability or uncertainty of γ_0, γ_1 and γ_2. This will be discussed in subsection 6.2.5.

6.2.4 Azimuth processing

If the reconstruction, which is basically a two-dimensional transformation as explained before, can be assumed separable, then since the range transformation has been accomplished in the previous subsection, only azimuth transformation remains to be done. In our case of RAT SCAT imaging, separability means no range curvature or range bin moving problems induced by the rotation of the target necessary for azimuth resolution. Since the maximal radial extent of the target is assumed to be no more than 10 feet, the range change will be less than $10 \cdot \phi$ feet for all the target points when the target undergoes a rotation of

ϕ radians assumed so small that $\tan\phi \approx \phi$. If the range walking is to be prohibited at all, then

$$10\times\phi \leq \rho_r = 0.52 \text{ ft.} \qquad (6\text{-}7)$$

or

$$\phi \leq 3^{\circ} \qquad (6\text{-}8)$$

However, it is sometimes desirable to process coherent intervals larger than the maximum interval without range walking even if separable processing is assumed. This has the advantage of a better azimuth resolution, although it will be subjected to some blurring due to the range walking introduced. The quantitative analysis of the interaction between the range walking and azimuth bandwidth will not be pursued here. It is pointed out, however, that if one were willing to use a non-separate model to process the data, then as long as the target reflectivity function could be reasonably assumed to be constant within the coherent azimuth interval, the interval processed could be as large as possible without actually suffering from range walking problem. This approach would yield optimum DOF of the final images and hence better resolutions. It would, of course, demand much more computational requirement as described in Chapter 2 and was not adopted in our experiments.

In our experiments the data in the ring area in Fig. 5-3 was divided into possibly overlapped azimuthal sectors. Each sector is individually Fourier transformed along azimuth (recall we have performed range Fourier transformation in 6.2.3) and only the magnitude part which is of our interest is kept to give target "looks" at the respective aspect angles. Figure 6-3(a) shows the image looks centered at 0^o, 30^o, 60^o, 120^o and 150^o with the azimuthal coherent interval being 3.2^o or 16 points. Figure 6-3(b) and 6-3(c) are looks at the same angle with 6.4^o and 12.8^o coherent intervals, respectively. Note the different relative scales between azimuth and range in Fig. 6-3(a), (b) and (c) in which figure 6-3(a) and 6-3(b) have been two-dimensionally linearly interpolated at a factor of 4 and 2 respectively to fully utilize the dimension of the displaying monitor from which all of our 2-D images were shot. In all the image looks of Fig. 6-3 the radar is to the right. Salient features of the airplane, e.g., the nose, the tail, the delta wing and the fuselage can be readily identified at appropriate looks. For example, at 0^o the target is sitting with nose on the radar. The images, which show reflectivities of the target, have a very large dynamic range of brightness and the sidelobe effects are very serious which manifest themselves as cross-like structures running horizontally and vertically, corresponding to the two dimensions of processing. Theoretically, images without sidelobes could be obtained only from all of the data points in the whole frequency domain which extends from $-\infty$ to ∞ in both dimensions. In reality

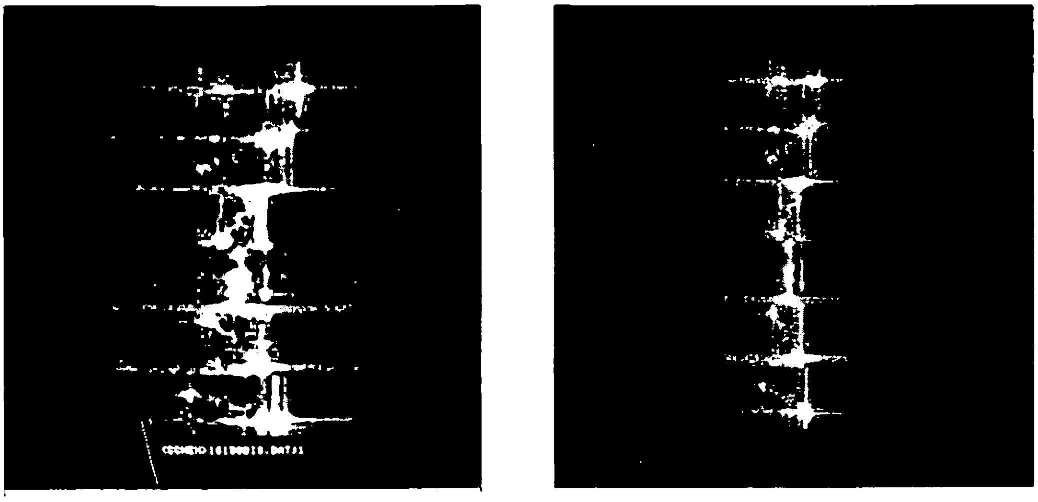

a) Azimuth coherence intervals = 3.2°
(16 points)

b) Azimuth coherence intervals = 6.4°
(32 points)

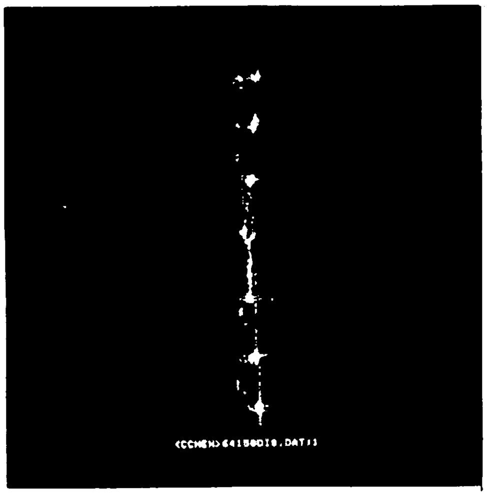

c) Azimuth coherence intervals = 12.8°
(64 points)

Fig. 6-3. Model F-102 azimuth images at 0°,30°,60°, 90°,120° and 150° aspect angles our data for each look comes only from an approximately rectangular area of the frequency space. This means, equivalently, a rectangular function has been multiplied with the data on the otherwise infinitely-extended data space. In the spatial domain the effect is as if the ideal images had been convolved with the Fourier transformation of a 2-D rectangular function, which is a sinc function. The sinc function has a first sidelobe of 13.4 dB below the main lobe level. Compared to the 30 dB dynamic range of the strength of the target reflectivities, the -13.4 dB sidelobe could completely mask the weak signals close to the strong ones. To alleviate the sidelobe problem, a well-shaped function should be multiplied to the data before Fourier transformation is taken [6-2]. Figure 6-4 shows the image looks when a two-dimensional Hanning window, which has a first sidelobe less than -30 dB, is incorporated into the data. Comparing Fig. 6-3(b) and Fig. 6-4 it is seen that the sidelobes have been reduced and the main lobe width slightly increased as predicted in [6-2].

To verify that the Hanning windowed Fourier transformation is a valid image reconstruction technique, Fig. 6-5, a sequence of 28 abutting looks with each look occupying 6.4° of data azimuthally, is presented. The rotation of the fuselage is very clear as it goes from 0° to 180° in the consecutive looks. In all the following experiments the Hanning window is always incorporated in the FFT's.

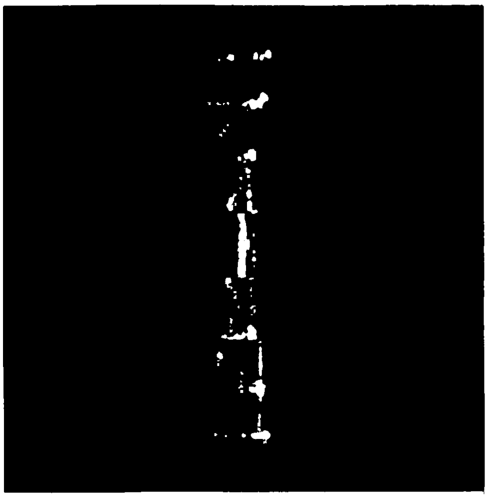

Fig. 6-4. Azimuth images of model F-102 at 0°,30°, 60°,90°,120°,150° and 180°; Hanning window incorporated; aspect coherence intervals: 6.4°

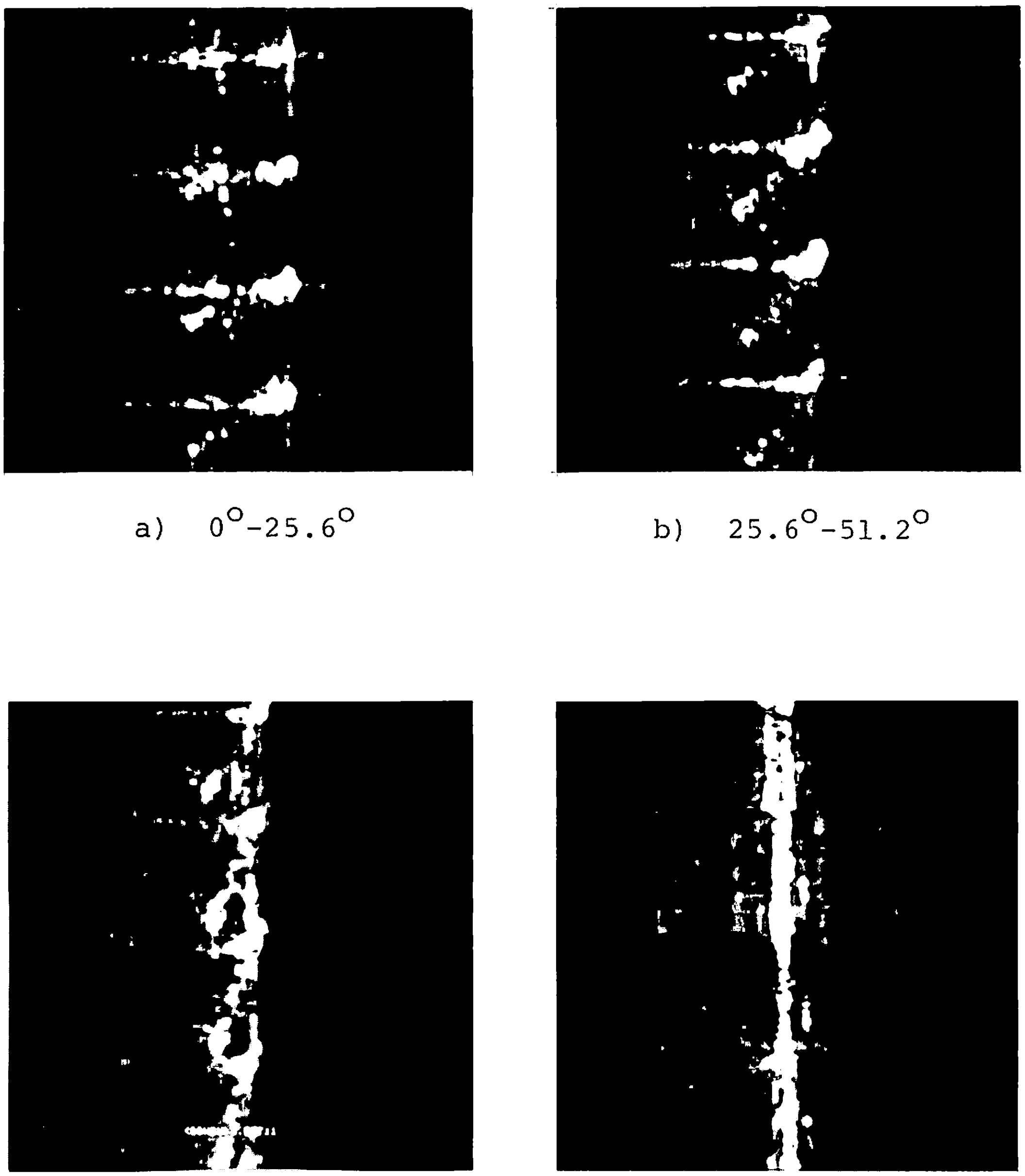

a) 0°-25.6°

b) 25.6°-51.2°

c) 51.2°-76.8°

d) 76.8°-102.4°

Fig. 6-5. Consecutive 6.4° abutting azimuth looks of model F-102; 28 looks total

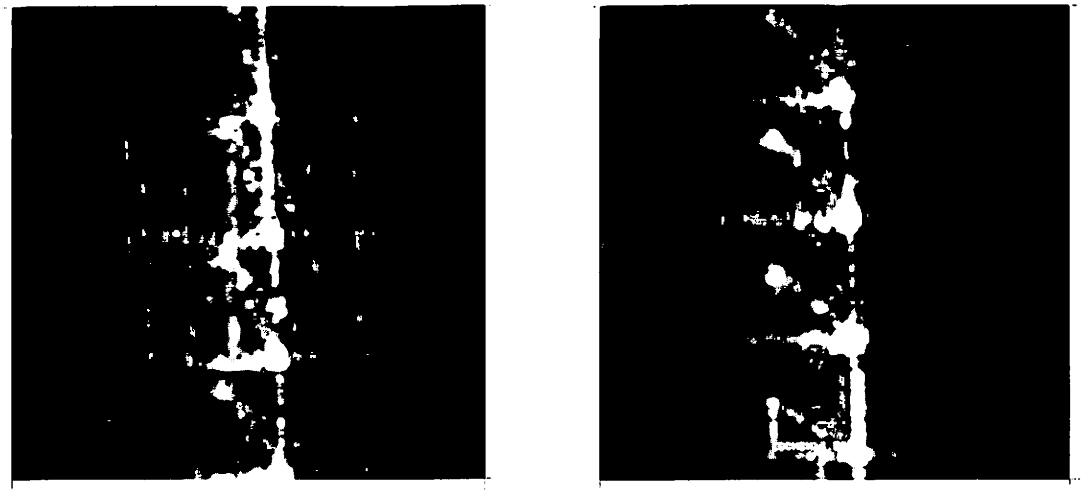

e) 102.4°-128°　　f) 128°-153.6°

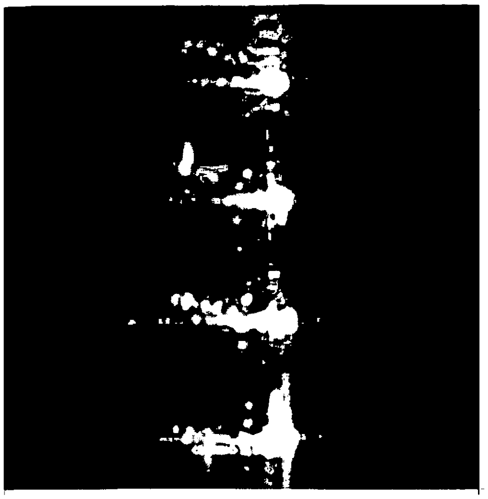

g) 153.6°-179.2°

Fig. 6-5. (Continued)

6.2.5 Incoherent summation of the looks

Because of the specularity of the target, each look in Fig. 6-5 shows only those target points which contribute coherently to the radar returns at the particular aspect angle. It is reasoned that a suitable combination of different looks should give a much enhanced overall target image. Indeed, we used the following procedure to accomplish this:

(1) determine the center of rotation for each look (and hence all of the looks since the distance between the radar and the rotation center is fixed upon the data collecting).

(2) rotate each look according to their respective aspect angle.

(3) incoherently sum the rotated and registered looks i.e. only the magnitude part of each look is used in the summation.

An additional advantage of the incoherent summation is the reduction of the "speckles" due to the phase errors in coherent systems.

In the case of "azimuth imaging", (i.e. horizontal setup of target), the images obtained from 180° orientation are always flipped for the other 180° and added for symmetry after the incoherent summation.

There are three parameters independently "tuned" to reach final summed images:

(1) the coherence interval in the azimuth direction.

(2) the amount of sector overlapping for adjacent looks.

(3) the center of rotation assumed in all looks.

Each of the above parameters is tested in our experiments to show how they affect the image quality.

Figure 6-6 through 6-8 test the parameters (1) and (2). Overlapping factors of abutting, 50% overlap and 90% overlap and coherence intervals of 3.2^o, 6.4^o and 12.8^o are adopted in these figures. Figure 6-9 test different rotation centers (different range bins) when the other parameters are fixed. The image quality seems to be relatively insensitive to the rotation center of each look compared to the case of F-5E imaging to be discussed later. Generally speaking, the experimental results show considerable improvement over the single-look images and clearly show the outline of the characteristic delta wing of the F-102 aircraft.

6.2.6 Imaging the vertical model F-102

The imaging principle of the RAT SCAT is that the information of the target reflectivity on the plane of the rotation can be resolved. In other words the images should outline the vertical projections of the target on the ground. Thus by using the data gathered from the target airplanes which sat vertically (i.e., roll angle = 90^o) one

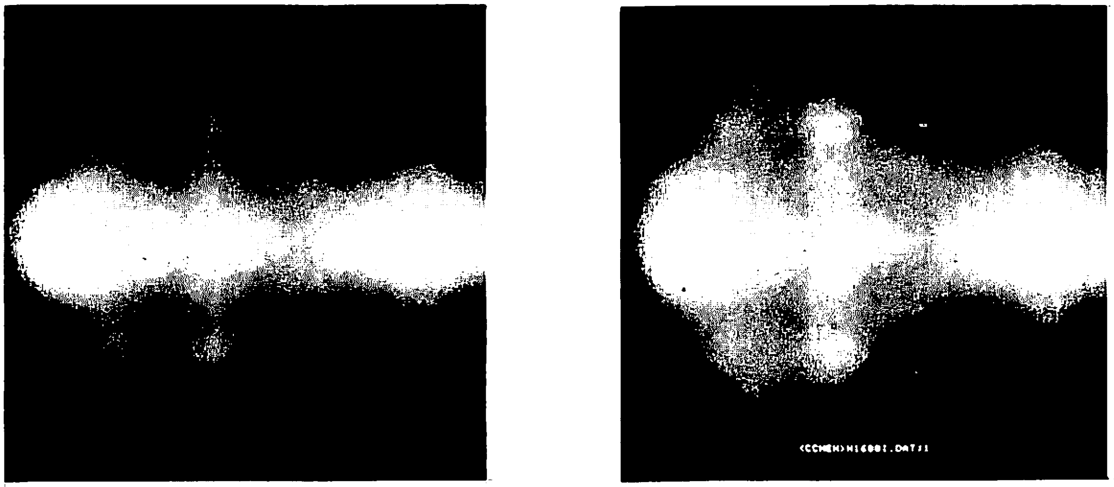

a) Abutting

b) 50% overlapping

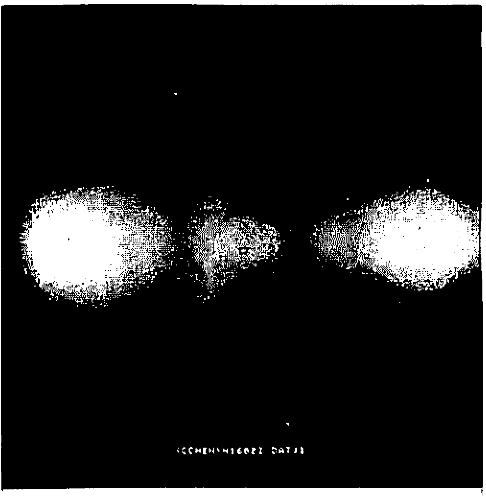

c) 90% overlapping

Fig. 6-6. Incoherently integrated azimuth images of model F-102 with different overlapping factors
aspect coherence intervals = 3.2°
centers of rotation = range bin number 188

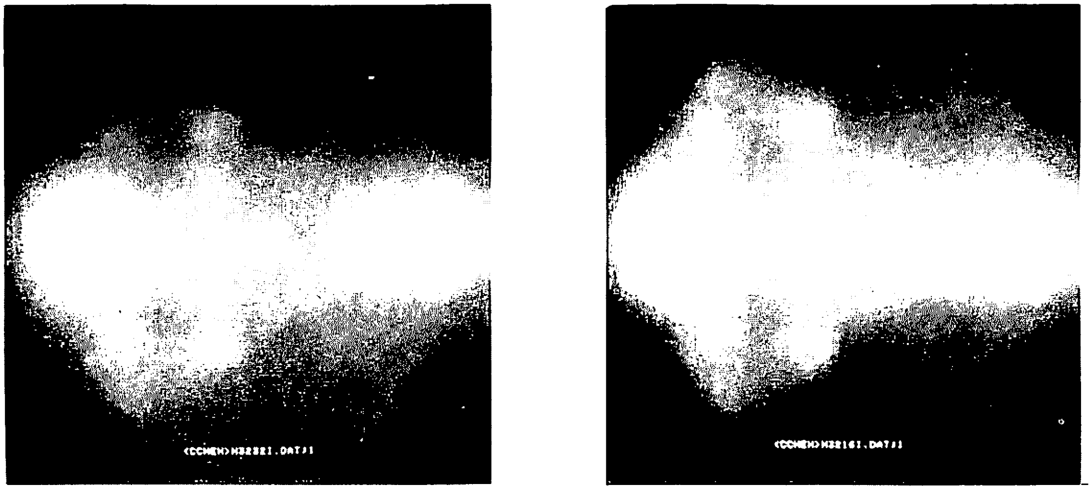

a) Abutting

b) 50% overlapping

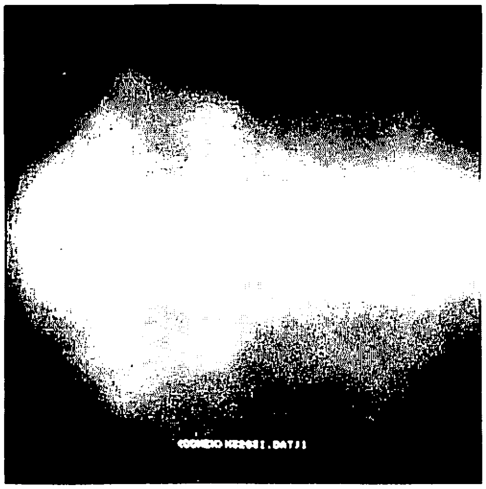

c) 90% overlapping

Fig. 6-7. Counterparts of Fig. 6-6 with 6.4° aspect coherence intervals. (all other parameters same as Fig. 6-6)

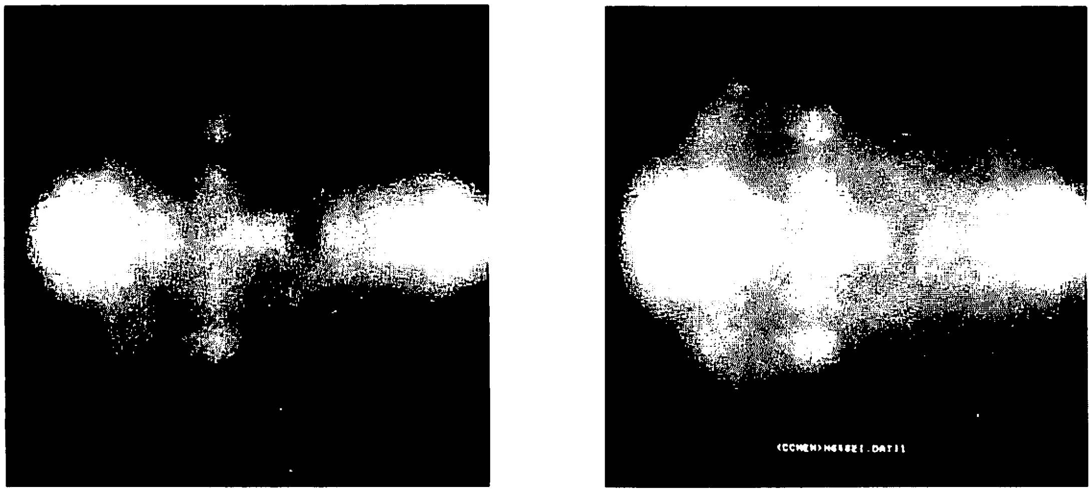

a) Abutting

b) 50% overlapping

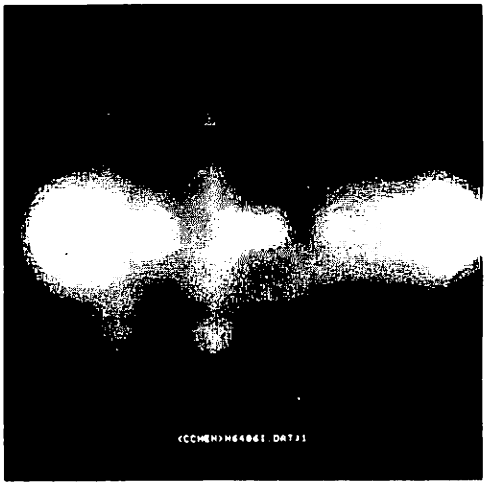

c) 90% overlapping

Fig. 6-8. Counterparts of Figs. 6-6 and 6-7 with 12.8° aspect coherence intervals. (all other parameters same as Figs. 6-6 and 6-7)

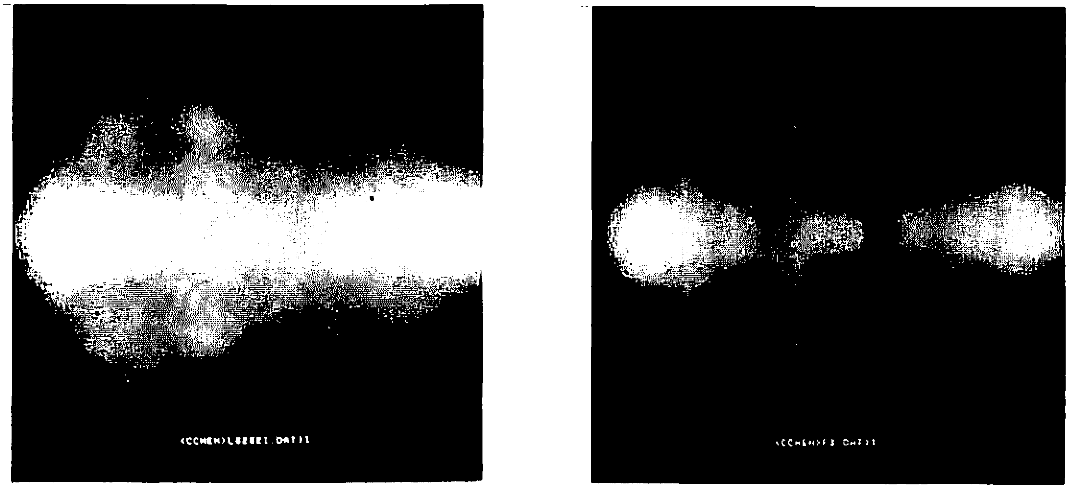

a) Centered at range bin 187

b) Centered at range bin 188

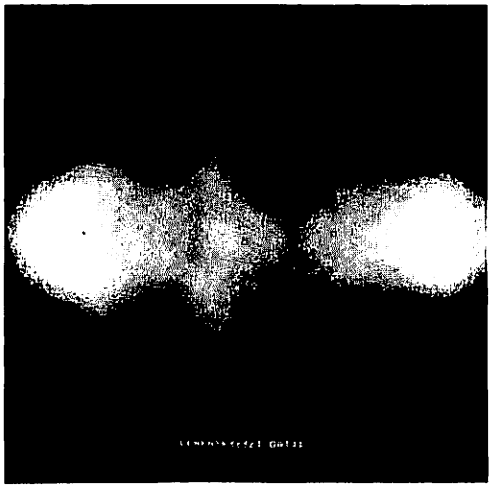

c) Centered at range bin 189

Fig. 6-9. Incoherently integrated azimuth images of model F-102 with different centers of rotation aspect coherence intervals 6.4° overlapping factor: abutting should come up with the "side view" or elevation image of the airplane. The processing principles are much the same as described before. However in this setup the radar images are not symmetric anymore so the data from the full 360° rotation is necessary for our reconstruction algorithm of incoherently summing different looks.

Figure 6-10 shows the result of the model F-102 from the vertical setup. The azimuth coherence intervals were 6.4°, the looks were abutting and the center of rotation was at range bin number 178.

6.3 Imaging the Model F-5E

The same processing techniques were applied to an F-5E model airplane which has a different shape and size from those of the F-102. The size of the model target is 0.30 times that of an actual plane which is approximately 48 feet in length and 26 feet from wing tip to wing tip. γ_1 and γ_2 were unknown constants while other parameters were the same as those in the case of the model F-102.

In the following experiments the target was assumed in a horizontal position (0° roll) unless otherwise stated.

Figure 6-11 shows a resultant sequence of 14 looks with abutting 6.4° coherence intervals, covering 0° to 90° aspect angles. Note the rotation of the fuselage along the consecutive looks. Again the radar was to the right for each look so the right wingtip can be identified in the

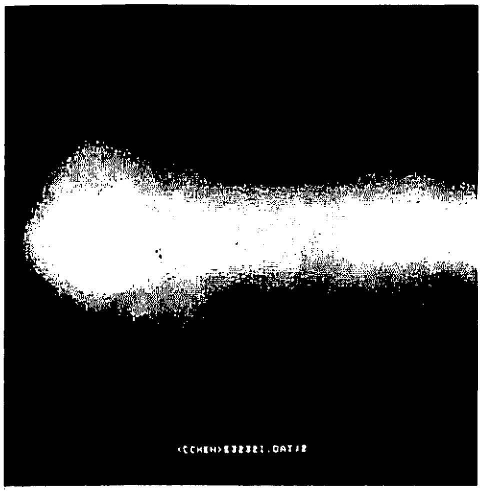

a) Abutting

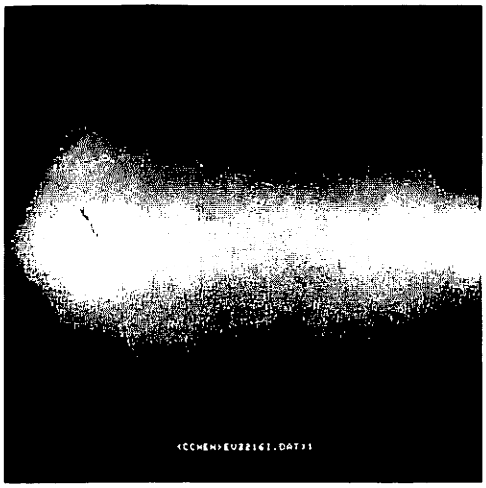

b) 50% overlapping

Fig. 6-10. Elevation images of model F-102 with
different overlapping factors; aspect
coherence intervals: 6.4°
centers of rotation: range bin number
188

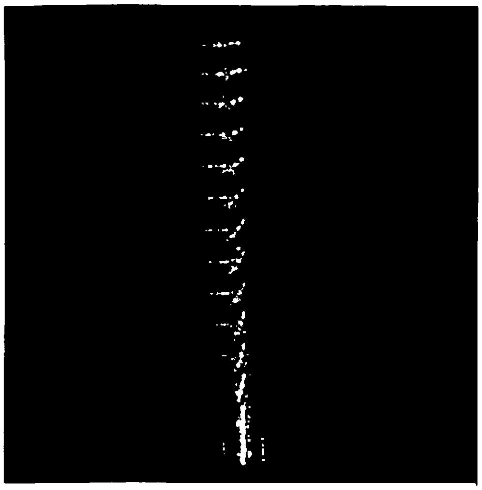

Fig. 6-11. A sequence of 14 azimuth looks from 0° to 90° aspect angles for model F-5E

last few looks in which the target was approximately broadsided to the radar. The other 14 looks covering 90^{o} through 180^{o} aspect angles, which are not shown here, have the corresponding orientation of the previous looks. These 28 looks were incoherently combined and flipped for symmetry with the rotation center being at range bin number 177.25 to become Fig. 6-12. Note the protrudent wings of this aircraft as opposed to the delta wings of an F-102. As mentioned before, the quality of the image for the model F-5E seems more sensitive to the rotation centered assumed; at approximately 4 bins (center at #181) off the true center the target image looks like a big blub as in Fig. 6-13. Figure 6-14 is a fine tuning of the rotation center at 0.25 range bin resolution.

Figure 6-15 shows the effect of the overlapping factor between adjacent looks.

Figure 6-16 are the elevation images of the target with a vertical position of the target. The images are centered at range bin number 178 with different amounts of overlapping.

6.4 Comparison Between the Model F-102 and F-5E Images

Figure 6-17 presents a summary of photographs for the model F-102 and model F-5E airframes for both azimuth and elevation plots. The photographs show the distinct shapes of the wings of the two aircraft. Except for a slight

Fig. 6-12. Model F-5E azimuth image aspect
coherence intervals 3.2°
overlapping factor: abutting
center of rotation: range bin 177.25

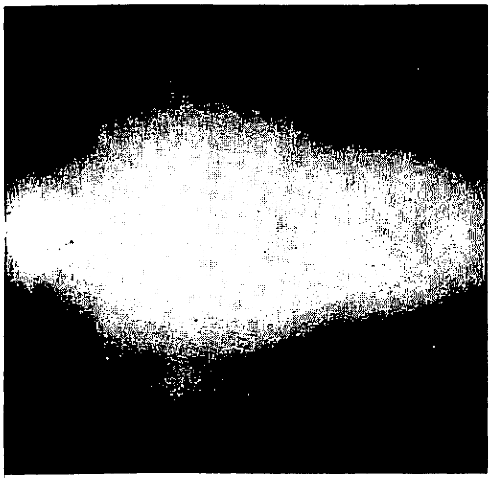

Fig. 6-13. Same as Fig. 6-12 except:
center of rotation: range bin 181

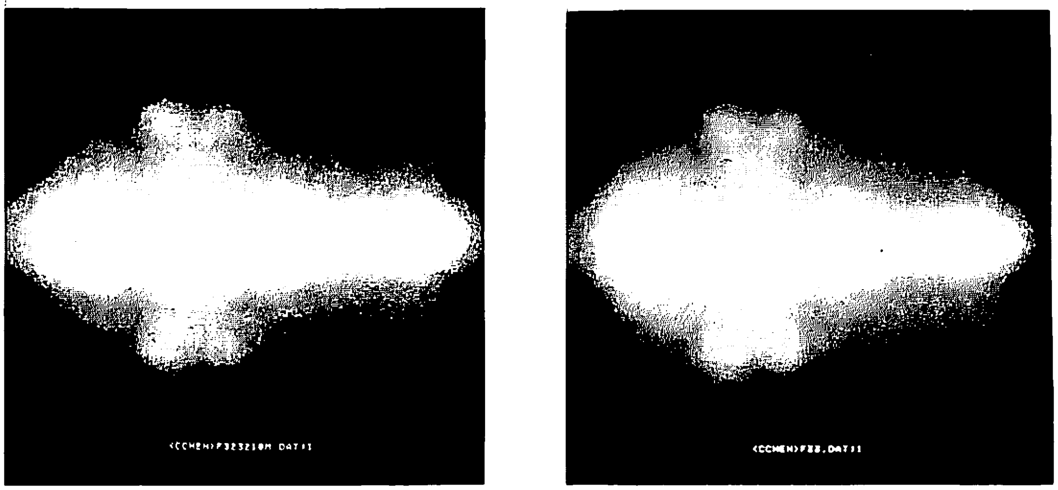

a) Centered at range bin 177

b) Centered at range bin 177.25

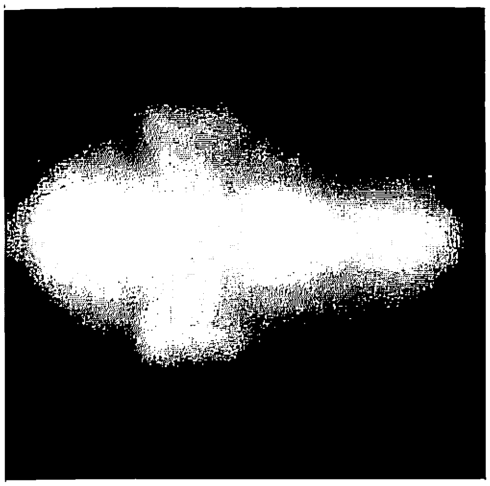

c) Centered at range bin 177.5

Fig. 6-14. Fine tuning of the rotation center for model F-5E azimuth images

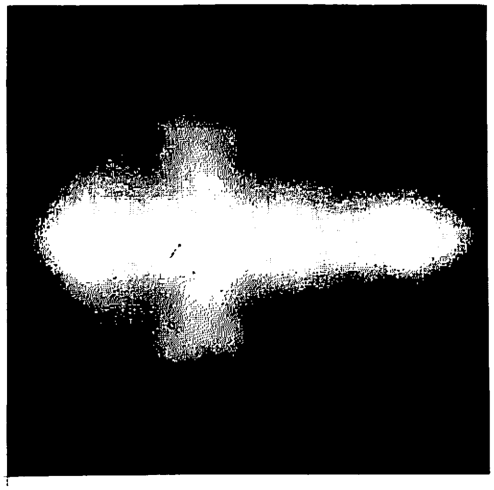

a) 50% overlapping

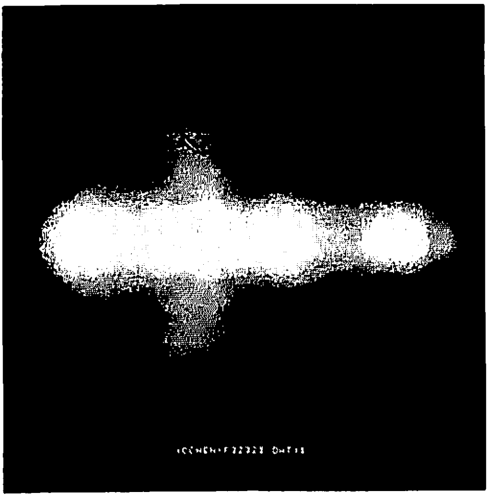

b) Abutting

Fig. 6-15. Effect of overlapping factors for model F-5E azimuth images
aspect coherence intervals: 6.4°
centers of rotation: range bin 178

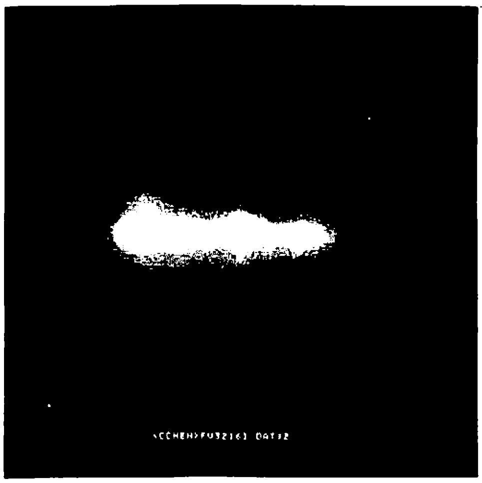

a) 50% overlapping

b) Abutting

Fig. 6-16. Model F-5E elevation images with
different overlapping factors.
aspect coherence intervals 6.4°
centers of rotation: range bin 178

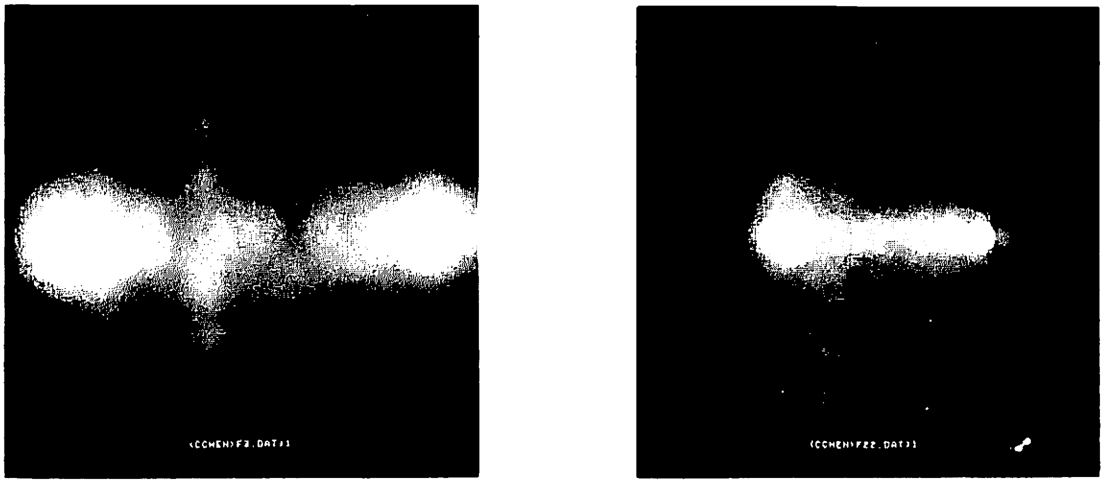

a) F-102 azimuth image
(28 looks)

b) F-102 elevation image
(56 looks) (1/2 scale)

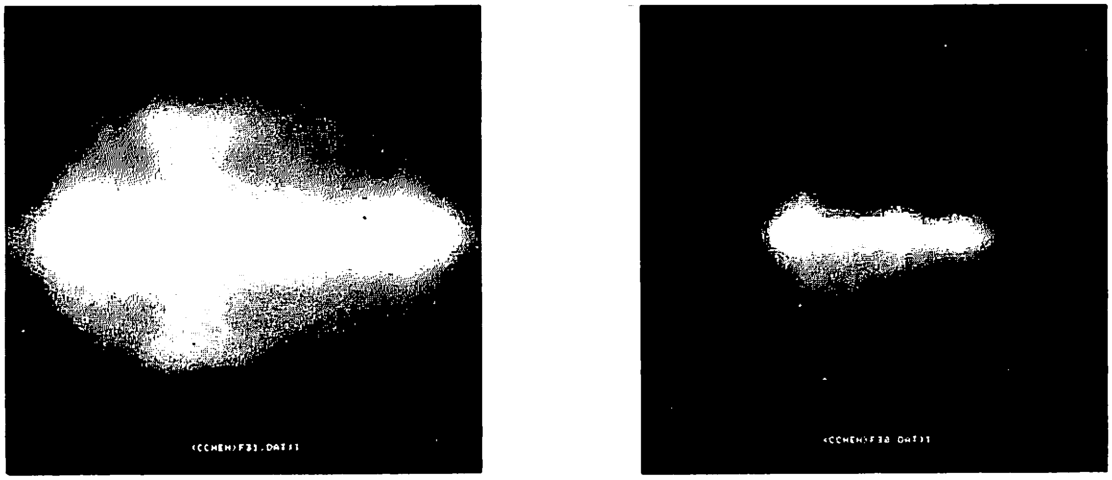

c) F-5E azimuth image
(28 looks)

d) F-5E elevation image
(56 looks) (1/2 scale)

Fig. 6-17. Model F-102 and model F-5E azimuth and elevation images (6.4° coherence) difference of the physical scales of these models (0.29 vs 0.30) all other parameters are fixed for these images. Consequently, it is clear that the F-5E is a smaller aircraft and naturally has a different azimuth and elevation projection than does the F-102.

6.5 Imaging a Real F-102 Airplane

The third target imaged was a full-sized real F-102 airplane. In this case, γ_0, f_{min} and Δf_r were changed to 5,552 ft., 2,744 MHz and 1,000 kHz, respectively to account for the large size of the real plane. γ_1 and γ_2 were unknown constants and other parameters remained the same as in the previous cases. From the parameters it is found that the unambiguous range interval I_r is

$$I_r = \frac{c}{2\times\Delta f_r} \cong 449 \text{ ft.}$$

and the range bandwidth is

$$B_r = 256 \times 1{,}000 \text{ kHz} = 256 \text{ MHz}$$

which has an ideal range resolution of

$$\rho_r = \frac{c}{2B_r} = 1.76 \text{ ft.}$$

The data ring in Fig. 5-3 has a smaller radius and width, hence smaller area than in the cases of model aircraft. However, because of the larger size of the target, the correlation field in the data space has a smaller "effective" autocorrelation region and thus the DOF in the small data ring is approximately the same as in the model airplane cases because of the cancellation of the scaling factors. Thus it is expected that the quality of the target images should be about the same. Roughly speaking, a target of larger spatial extent needs a narrower sampling interval in the frequency data domain to avoid any aliasing effect. Consequently the area in the sampled data domain would be smaller if the same number (DOF) of independent data points which determines the quality of the final images is to be present.

Figure 6-18 presents some photographs of the real F-102 radar images at different rotation centers. As predicted, the images qualities are about the same as those in Fig. 6-9. Again, here the delta wing structure is clearly visible.

6.6 Summary and Conclusions

Reconstruction of the reflectivity function of three airplanes is attempted experimentally in this chapter. Three major parameters of the reconstruction algorithms proposed in Chapter 5 are tested. They are: aspect coherence interval (the optimal value of which is determined by the interaction between the azimuth resolution and the range walking when separable processing is assumed), factor of overlapping between adjacent looks, and location

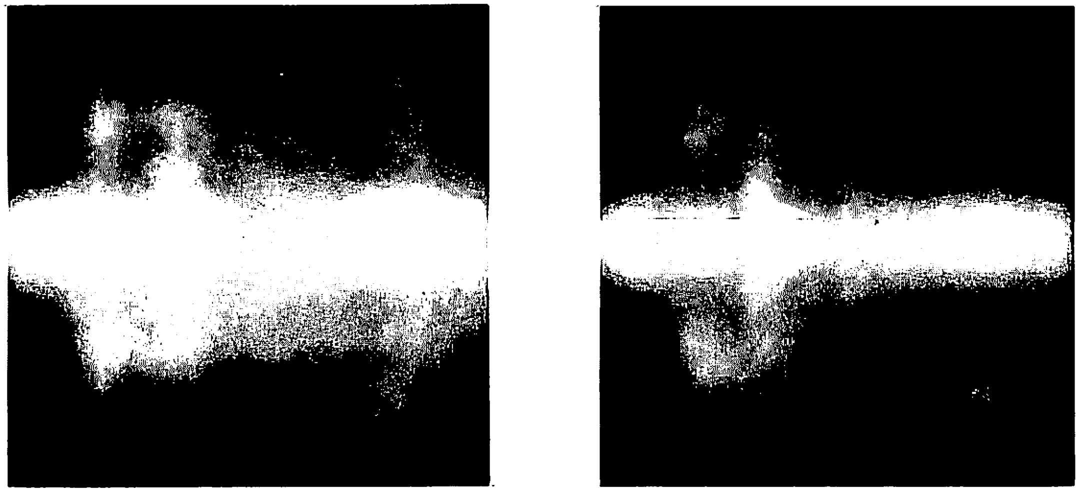

a) Centered at range bin 229

b) Centered at range bin 230

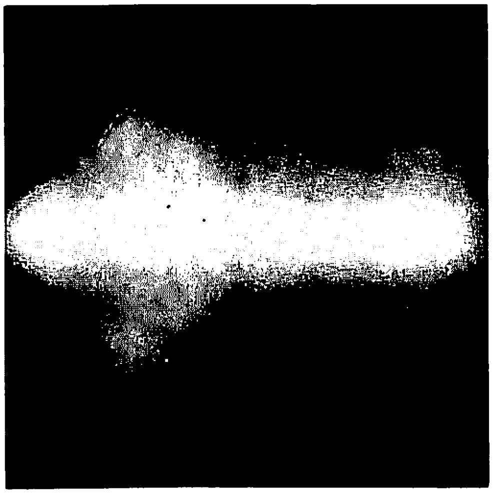

c) Centered at range bin 231

Fig. 6-18. Images of real F-102 with different centers of rotation; aspect coherence intervals 6.4° overlapping factor: abutting of the rotation center which has a "focusing" effect. As it turns out, some targets are sensitive to some of the parameters while insensitive to others. It is very difficult to predict what parameters should be used in a given imaging condition. For our purpose of obtaining the "best" images judged by human perception, trial and error seems to be the only feasible way at the present time.

In the final stage of our experiments to take pictures off the TV monitor for display, most factors of the shooting conditions were well controlled and calibrated. In fact, most of our images were taken from the same camera at fixed focal length, shutter speed and aperture. The brightness and the contrast on the monitor were fixed within the accuracy of the monitor operation. The background intensity has always been kept as low as possible. The major nonuniformity of the pictures so presented, if any, is conjectured due mainly to the films because of the film grain noise and possible difference in the sensitivity to the exposure.

Chapter 7

RADAR IMAGING WITH TARGET MOTION

7.1 Introduction

Imaging from ground-based (stationary) radars of moving targets is often possible by utilizing a "synthetic aperture" developed from the target motion itself, or sometimes called "inverse SAR" for the obvious reason. This chapter addresses the theory about a ground-based radar imaging system in which a target aircraft is imaged by its own motion induced doppler. The aircraft is imaged from both a straight flight and a turn with recognizable results. Analysis shows that two phase components exist in the radar return, one being gross velocity induced, the other being interscatterer interference within the target itself. The former phase must be removed prior to imaging and techniques are developed for this task. Preprocessing, range curvature, range alignment, motion compensation, and presuming are all addressed in this chapter.

7.2 Radar Imaging Equations

Figure 7-1 shows the flight path of a target aircraft which has an overall length of approximately 80 feet and wing span of about 70 feet. Two portions of the flight path

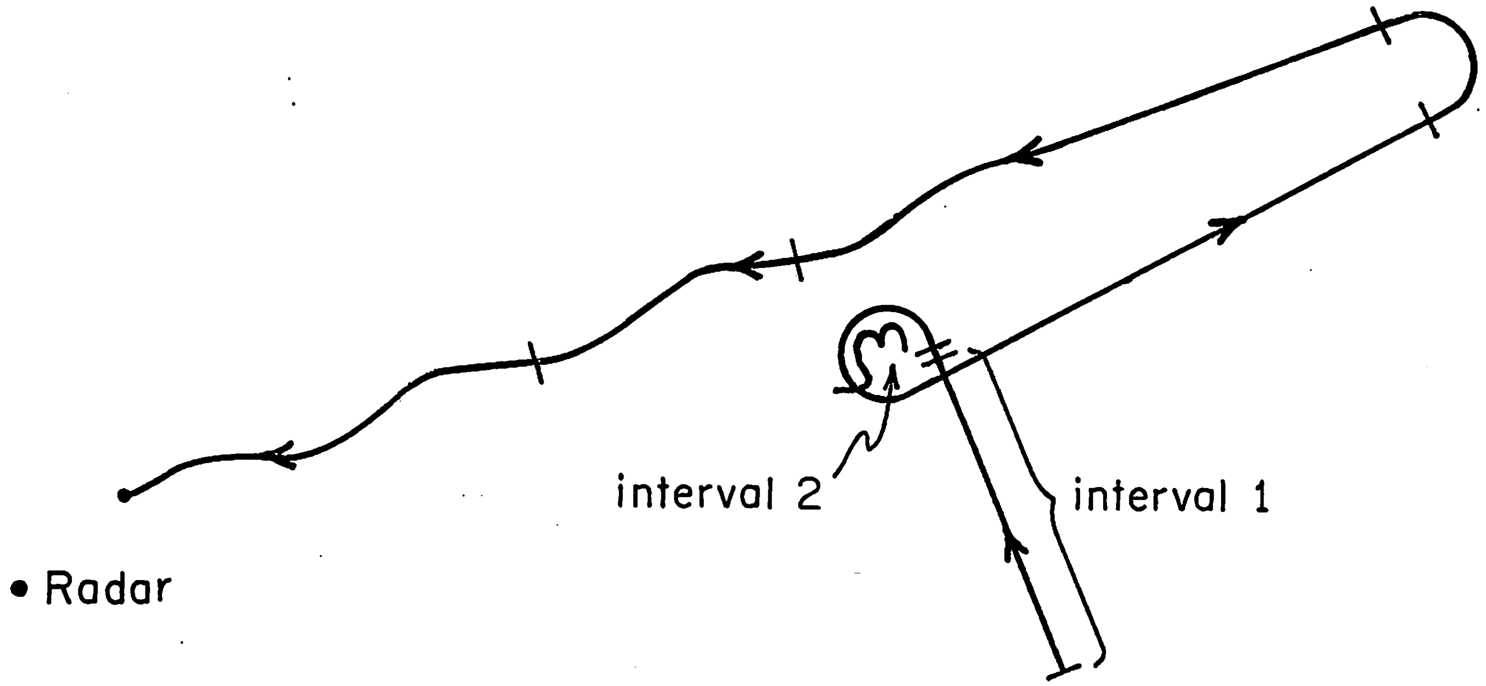

Fig. 7-1. Overall flight path of target

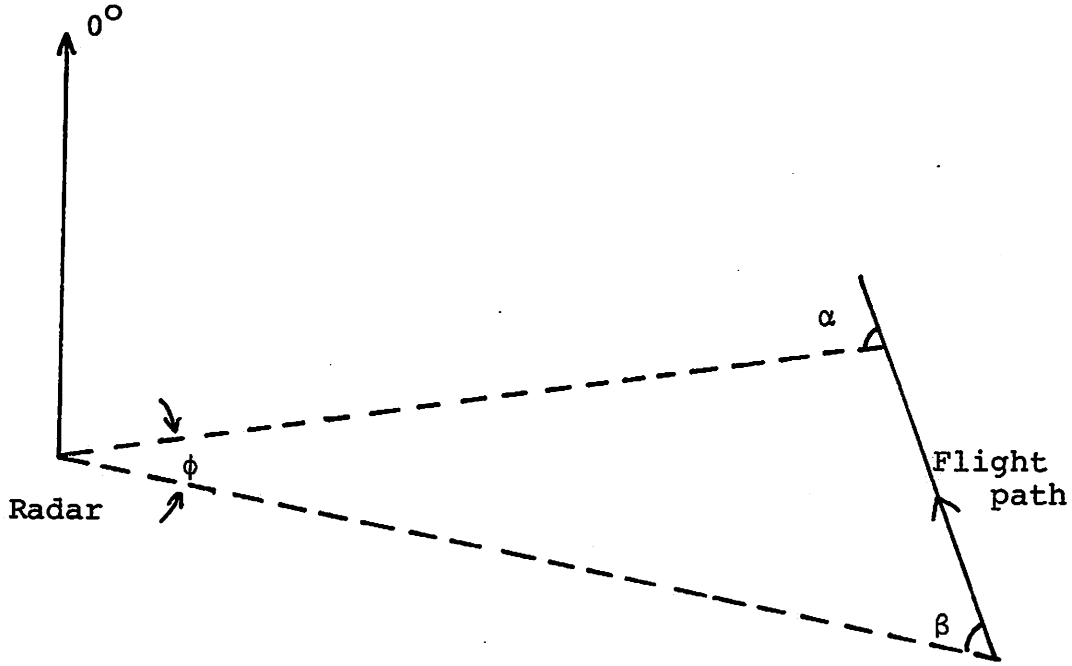

Fig. 7-2. Flight geometry of first inteval
$\phi = \alpha - \beta$

along which the data were obtained for imaging will be called interval 1 and interval 2, as shown in Fig. 7-1. The first interval is when the airplane was flying straight, at angles approximately 30° to 15° off broadwide, whereby the second interval occurs when the airplane was making a standard left turn.

7.2.1 First interval

Figure 7-2 is a reproduction of the first interval of Fig. 7-1. The aspect angle of the target center viewed from the radar undergoes a change ϕ, which in this case is the same as the change of the aspect angle of the target body with respect to the radar line of sight (LOS) because of the straight flight. In fact, it can be shown that it is the latter, and not the former angle change, which provides the azimuthal information. For this reason, we redraw Fig. 7-2 using the target center as the origin of the coordinate system. This becomes Fig. 7-3. Observe a close resemblance to the rotational geometry of a turntable imaging system as in chapters 5 and 6 [7-1].

In Fig. 7-3 let coordinates (ξ,η) be fixed on the target and (x,y) be rotating with the radar and with the same origin 0 as (ξ,η). Let the angle from axes ξ to x be θ. Then we have

$$\begin{aligned} x &= \xi\cos\theta+\eta\sin\theta & & \xi = x\cos\theta-y\sin\theta \\ & & \text{or} & \\ y &= -\xi\sin\theta+\eta\cos\theta & & \eta = x\sin\theta+y\cos\theta \end{aligned} \qquad (7\text{-}1)$$

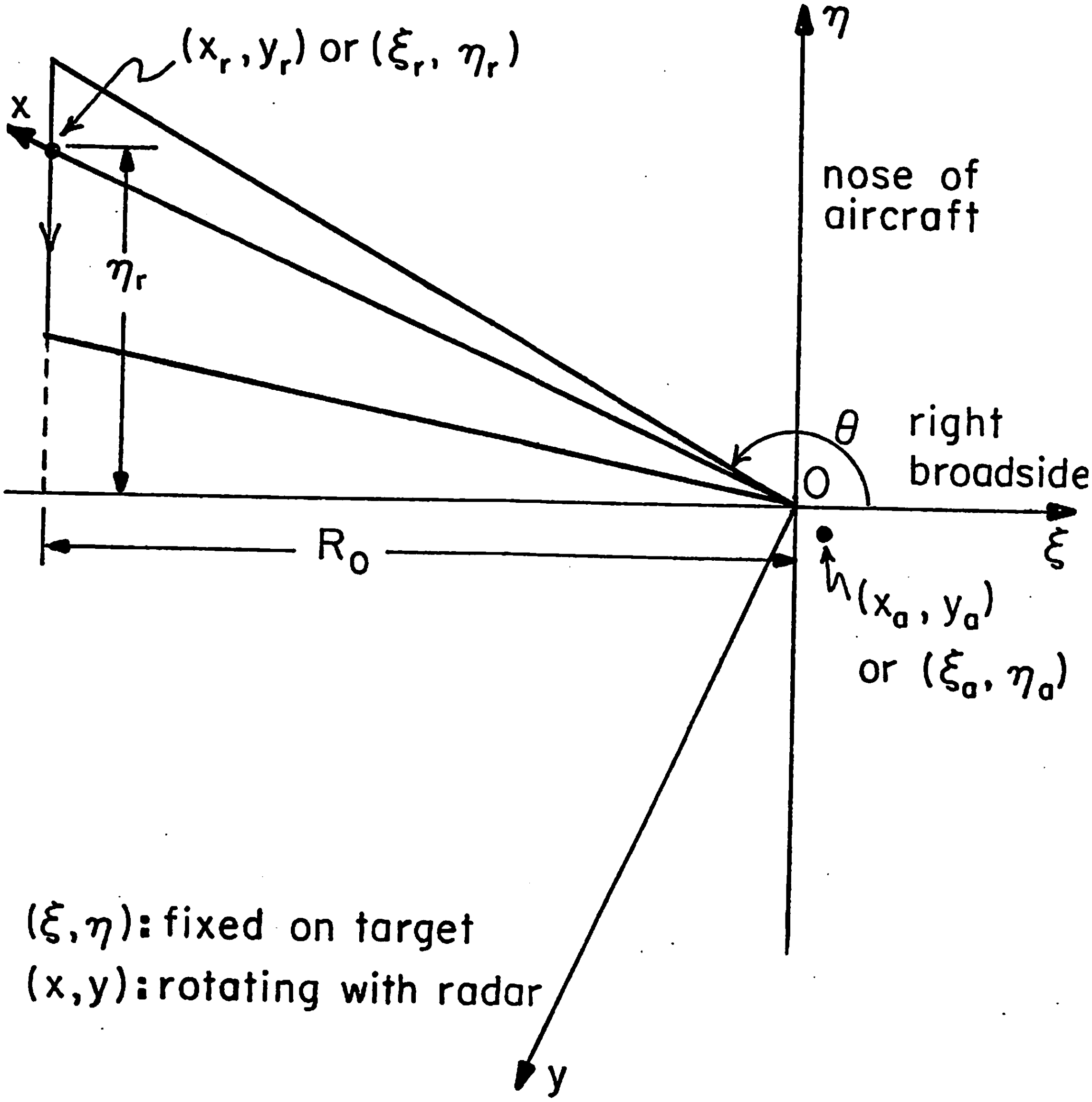

Fig. 7-3. Radar trajectory relative to target center in first interval

Let (x_r,y_r) or (ξ_r,η_r) be the coordinates of the radar and (x_a,y_a) or (ξ_a,η_a) be those of any target point. Note that $y_r = 0$ identically. Let ξ_{r_o} be the ξ coordinate of the radar had the airplane flown to the position broadwide to the radar and define $R_o \triangleq |\xi_{r_0}|$. Let $s(x_a,y_a,x_r,y_r)$ be the distance between (x_a,y_a) and (x_r,y_r). Then

$$\begin{aligned} s(x_a,y_a,x_r,y_r) &= \left[(x_a-x_r)^2+(y_a-y_r)^2\right]^{\frac{1}{2}} \\ &= \left(x_r^2-2x_rx_a+x_a^2+y_a^2\right)^{\frac{1}{2}} \\ &\simeq \left(x_r^2-2x_rx_a\right)^{\frac{1}{2}} \qquad (7\text{-}2) \\ &\simeq x_r-\frac{x_rx_a}{x_r} \\ &= x_r-x_a \end{aligned}$$

for target distance large enough such that $x_a^2+y_a^2 << x_r^2$. Note that x_r and x_a are both functions of time t.

As the flight goes by, the change in $s(x_a,y_a,x_r,y_r)$ induces a Doppler frequency of the target point at (x_a,y_a)

$$f_d(x_a,y_a) = \frac{2}{\lambda}\frac{ds}{dt} = \frac{2}{\lambda}\left(\frac{dx_r}{dt} - \frac{dx_a}{dt}\right) \qquad (7\text{-}3)$$

where λ is the wavelength of the transmitted signals.

Equation (7-3) has a very interesting interpretation. The Doppler frequency of the target point (x_a,y_a) is comprised of two part:

$f_{d_1} \triangleq \frac{2}{\lambda}\frac{dx_r}{dt}\left(\text{when } \frac{dx_a}{dt} = 0\right)$, due to the trajectory of the target center, and

$f_{d_2} \triangleq \frac{2}{\lambda}\frac{dx_a}{dt}\left(\text{when } \frac{dx_r}{dt} = 0\right)$, due to the relative motion of the target inter-scatterer points with respect to the target center. Recall that in the last two chapters the term $\frac{dx_r}{dt}$ was zero because the target was rotating on a table and hence x_r was a constant. Also in RAT SCAT $\frac{dx_a}{dt}$ is a constant because the rotation rate, or the step increment in aspect angle of the target is a constant. If we are to apply the techniques developed in turntable imaging to the underlying system, these two differences have to be compensated first.

Because

$$x_r = \left(R_o^2+\eta_r^2\right)^{\frac{1}{2}} = R_0+\frac{1}{2}\frac{\eta_r^2}{R_o}-\frac{1}{8}\frac{\eta_r^4}{R_o^3}+\cdots, \tag{7-4}$$

$$\frac{dx_r}{dt} = \frac{\eta_r}{R_o}\frac{d\eta_r}{dt} - \frac{1}{2}\frac{\eta_r^3}{R_o^3}\frac{d\eta_r}{dt} + \cdots \tag{7-5}$$

Assuming a constant flight speed v, from Fig. 7-3 we have $\frac{d\eta_r}{dt} = -v$ and hence

$$\frac{dx_r}{dt} = -\frac{\eta_r v}{R_o} + \frac{1}{2}\frac{v}{R_o^3}\eta_r^3 - \cdots \tag{7-6}$$

Thus the Doppler frequency induced by x_r is a linear function of η_r plus higher order terms and the phases of the return due to x_r are quadratic plus other higher order terms, the first two being of opposite signs. It is clear from Eq. (7-6) that as the aircraft flies closer to being broadside or normal to the radar LOS corresponding to a decreasing η_r, the linear relation between f_{d_1} and η_r is more precise. In that situation the "rate" in Doppler frequency

$$\frac{2}{\lambda}\frac{d^2x_r}{dt^2} = \frac{2}{\lambda}\left(\frac{v^2}{R_o} - \frac{3\eta_r^2v^2}{2R_o^3}\right) \tag{7-7}$$

becomes larger and larger and converges to a constant proportional to $\frac{v^2}{R_o}$, which in terms of signal processing is a linear FM rate.

Roughly speaking, the history of x_r does not provide useful imaging information but only serves as a carrier to carry $\frac{dx_a}{dt}$ which contributes to coherent imaging ability by providing a wide spectral bandwidth inherent in a linear FM signal. Upon reception, x_r phases should be removed first (sometimes called de-chirping or motion compensation) to ease the processing afterwards to extract the relevant azimuthal phase information in $\frac{dx_a}{dt}$. Schemes to remove these phases will be described in Section 7-5. We now analyze the higher order effects of $\frac{dx_a}{dt}$ which does not exist in RAT SCAT.

Since $x_a = \xi_a\cos\theta+\eta_a\sin\theta$,

$$\begin{aligned}\frac{2}{\lambda}\frac{dx_a}{dt} &= \frac{2}{\lambda}(-\xi_a\sin\theta+\eta_a\cos\theta)\frac{d\theta}{dt}\\ &= \frac{2y_a}{\lambda}\frac{d\theta}{dt}\end{aligned} \tag{7-8}$$

Also $\tan\theta = \frac{\eta_r}{\xi_{r_o}}$ or $\theta = \tan^{-1}\frac{\eta_r}{\xi_{r_o}}$

so

$$\frac{d\theta}{dt} = \frac{1}{1 + \frac{\eta_r^2}{\xi_{r_o}^2}} \cdot \frac{1}{\xi_{r_o}} (-v)$$

$$= \frac{v}{R_o} \cdot \frac{1}{1 + \frac{\eta_r^2}{R_o^2}} \tag{7-9}$$

Again, $\frac{d\theta}{dt}$ approaches maximum as the airplane flies normal (η_r=0) to the radar. In that case $\frac{d\theta}{dt} = \frac{v}{R_o}$ and

$$f_{d_2} = \frac{2y_a}{\lambda} \frac{v}{R_o} \tag{7-10}$$

This means that at positions close to broadside the doppler frequency of a single target point at (x_a, y_a) due to change in x_a is proportional to y_a and is independent of x_a. In this situation there is a one-dimensional (along y_a) Fourier transform relation between the returns and the target reflectivities. Over a wide range of the flight path, the factor $\frac{1}{1+\frac{\eta_r^2}{R_o^2}}$ could change so much as to affect the performance of the Fourier transform. However, over a small interval where $\frac{1}{1+\frac{\eta_r^2}{R_o^2}}$ is approximately constant and can thus be replaced by a nominal value, Fourier transform techniques can still be applied. Thus if one does not compensate for the above abnormality factor, there is a tradeoff between the resolution (determined by the aspect angle span coherently processed) and the fidelity of a Fourier transform. One way to compensate for this is to interpolate the azimuthal samples to obtain the data uniformly spaced in the azimuthal frequency domain. Another possibility is to use a variable PRF which follows $\frac{d\theta}{dt}$ or the rate of rotation of the target as seen from the radar. Note from Eq. (7-10) that an increase in v, or a decrease in λ or R_o will increase the obtainable resolution accompanied with a higher minimum PRF required. The λ-dependence will be further explained later. The "speckles" of the final images from the coherent processing could be removed somewhat by incoherently averaging different coherent looks, as in Chapters 5 and 6.

7.2.2 Second interval

The flight path of the second interval is depicted in Fig. 7-4 in which (ξ', η') are coordinates centered and fixed on the target and (x,y) are fixed on the radar with the origin o being the center of the turn. Let (ξ, η) be the coordinates parallel to (ξ', η'), with origin at o. Again let the coordinates of the radar and the target points have subscripts r and a, respectively. Because

$$\begin{aligned} \xi &= x\cos\theta - y\sin\theta \\ \eta &= x\sin\theta + y\cos\theta \end{aligned} \qquad (7\text{-}11)$$

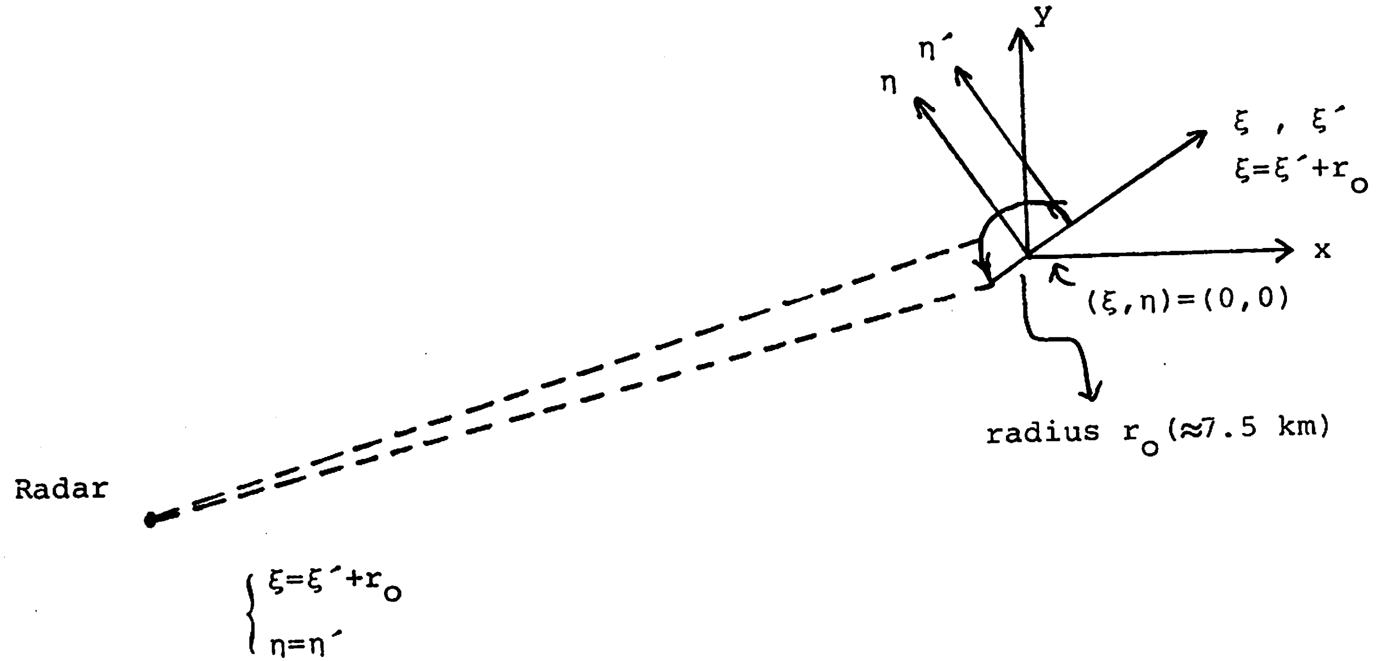

Fig. 7-4. Geometry of the flight in second interval

and $\begin{cases} \xi = \xi' + r_o \\ \eta = \eta' \end{cases}$, where r_o is the radius of the turn, we have

$$\begin{aligned} \xi' + r_o &= x\cos\theta - y\sin\theta \\ \eta' &= x\sin\theta + y\cos\theta \end{aligned}$$

or (7-12)

$$\begin{aligned} \xi' &= x\cos\theta - y\sin\theta - r_o \\ \eta' &= x\sin\theta + y\cos\theta \end{aligned}$$

which is the coordinate transformation relation between (ξ',η') and (x,y).

The distance between a target point at (ξ_a,η_a) and the radar at (ξ_r,η_r) is

$$\begin{aligned} s(\xi_a,\eta_a,\xi_r,\eta_r) &= [(\xi_a-\xi_r)^2+(\eta_a-\eta_r)^2]^{\frac{1}{2}} \\ &= [\xi_r^2+\eta_r^2-2\xi_a\xi_r-2\eta_a\eta_r+\xi_a^2+\eta_a^2]^{\frac{1}{2}} \\ &\simeq [\xi_r^2+\eta_r^2-2(\xi_a\xi_r+\eta_a\eta_r)]^{\frac{1}{2}} \qquad (7\text{-}13) \\ &\simeq (\xi_r^2+\eta_r^2)^{\frac{1}{2}} - \frac{\xi_a\xi_r+\eta_a\eta_r}{(\xi_r^2+\eta_r^2)^{\frac{1}{2}}} \\ &= R_o - \frac{\xi_a\xi_r+\eta_a\eta_r}{R_o} \end{aligned}$$

where $R_o \triangleq (x_r^2+y_r^2)^{\frac{1}{2}}$ is the distance between the center of the turn and the radar. In Eq. (7-13) we have assumed that the radius of the turn is small compared to R_o. The Doppler frequency of the point target at (ξ_a,η_a) is then

$$f_d(\xi_a,\eta_a) = \frac{2}{\lambda}\,\frac{ds(\xi_a,\eta_a,\xi_r,\eta_r)}{dt}$$

$$= \frac{2}{\lambda}\,\frac{ds}{d\theta}\,\frac{d\theta}{dt} \qquad (7\text{-}14)$$

where

$$\frac{ds}{d\theta} = \frac{1}{R_o}\,\frac{d[\xi_a(x_r\cos\theta - y_r\sin\theta) + \eta_a(x_r\sin\theta + y_r\cos\theta)]}{d\theta}$$

$$= \frac{1}{R_o}\,(-\xi_a\eta_r + \xi_a\eta_r) \qquad (7\text{-}15)$$

Let

$$(\xi_a,\eta_a) = r_a(\cos\theta_a, \sin\theta_a)$$

and

$$(\xi_r,\eta_r) = r_r(\cos\theta_r, \sin\theta_r) = R_o\ (\cos\theta_r, \sin\theta_r)$$

where r and θ are the polar coordinates with respect to the coordinates (ξ,η) with origin at 0. Then

$$\frac{ds}{d\theta} = \frac{1}{R_o}\,r_a \cdot R_o \sin(\theta_a - \theta_r) = r_a \cdot \sin(\theta_a - \theta_r) \qquad (7\text{-}16)$$

Equation (7-15), which assumes that $r_o << R_o$ as in Eq. (7-13), has the following interpretation: $\frac{ds}{d\theta}$ is proportional to r_a, the radial distance of the target point from origin 0 and is independnent of θ, modulated by a sinusoidal function of $\theta_a - \theta_r$. While θ_a is independent of θ, θ_r is a linear function of θ. Hence each target point has a sinusoidal range history. In the extreme case when $r_o = 0$, this would be the same as a turntable geometry. The effect of θ_r is to make the family of constant doppler lines rotated to the data returns with small aspect angle change*, the motion of the center of target, which is much more complicated in interval 2, has to be compensated. This will be discussed in subsequent sections.

7.3 Preprocessing

For most practical purposes, radar imaging systems which determine the relation between the data returns and the reflectivities of the target can be considered linear [7-2] and the system classification method developed in Chapter 2 [7-4] can be used to decide ways to reconstruct the reflectivities directly from the raw data. This situation is depicted in Fig. 7-5. The data return $g(x,y)$ is a linear transformation of target reflectivity function $f(\xi,\eta)$ through the radar signal radiation and the echo reception. For ease of presentation we will assume that both g and f in Fig. 7-5 are discrete so that the system can be represented by a matrix [H] and g and f by vectors as in Chapter 2. Depending on the waveforms of transmitted signals, (e.g., short pulse, linear FM pulse, or step-frequency waveforms) and the imaging geometries (e.g., shape and size of target, direction of relative motion, resolution required, etc.), the radar imaging systems represent a wide spectrum of the cases in [7-4]. Once the relation [H] between the reflectivity and data is

---

*Assuming no range curvature problem, as discussed later.

by an angle θ_r. Note that $\theta_a = 0$ for the target center and

$$\frac{ds}{d\theta} = -r_o \sin\theta_r \qquad (7\text{-}17)$$

is the range velocity of the target center. Obviously $\frac{ds}{d\theta} = 0$ at $\theta_r = 0^o$ and 180^o corresponding to broadside positions and is maximum in absolute value corresponding to head-on or tail-on positions.

In the case r_o is not small compared to R_o one can still, in principle, decompose $s(\xi_a, \eta_a, \xi_r, \eta_r)$ into two parts, one consisting of the pure target center motion and the other a rotating of the target as seen from the radar, to separate the relevant imaging information from the irrelevant trajectory information using the precise coordinate relation in Eq. (7-12). However, derivation of the exact expression is very complicated and tedious so we decided not to elaborate. The comment that is necessary is that the effective target rotation rate which determines the azimuth resolution is the sum of the aspect rate due to the turn itself (thus is uniform) and the aspect angle rate of the aircraft center as seen from the radar. If the maximum rate of target center aspect change which occurs at broadside is much smaller than the uniform turn rate , the effective aspect angle rate can be approximated by a constant, assuming constant radius and velocity of the turn.

As in Interval 1, before applying a Fourier transform (precisely) decided by the flight or radar data, a straightforward reconstruction of $\underline{f}$ and $\underline{g}$ can be achieved by applying the pseudoinverse of [H] to $\underline{g}$ yielding a minimum square error reconstruction. Methods of taking $[H]^-$ are readily provided by each of the nine cases in Chapter 2.

The above reconstruction scheme, although straightforward in theory, usually involves a great deal of computation because of the complexity of [H]. In the worst case, one would expect to resort to a full singular value decomposition (SVD) to find $[H]^{-1}$. Certainly a decomposition of [H] such that the structure of the imaging geometry can be better utilized would warrant the efforts in many cases.

A perceivable way to accomplish this is to do some preprocessing upon the raw data such that the resultant data has a much simplified relation to the reflectivity than the raw data itself. Diagrammatically, [H] can be replaced by a cascaded system of $[H_1]$ and $[H_2]$ as in Fig. 7-6 or Fig. 2-2(d) and $\underline{f}$ can be estimated by multiplying $[H_2]^{-1}$, followed by $[H_1]^{-1}$, to $\underline{g}$ with the hope that $[H_1]$ would be so simplified in structure or so small in size compared to [H] that the extra effort on obtaining $[H_2]^{-1}$ would be warranted. For this purpose $[H_2]^{-1}$ is called preprocessing. Examples of $[H_2]^{-1}$ are: range alignment, presumming, de-chirping, and general motion compensation. Some of them will be discussed in the

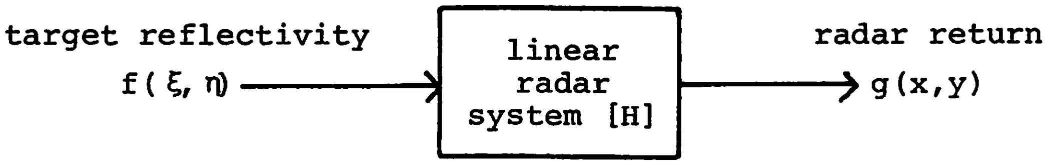

$\underline{g} = [H]\ \underline{f}$

$[H]$: Point spread function matrix (PSF)

$[H][H]^t$: correlation matrix

- determines systems degrees of freedom (DOF).

Fig. 7-5. Linear radar imaging system

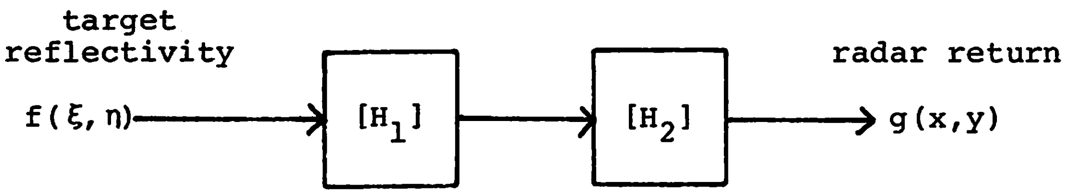

$[H_2]^{-1}$: Preprocessing

- Range alignment
- Range curvature elimination
- Motion Compensation
- Presuming

$[H_1]^{-1}$: Ideally a Fourier transform

Fig. 7-6. Decomposition of [H] in Fig. 7-5 following sections.

7.4 Range Curvature and Range Bin Alignment

In general, the radar return of the signal pulse from the target provides the range information while the history of the returns along some range bin provide azimuthal information. These two sources of information could have been coupled such that a separable or even separate processing [7-4] would not be adequate to recover the information to the extent of accuracy one pursues. There are two major sources of non-separability in the radar imaging system: range curvature and range misalignment. We will describe the phenomena and propose methods to avoid or correct them.

7.4.1 Range curvature

A single radar pulse return contains the information about the surfaces or lines whose points are equi-distant from the radar transmitter or receiver. These surfaces or lines can be resolved by the timing (for short pulse) or range compression (for long duration linear FM-like pulse) or even synthetic range profiles (for MFS pulses) techniques. Since the range direction has been compressed and resolved in our source data, the simplest way to resolve the azimuth would be to do one-dimensional processing along cross range direction. This requires that each particular point has contribution to only those range bins which are aligned for azimuthal processing. Such is the case for low or medium resolution SAR imaging with aligned returns. As the resolution requirement becomes greater and greater one is usually forced to reduce the range bin width and/or to increase the azimuthal interval over which the data are to be processed coherently. Both of these would eventually create range curvature problem since the surfaces of constant range as mapped on the target move further away as the relative motion between the radar and the target continues.

There are two effects as one increases the azimuthal coherence interval: increased bandwidth and range curvature. In addition, the amount of computation increases with the signal bandwidth. Assuming separable processing there is a tradeoff as to how far one should increase the coherence interval without too serious a range curvature problem. There have been few quantitative criteria proposed for optimizing this tradeoff, especially when the computational factor is also considered.

It is, however, much easier to find the critical condition under which the range curvature starts to occur. This is whenever any target point of interest has a range variation of more than, say, 1 range bin width, so that the point has contribution to more than 1 range bin. This condition can be derived from the geometry of imaging, as in Chapters 5 and 6.

Since range curvature problems are introduced by crossing the range bins, ideally one can avoid it by increasing the range bin width. This means sacrificing range resolution for the azimuthal resolution in the case of separable processing. It is not true, though, that the range curvature limits the width of coherent azimuth processing available. In fact, in the range curvature situation one can do some limited compensation by the techniques described in [7-5,7-6] or even full compensation by resorting to a non-separable model for the imaging system [7-4] and relying on singular value decomposition (SVD) techniques. However, all of our experiments in the following chapter assume separable processing for ease of computation and implementation.

7.4.2 Range alignment

In addition to the range curvature, there is another problem which hinders the separability of the processing: range misalignment. As described before, azimuthal processing must operate upon the returns from target points at equal range. Thus precise timing or other schemes on returns of individual pulses to insure correct range bin alignment is of ultimate importance to a single azimuth processing.

In obtaining the data from our radar system, range tracking is provided by a Poly/Kalman estimator which tries to lock the first strong peak of each pulse return onto a specific range bin. For example, if the target point closest to the radar is the wing tip, then the wing tip returns of different pulses hopefully will be locked in the same range bins. Because of scintillation of the reflectivities, this range locking method is not always reliable and misalignment occurs from time to time. Two automatic algorithms are proposed to realign the data, one being in the frequency domain and the other in the spatial domain.

7.4.2.1 spatial domain re-alignment

Let $f_{t_1}(r)$ and $f_{t_2}(r)$ be the high range resolution (HRR) returns (or our source data) from adjacent pulses where $t_2-t_1 = \Delta t$ is the pulse repetition interval (PRI) and r is the recorded range. Because of the tiny aspect angle change in one PRI, if we consider only the magnitude of the returns, then

$$m_{t_1}(r+\Delta r) \approx m_{t_2}(r), \quad \text{where } m_{t_i}(r) \triangleq |f_{t_i}(r)| \qquad (7\text{-}18)$$

for some Δr, the amount of misalignment which we would like to estimate. Define a correlation function between the two waveforms $m_{t_1}(r)$ and $m_{t_2}(r)$:

$$R(s) \triangleq \frac{\int_{-\infty}^{\infty} m_{t_1}(r)m_{t_2}(r-s)dr}{\left[\int_{-\infty}^{\infty} m_{t_1}^2(r)dr \int_{-\infty}^{\infty} m_{t_2}^2(r)dr\right]^{\frac{1}{2}}} \qquad (7\text{-}19)$$

Then because $m_{t_1}(r+\Delta r) \cong m_{t_2}(r)$, from the Schwartz inequality we have that R(s) will be maximal at $s = \Delta r$ and the amount of misalignment can be determined by a subsequent peak detection on R(s). It is observed that the denominator of Eq. (7-19) is independent of R(s) and can be dropped without affecting the peak location. Thus we could as well use

$$R'(s) \triangleq \int_{-\infty}^{\infty} m_{t_1}(r) m_{t_2}(r-s)dr \qquad (7\text{-}20)$$

which is a straight convolution relation.

7.4.2.2 frequency domain re-alignment

There are three differences between $f_{t_1}(r)$ and $f_{t_2}(r)$, the returns from adjacent pulses. One is that the range bins have been shifted relatively. The other two are an overall constant phase change due to the motion of the target center and a phase variation due to the effective rotation of the target. The last phase variation can be negligible if the sampling rate in azimuth direction (i.e., the PRF) is large enough. In that case

$$f_{t_1}(r) \cong \phi(t_1,t_2) f_{t_2}(r-\Delta r) \qquad (7\text{-}21)$$

where $\phi(t_1,t_2)$ is a phase factor independent of r and again Δr is the quantity to be estimated.

If one takes Fourier transforms of both sides of Eq. (7-21) with respect to r, then

$$\mathcal{F}_{t_1}(f) = \phi(t_1,t_2)\mathcal{F}_{t_2}(f)\exp(-j2\pi f\cdot\Delta r) \tag{7-22}$$

Let $\phi_{t_1}(f)$ and $\phi_{t_2}(f)$ be the phase part of $\mathcal{F}_{t_1}(f)$ and $\mathcal{F}_{t_2}(f)$, respectively, then

$$\Delta\phi_{t_1,t_2}(f) \triangleq \phi_{t_1}(f)-\phi_{t_2}(f) = \phi(t_1,t_2)\exp(-j2\pi f\Delta r) \tag{7-23}$$

and

$$\begin{aligned}\mathcal{F}^{-1}\{\Delta\phi_{t_1,t_2}(f)\} &= \mathcal{F}^{-1}\{\phi(t_1,t_2)\exp(-j2\pi f\Delta r)\}\\ &= \phi(t_1,t_2)\delta(r-\Delta r)\end{aligned} \tag{7-24}$$

hence

$$|\mathcal{F}^{-1}\{\Delta o_{t_1,t_2}(f)\}| = \delta(r-\Delta r) \tag{7-25}$$

The above analysis suggests the following way to estimate Δr: Take the Fourier transform of each pulse return and keep only the phase part. Find the phase difference of adjacent signatures. Finally, take the inverse Fourier transform of that phase difference and keep only the magnitude part. The location of the peak along the final range direction gives the estimate of range bin shift required to realign the range bins.

Clearly, the above two re-alignment schemes are equivalent in the noise-free situation. Under noisy condition, they would have different performances. However, a detailed analysis is not attempted in this work.

7.5 Motion Compensation

As described in Section 7.2, there are two components of the target motion: the motion of the target center relative to the radar and that of different target points relative to the target center as viewed from the radar. Only the latter contributes to the imaging ability of the radar, and the relation between the latter phase variation and the target reflectivity is a simple Fourier transformation in the azimuth direction. Thus, a motion compensation $[H_2]^{-1}$ which removes the effect of the motion of the target center is highly desirable as a preprocessing. Equivalently this is to find the trajectory of the target center and remove its effect from the raw data.

Two schemes of such a motion compensation are proposed for our imaging.

First scheme: The flight path of the target center can be inferred from the timing of the pulse returns. For example, in the first interval after the flight path has been decided to be a straight line and the azimuth angle determined, the result of the analysis in Section 7.2 can be applied to determine the coefficients of the quadratic and other higher-order phases and remove the χ_r effects to leave only the phases associated with χ_a which is relevant to imaging.

Second scheme: Since the trajectory of a single target point is very close to that of the target center, the returns from that point, if available, can as well be used as a reference to compensate for the targer center motion. In fact, this is equivalent to considering this target point as the rotation center of the target. The phases of this reference point as a function of azimuthal signatures can then be subtracted from those of all range bins at the corresponding signatures. Care should be exercised to assure two things in this process: first, the size of the reference point must be small enough. This is because the size of the reference point decides the best possible azimuthal resolution. Second, for each signature, the reference range bin must correspond to the reference point. This requires range alignment as described before. In addition, reference point must be rigid on the target.

There are situations where other forms of motion compensation should or could be applied: For example, in many cases mathematical simplicity of the imaging equation can be guaranteed only if the relative motion between the radar and the target is very simple. In the case where the flight speed, for example, is varying due to the weather or maneuvering an interpolation of the azimuthal data can be applied to obtain equally spaced samples. Alternatively, a varying PRF which follows the speed of the flight can be an effective tool in assuring a simple imaging equation. On the other hand, some times even if the flight speed is a constant, the interpolation or varying PRF schemes may still be needed. For example, in the first interval portion in

Section 7.2, $\frac{d\theta}{dt}$ in Eq. (7-9) is not a constant due to the ratio of η_r/R_o, and thus the Fourier transform relation would not be exact if there were no compensation.

7.6 Oversampling and Presumming

Usually the radar imaging system is oversampled in the azimuth direction because of a too high PRF. The purpose of presumming is to remove the oversampling redundancy. In the case of terrain imaging, over-sampling could be a result of not processing the whole antenna illumination pattern along the azimuth direction. In that case, the azimuth pattern width utilized or coherently processed determines the resolution of the image which in turn determines the amount of data redundancy. In our aircraft imaging, the situation is subtly different. Here the azimuthal width of the aircraft is so small that we always try to make full use of the maximum width of the effective radar illumination pattern, which is the azimuthal length of the aircraft itself. Under this condition the PRF required is decided by the azimuth dimension on the aircraft and the azimuth resolution again by the interval coherently processed. Thus, assuming other parameters fixed, a larger aircraft would require a higher minimum PRF to insure that no aliasing would occur in the final images. Also, since the effective antenna illumination (i.e., the overall aircraft azimuthal length) is independent of the wavelength, λ, the minimum PRF or the resolution in the aircraft-imaging case would be function of λ. This is in contrast to the ground terrain imaging cases where the full antenna illumination pattern width, which is proportional to λ, is to be used so that the resultant resolution is independent of λ because of a cancelling effect [7-1,2].

Let f_o be the carrier frequency and L the length of the aircraft along the direction normal to the LOS and on the imaging plane, as shown in Fig. 7-7. Let $\Delta\theta$ be the orientation change of the target between two adjacent pulses as observed from the radar, then the azimuthal frequency change will be

$$\Delta f_z \cong f_o \Delta\theta \tag{7-26}$$

This means a sampling interval of Δf_z in the azimuthal frequency domain, which implies a non-ambiguous azimuthal time interval of $\frac{1}{\Delta f_z}$, or spatial interval of $\frac{c}{2\Delta f_z}$, in accordance with the sampling theorem.

The oversampling factor o can be determined by

$$o = \frac{c}{2\Delta f_z}/L \tag{7-27}$$

To remove the oversampling and leave minimum useful data, a coherent low pass filter followed by sampling at a correspondingly low rate should be applied along the azimuth following motion compensation. The effect of low-pass filtering is to remove the high frequency noise which other-

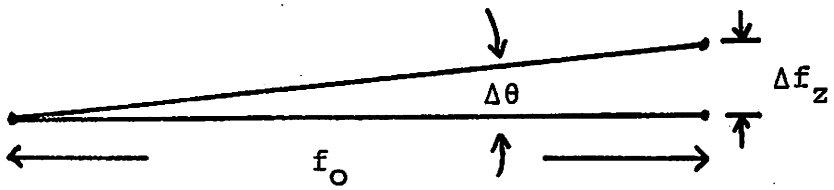

$$o = \frac{c}{2\Delta f_z} / L$$

L: azimuth length of target

Fig. 7-7. Determination of azimuth oversampling factor wise would appear in the resultant image.

7.7 Conclusions

In this chapter a radar imaging system more practical than the previous RAT-SCAT is researched. Although the baseline coherent processing principle, i.e., Fourier transforms along azimuthal direction, is the same as that in RAT SCAT, the data has to undergo much more processing before a final image can be realized. Motion compensation, range realignment, and presuming are additional requirements compared to the RAT SCAT case. The study of RAT SCAT, which is in a well-controlled environment is of much help to the analysis and processing in this and the following chapters.

Chapter 8

EXPERIMENTAL RESULTS OF RADAR IMAGING WITH TARGET MOTION

8.1 Introduction

Unlike the RAT-SCAT case, the in-flight data represents complicated flying geometries and requires much more analysis and processing to reach final radar images. A series of processing techniques developed from the previous chapter will be presented along with their experimental results.

The mode in which the radar operated and our source data was acquired was a wide band high resolution mode. The transmitted pulses were linear FM signals whose returns were then compressed using matched filtering techniques in the radar receiver and aligned side by side by using a Poly/Kalman centroid estimator.

8.2 Experimental Results - First Interval

A condensed overall view of magnitude part of first interval data is shown in Fig. 8-1 in which each row corresponds to the log magnitude of the compressed return of a single pulse. Only every 16th signature is shown in this figure. Recalling that this interval represents the radar returns when the target aircraft was flying toward a broadside position (Fig. 7-1), we presume that the first high-intensity range bin corresponds to the left wing tip and the next distinct strong returns are from the fuselage and nose. Note that the radar is to the left.

Then it can be perceived from Fig. 8-1 that the fuselage is at a greater and greater range distance away from the wing tip along the signatures as a result of closing-to-broadside during flight. Also observe that while most portions of Fig. 8-1 seem pretty well range-aligned, other portions do need re-alignment before a separable processing can be implemented.

To present the data in detail all of the first 512 signatures are displayed in Fig. 8-2. The phase image (Fig. 8-2(b)) indicates clearly that the target points probably lie in range bin number 50 to 200, where a strong structure of phase relationships appears as a result of the coherent radar pulsing. This is also shown in the log magnitude picture Fig.8-2a, although with less clarity. There is a transient region where the strength of the returns decreases gradually with the range or time. This is conjectured to be a result of multiple reflections on the target which take more than before re-radiating to the radar receiver.

To investigate further the behavior of the returns, we kept only the regions of strong signal returns and a sequence of 80 second data or 8192 signatures is shown in

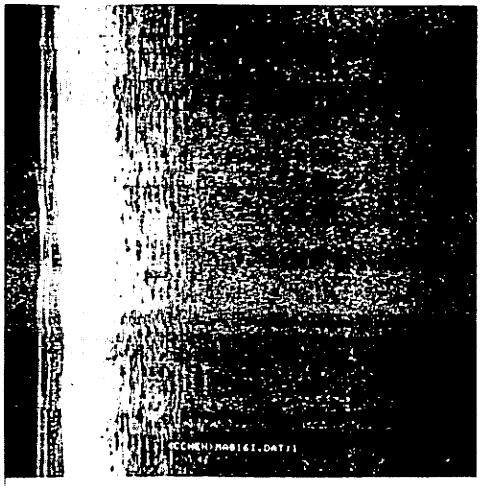

Fig. 8-1. Overall view of data in first interval; log magnitude of every 16th pulse return

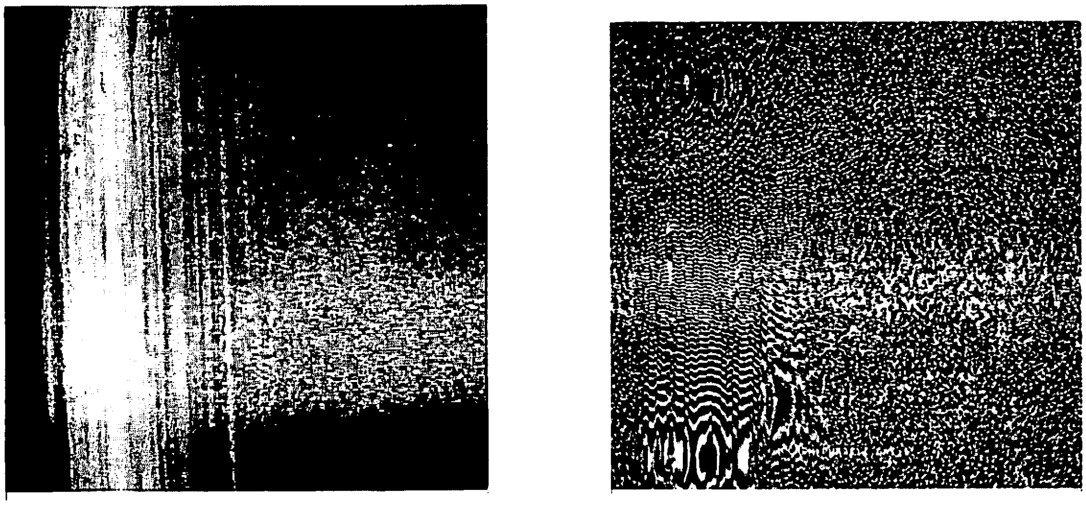

a) Log magnitude

b) Phase

Fig. 8-2. First 512 signatures in first interval

Fig. 8-3 with both log magnitude and corresponding phase. Observe the quadratic-like phases along the flight direction due to the flight geometry, as analyzed in Section 7.2.

Since the radar receiver has range compressed the signal returns, ideally we will only need to perform some azimuthal processing. For convenience we transpose the data so that the horizontal direction now denotes the signature or along-flight direction. Figure 8-4 shows the log magnitude and phase of typical signatures (signature 8001 to 8512). To remove the quadratic phases from Fig. 8-4(b), three options exist, the first two being similar. They are described in subsections 8.2.1-3:

8.2.1 Linear fitting the phase differences and subsequent integration

Since the differentiation of quadratic phases is linear phases, a linear fit to the phase differences can be applied to determine the quadratic phase curvature. Figure 8-5(a) shows the azimuthal phase difference of Fig. 8-4(b). Note that except for the phase wrap-around in the right half portion and the small variation due to oversampling and noise, the intensity used to linearly encode the phase between $-\pi$ to π looks quite linear. However, before a successful linear fit can be obtained, the phase-wrap problem has to be solved and this is usually not a very easy task. In fact, it is because of the rapid phase

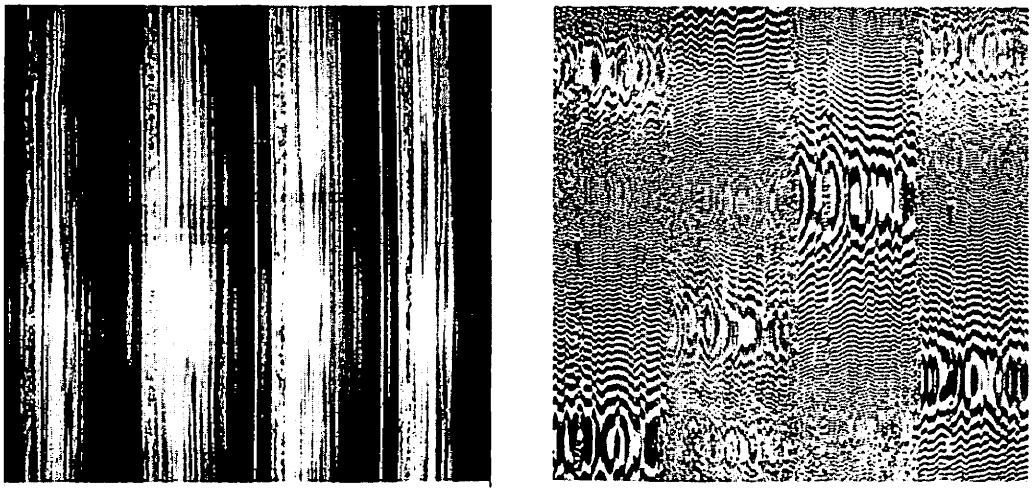

a) Log magnitude b) Phase

signature number 1-2048

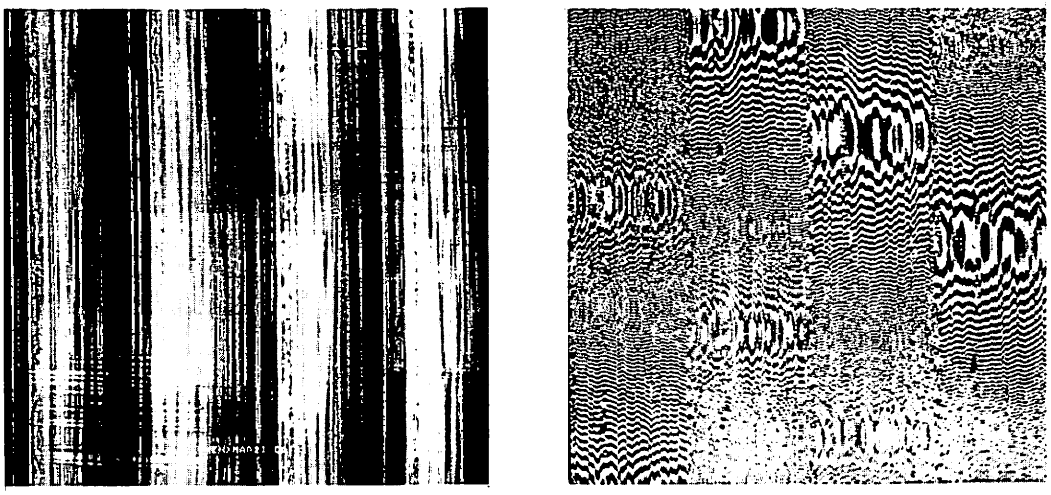

c) Log magnitude d) Phase

signature number 2049-4096

Fig. 8-3. Data in first interval with 128 range bins stacked side by side

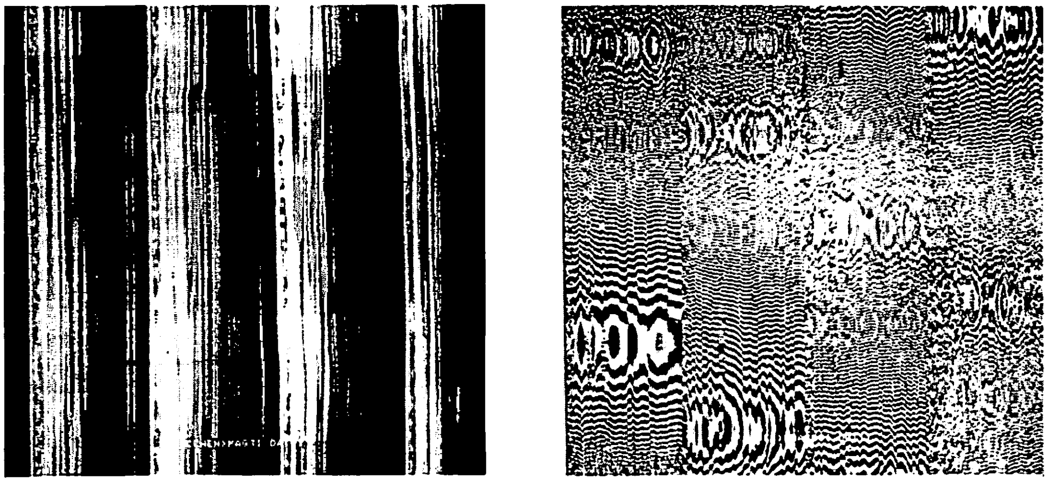

e) Log magnitude f) Phase

signature number 4097-6144

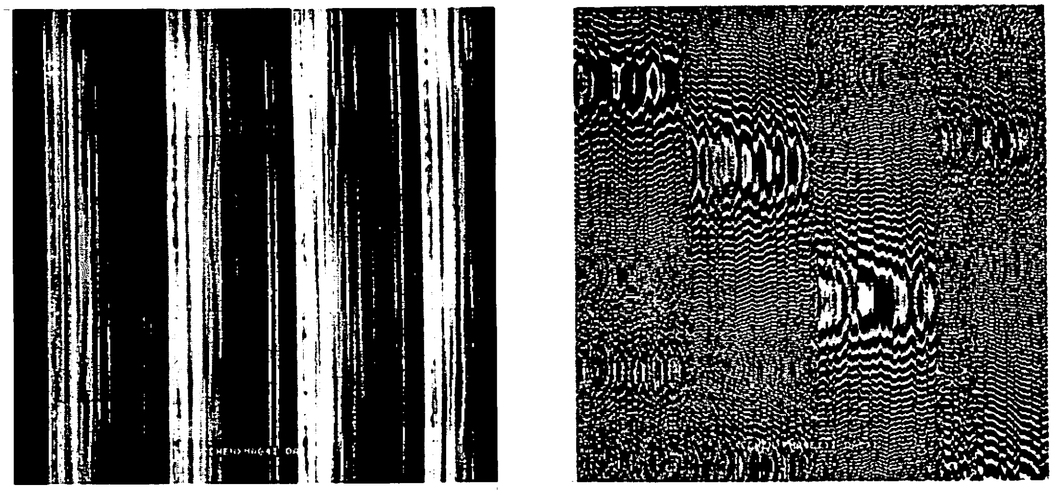

g) Log magnitude g) Phase

signature number 6145-8192

Fig. 8-3. (Continued)

modulus phenomena in Fig. 8-4(b) that causes direct unwrapping Fig. 8-4(b) extremely difficult. We used a simple-minded scheme to unwrap the phase differences of Fig. 8-5(a) to get Fig. 8-5(b), from which the linear portion of phase variation was estimated and removed to leave Fig. 8-5(c). Since Fig. 8-5(c) is still in the differentiation domain, an integration brings it back to the azimuthal phase domain, as depicted in Fig. 8-5(d).

8.2.2 Linear fitting the phase difference and quadratic subtraction

An alternative to applying the estimated linear-phase-difference is to subtract the estimated quadratic phase (from integration of estimated linear phase difference) from Fig. 8-4(b) directly. The result is shown in Fig. 8-5(e).

Magnitudes of azimuthal Fourier transforms of Fig. 8-5(d) and 8-5(e) are shown in Figs. 8-6(a) and 8-6(b), which are very similar visually.

8.2.3 Target point referencing

The above two schemes of removing phase variation due to target center motion are based on an assumption that the flight path is relatively straight during the coherence time. In other cases where the range trajectory is more complicated than a low-order polynomial curve, the above schemes are expected to be difficult. Another motion com-

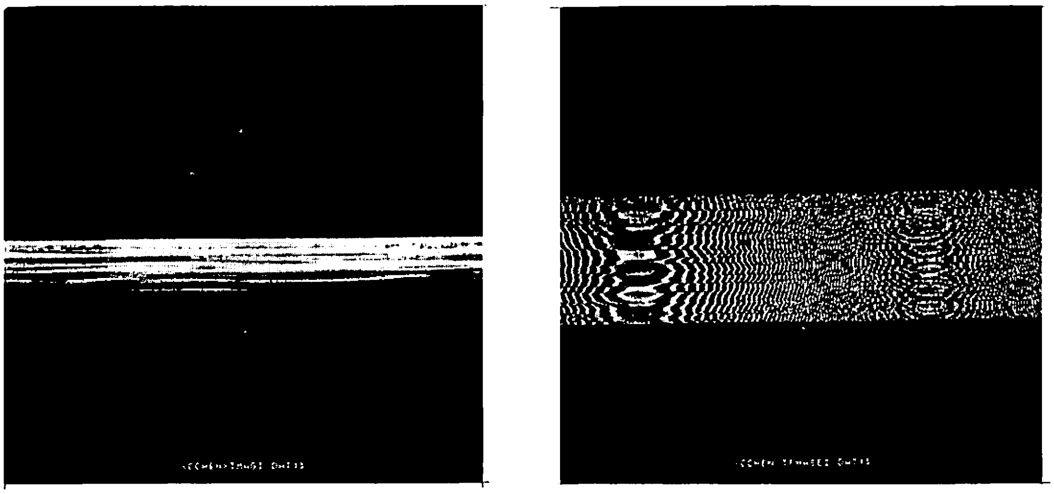

a) Log magnitude

b) Phase

Fig. 8-4. Signature number 8001-8512
(range direction is vertical)

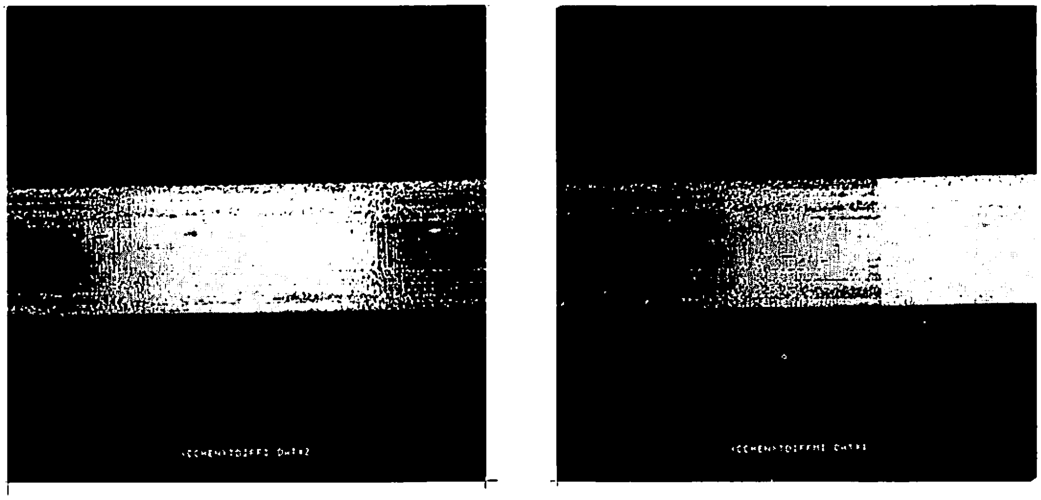

a) Phase difference of Fig. 4b)

b) Unwrapped version of a)

Fig. 8-5. Motion compensation on Fig. 8-4(b) using linear curve fitting

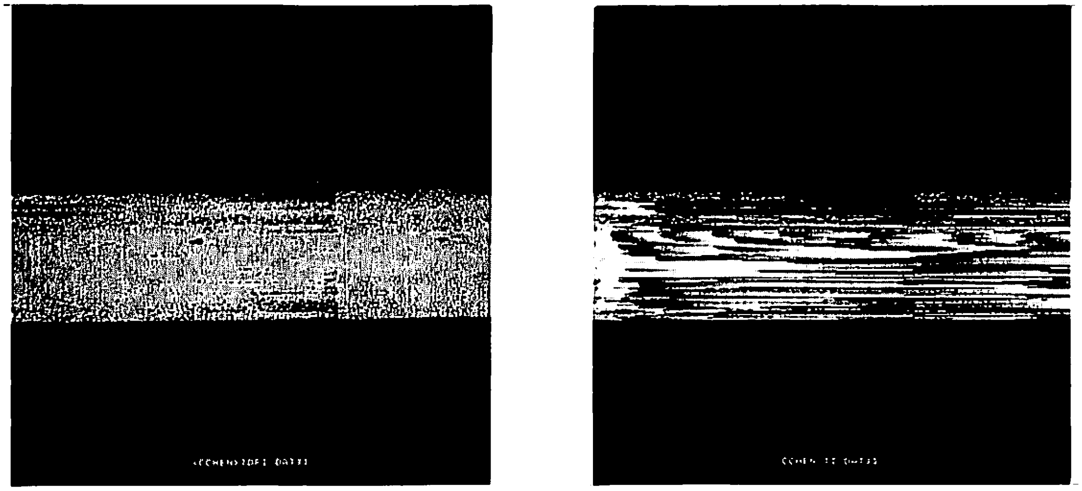

c) Linear phase removed from b)

d) Phase integration of c)

e) Quadratic phase removed directly from 4b)

Fig. 8-5. (Continued)

pensation scheme somewhat independent of the flight geometry and simple in implementation is to use the signal returns from a reference point to estimate the history of the flight range trajectory. This single point can be thought of as the center of rotation of the target and its phases subtracted from all other range bins to leave only the phase histories of all target points relative to this reference point. This was, in fact, the techniques used in subsequent imaging.

Since the azimuthal oversampling factor has been determined to be greater than 50, the data after quadratic phase compensation can be reduced by a factor of 32 before Fourier transformations are applied. The result is shown in Fig. 8-6(c). A comparison of Figs. 8-6(a) and 8-6(c) confirms the validity of the coherent presumming. Note that in Figs. 8-6(a), (b) and (c) the azimuthal bin width is much wider than the range bin width and a subsequent interpolation has to be done to properly scale the images.

Figure 8-7 is a series of processed aircraft images using the reference-point scheme. Consecutive pictures represent abutting 2048 signatures or 20-second flight time. The images have been linearly interpolated in azimuthal to give the same range and azimuthal bin width such that the images are properly scaled. Visually Fig. 8-7(d) is the best probably due to the best range alignment of the data in that time interval.

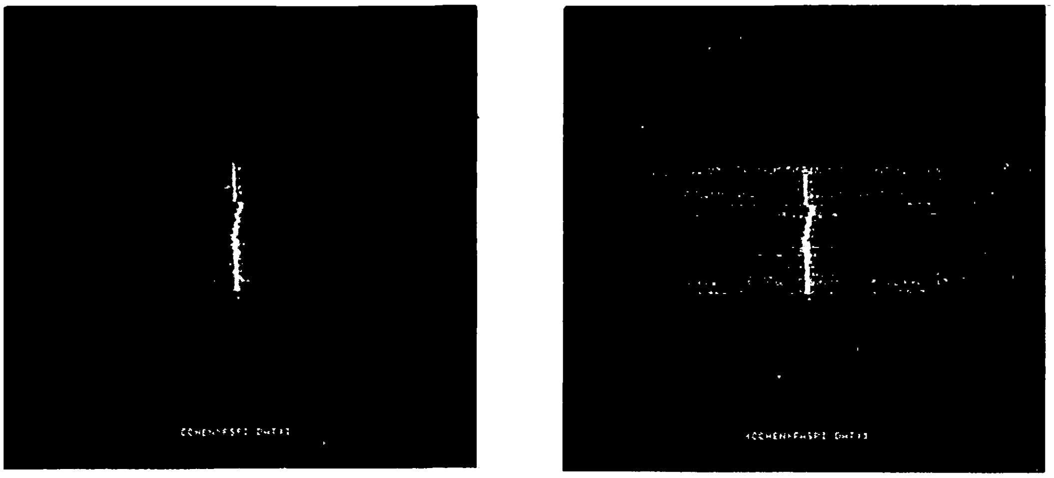

a) Magnitude of Fourier transform of 5d)

b) Magnitude of Fourier transform of 5e)

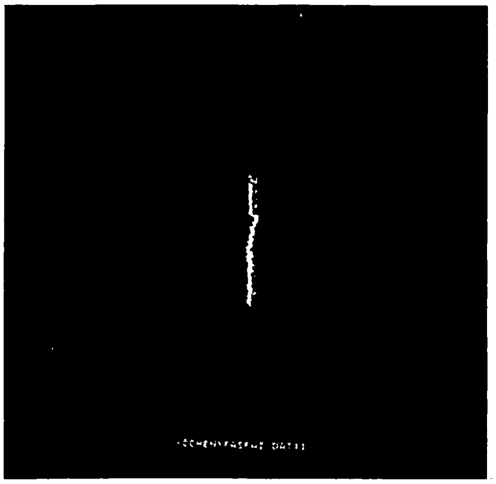

c) Fourier transform of collapsed version of 5e)

Fig. 8-6. Cross-range processing Fig. 8-5

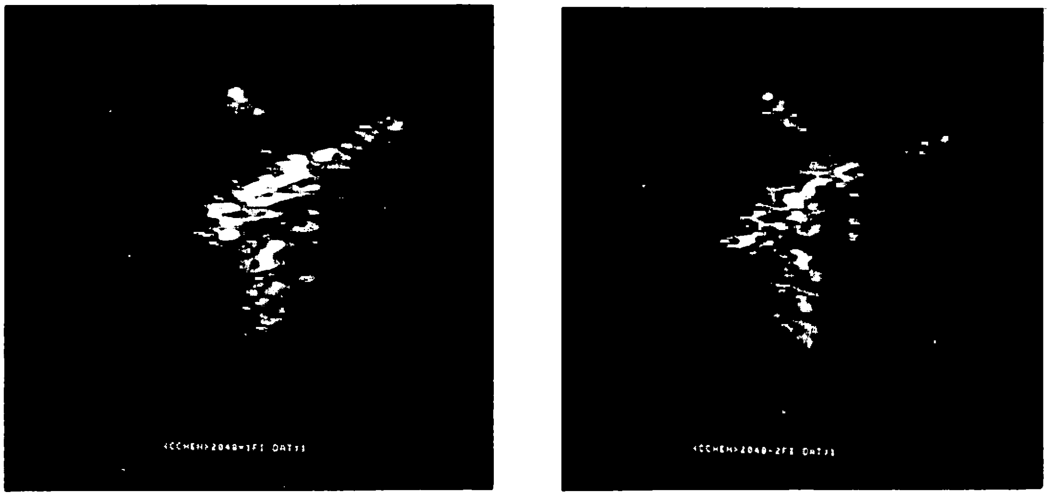

a) 1st 20 seconds or 2048 signatures ($\approx 2.5^{\circ}$ aspect change)

b) 2nd 20 seconds

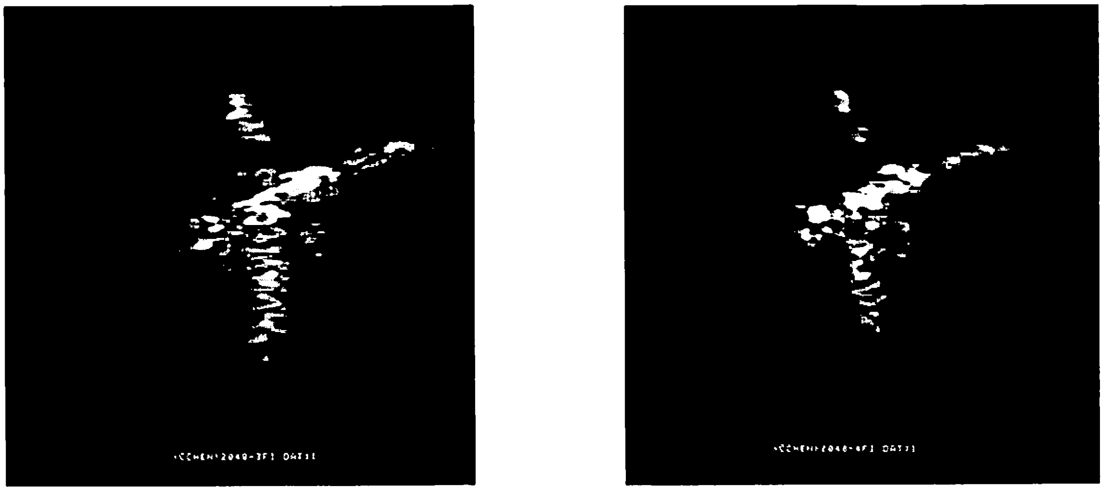

c) 3rd 20 seconds

d) 4th 20 seconds

Fig. 8-7. Aircraft radar images with abutting 20 second coherence times

Ideally, an increase in coherence time should be accompanied with an equally increased amount of resolution. This is not the case in Fig. 8-8, where coherence times of 40 and 80 seconds are processed. The conjecture is that the range curvature and range misalignment which tend to blur the images outplay the coherence time increase. As described in the previous chapter, one way to alleviate the range curvature problem is to use larger range bin widths. To test this, we used the same parameters as in Fig. 8-8(b) except the data in range dimension were reduced by a factor of two by a coherent collapsing. The result shown in Fig. 8-9 is to be compared with Fig. 8-8(b).

The phase variations of target points induced by the target motion is the key to the coherent radar imaging. As one can see from Fig. 8-2, the magnitude of the radar returns which provide only range information are very similar from pulse to pulse and represent a great deal of data redundancy. From the DOF point of view one would like to have approximately equal amount of input and output data. Since only the magnitude parts of the processed images are needed for displays, it is conjectured that the phase portion of data alone is sufficient to give an image of a comparable quality. This would achieve a factor 2:1 in data reduction. Experimental result shown in Fig. 8-10 seems to support this conjecture. Intuitively speaking, the range bins corresponding to no strongly

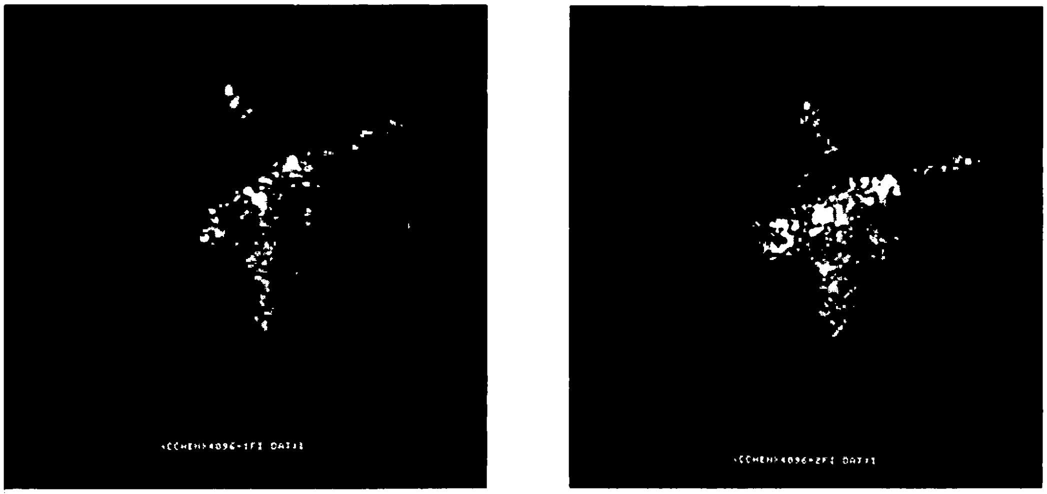

a) 1st 40 seconds
($\approx 5^{\circ}$ aspect change)

b) 2nd 40 seconds

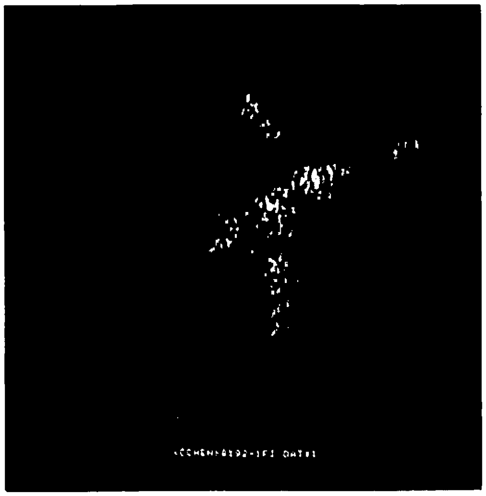

c) 1st 80 seconds
($\approx 10^{\circ}$)

Fig. 8-8. Aircraft images with different coherence times

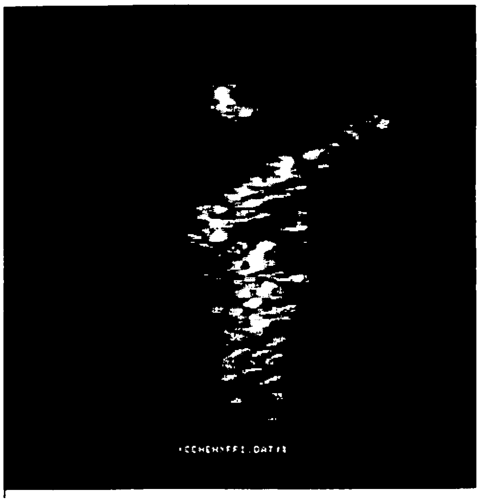

Fig. 8-9. 2:1 range collaped; coherence time = 40 seconds

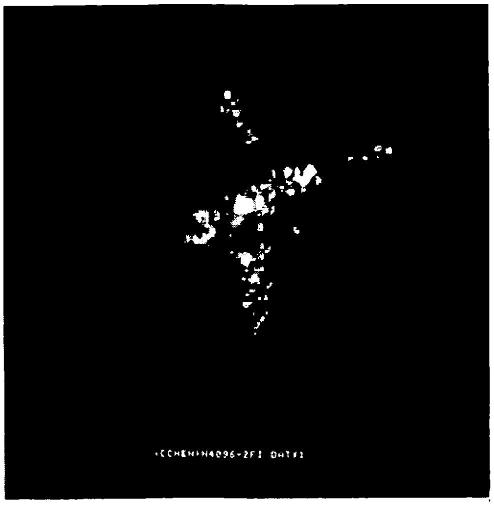

Fig. 8-10. Same portion as Fig. 8-7d); phase information only

reflective target points have a random-like phase and are likely to spread their energy over the spectrum after the Fourier transform in the azimuthal direction is taken. On the other hand, target points of strong reflectivities give highly correlated azimuthal radar returns, resulting in clusterings of energy corresponding to different azimuthal target points in the processed Fourier transform domain. In this way, the magnitude of the returns do not play an important role in determining in which range bins lie the strong target points.

8.3 Experimental Results - Second Interval

The first 8000 signatures of the second interval source data taken when the airplane was making a standard left turn are shown in Fig. 8-11 and Fig. 8-12. Unlike the straight flight of interval 1, the phase plot here has a changing azimuthal structure due to the turning motion of the target, which creates complicated range and Doppler histories. In addition, there are several occasions when the range bins are seriously out of alignment. The overall view of Fig. 8-11 shows the changes of relative positions of the nose, fuselage and wing tip due to the turn. A portion of data was taken when the airplane was approximately nosed into the radar and a series of resultant images are shown in Fig. 8-13 using the reference-point technique as a phase compensator. In this case the

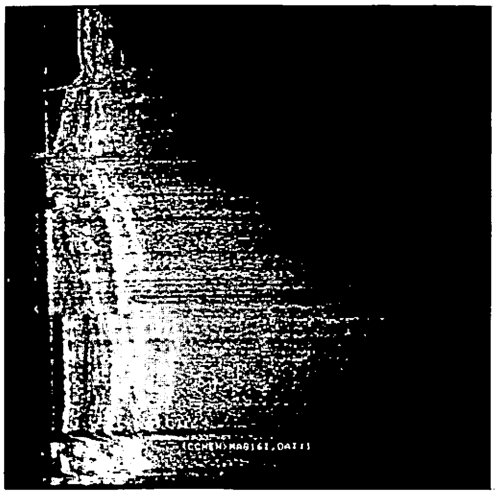

Fig. 8-11. Overall view of data in second interval; log magnitude of every 16th pulse return

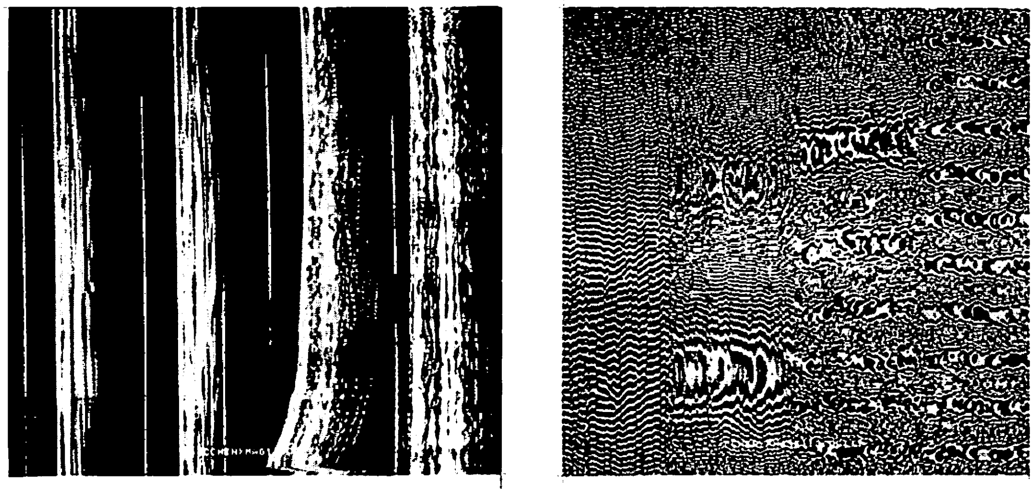

a) Log magnitude b) Phase

signature number 1-2048

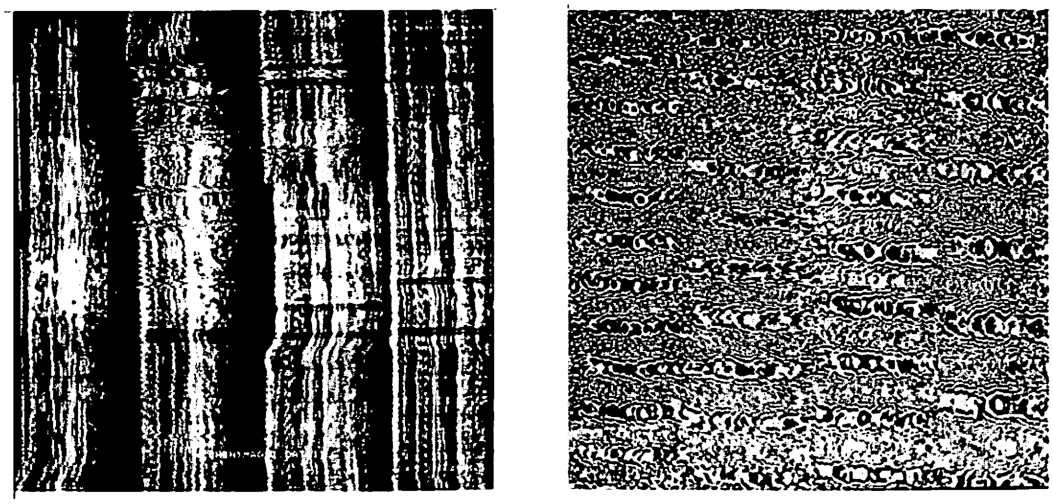

c) Log magnitude d) Phase

signature number 2049-4096

Fig. 8-12. Data in second interval with 128 range bins side by side

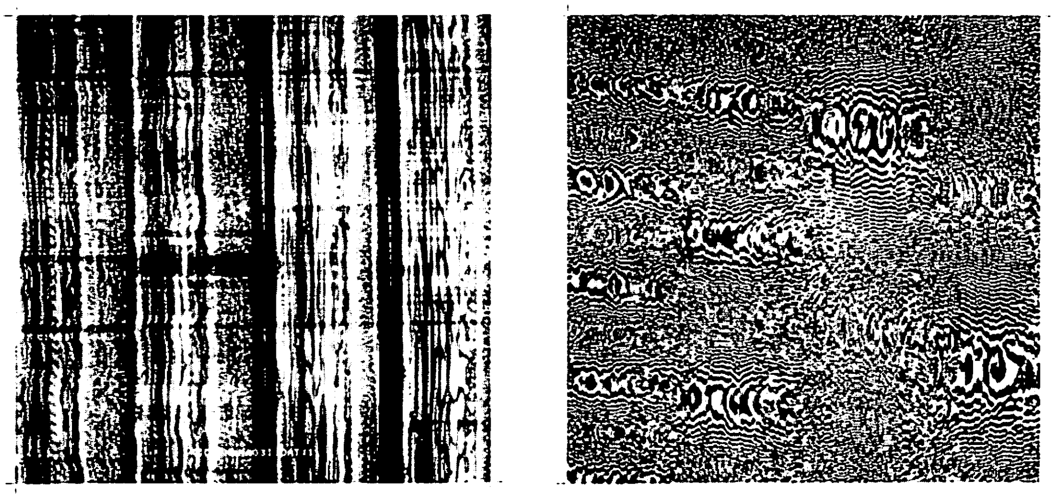

e) Log magnitude f) Phase

signature number 4097-6144

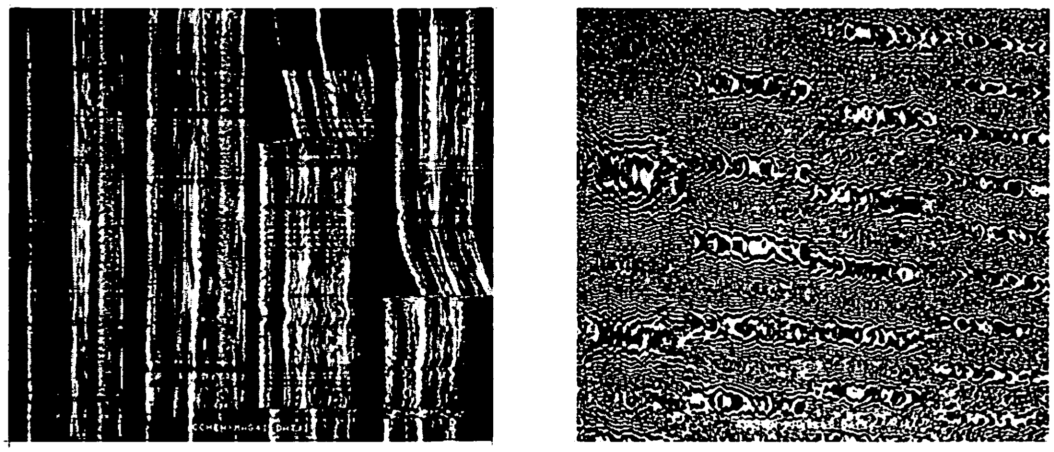

g) Log magnitude h) Phase

signature number 6145-8000

Fig. 8-12. (Continued)

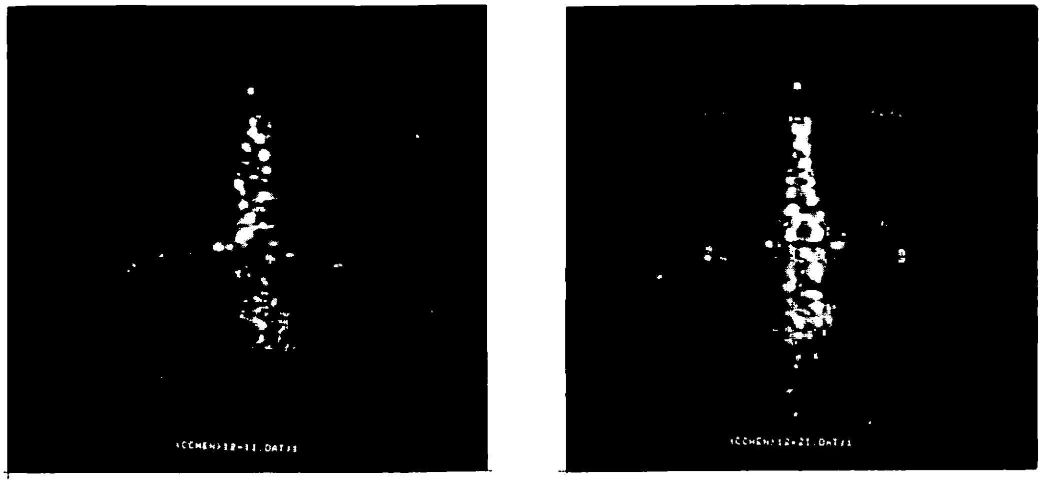

a) 1st 2.5 seconds or 256 signatures (≈ 4.5° aspect change)

b) 2nd 2.5 seconds

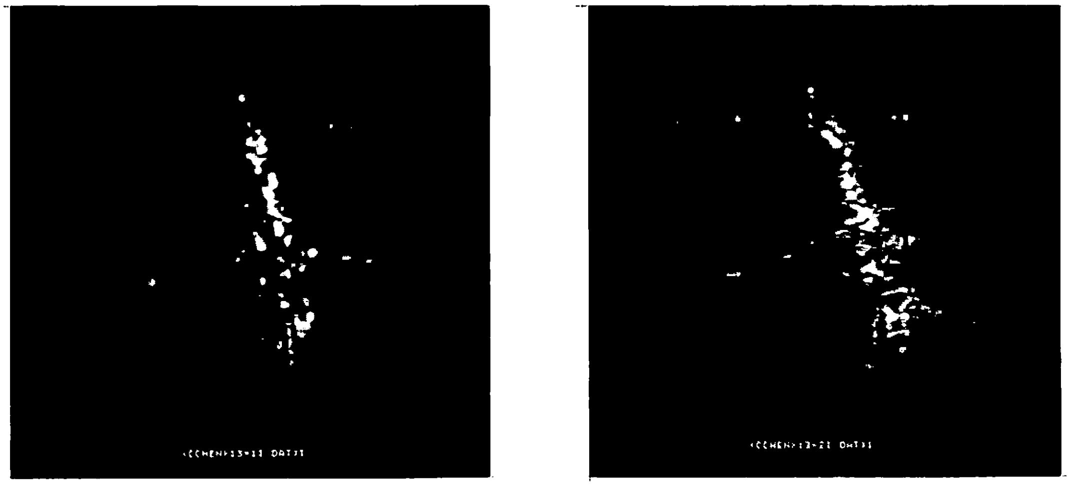

c) 3rd 2.5 seconds

d) 4th 2.5 seconds

Fig. 8-13. Aircraft radar images with abutting 2.5 second coherence times in second interval nose tip serves as a very good reference point as shown by the degree of sharpness of the nose in these images. Figure 8-14 shows images of different coherence times. In Fig. 8-14(b) the shape of the fuselage has been clearly imaged. A coherence interval of 18° rotation of the target seems too much to give a satisfactory image as a result of overwhelming range curvature.

The spread patterns close to the nose are due to the aircraft radar which was constantly scanning during the flight, presenting an object of changing reflectivity and violating the assumption that the target was a rigid body in the imaging system.

8.4 Range Re-alignment Results

As is evident from Figs. 8-11 and 8-12 the radar breaks range lock quite often during the turn of the target aircraft. This is to be expected as different scatterers from the aircraft dominate the leading return of the radar reflection. Naturally when the radar broke lock seriously, one would not expect to be able to image without re-alignment processing. Section 7.4 presented a theoretical discussion on such re-alignment procedures and this section will present some experimental results.

The realignment procedures presented in the last chapter are based on a sequential comparison between adjacent signatures. Because of the discrete nature of the

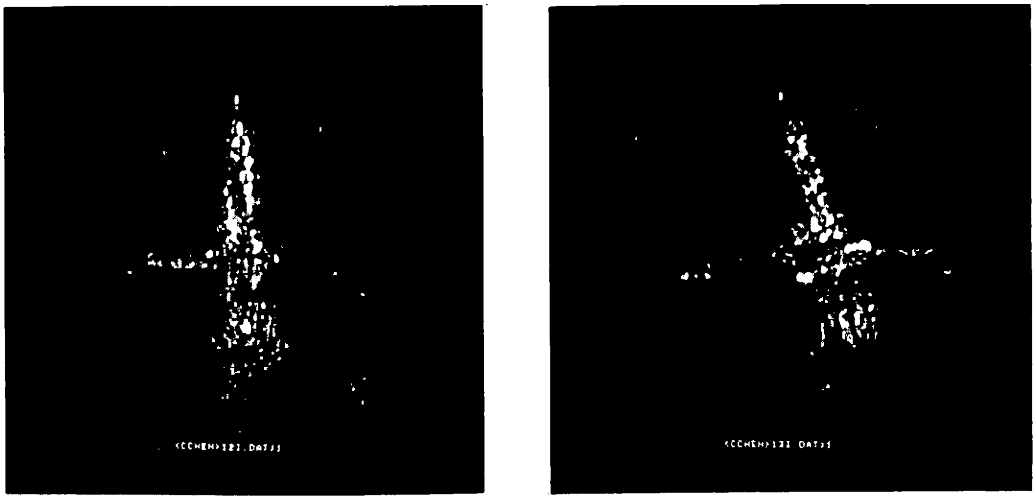

a) 1st 5 seconds
(≈ 90° aspect change)

b) 2nd 5 seconds

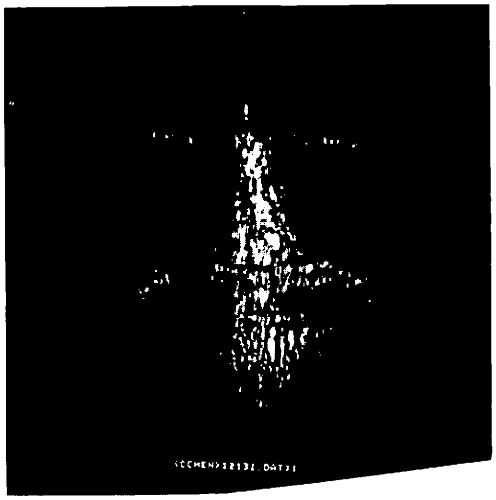

c) 1st 10 seconds
(≈ 18° aspect change)

Fig. 8-14. Aircraft images with different coherence times data, each comparison could produce a misalignment error by up to one pixel width. Hence, although the scheme is successful on local realignment, the accumulated errors from this primitive recursive procedure make a global alignment very difficult to produce satisfactorily corrected images.

A remedy to this is to compare each signature with a reference which has been aligned globally. However, this reference has to bear considerable similarity to the signature being compared to avoid large quantity error. From these requirements and considering the slowly varying nature of the successive signatures, we propose to use for reference an exponentially weighted sum of the magnitudes of previous realigned signatures. The algorithm is easily implementable by assigning a weight to the newly aligned signature and a complement weight to previous reference to form the current reference. The weight can be chosen according to how slowly the range profiles change along the signature assuming the profiles resemble a "Markov process." A small weight corresponds to high correlation of the process. On the other hand, a weight of 1 corresponds to very low correlation and coincides with the theoretical realignment scheme described in the last chapter.

We applied the modified realignment algorithm using exponential weighting for the signature magnitude correlation and obtained a series of realigned data as in Fig. 8-15. Sequential pictures contains 512 signatures or a flight time of 5 seconds each. Note that the first 16 pictures correspond to the original data in Fig. 8-12. A weight of 0.05 was used in all 21 data segments which comprise the whole second interval of the flight. Except for very few signatures the realignment algorithm seems to work very well.

The realigned data was processed during the same reconstruction procedure before and a series of 21 images produced as in Fig. 8-16 in which the effective rotation rate of the aircraft was assumed constant. Most of the aircraft images are recognizable and clearly show the turning. Fig. 8-16(a) and (b) correspond to the motion before completing the starting of the turn and are thus not square pictures. The nose and left wing tip crossed in and out respectively at the later portion of the data segment (e) as shown by Fig. 8-15(e) and by the change of Fig. 8-16(e) from Fig. 8-16(f). In Fig. 8-16(r) the image was a superposition of two images with the same orientation and with the wingtip of one image being on top of the nose of the other. This is due to the equi-distance of those two target points from the radar at that particular target orientation. In Figs. 8-16(t) and 8-16(u) the wingtip was chosen as the reference range bins for motion compensation whereby the range realignment procedure aligned the data

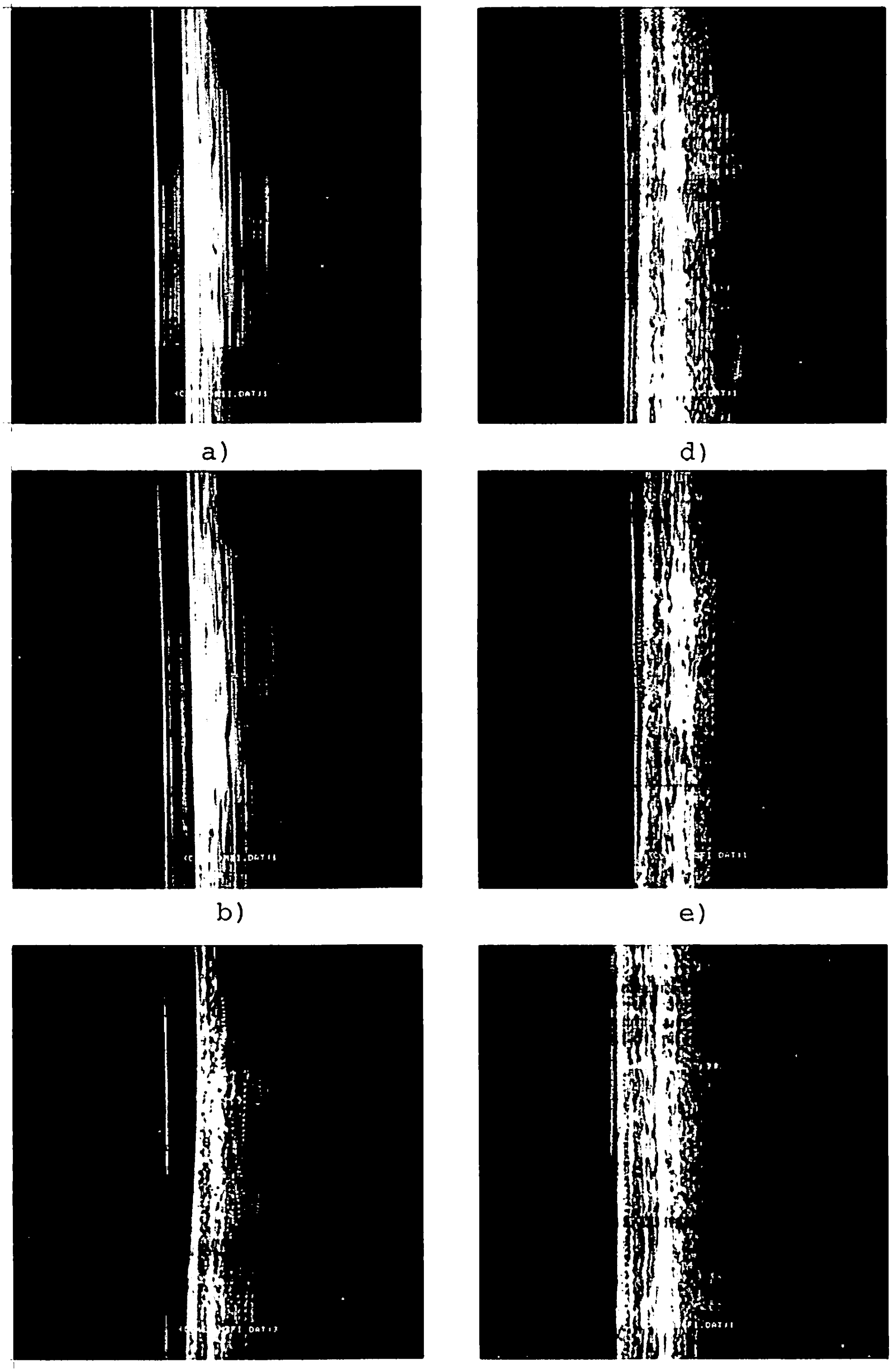

a) d)

b) e)

c) f)

Fig.8-15. Range-realigned signatures

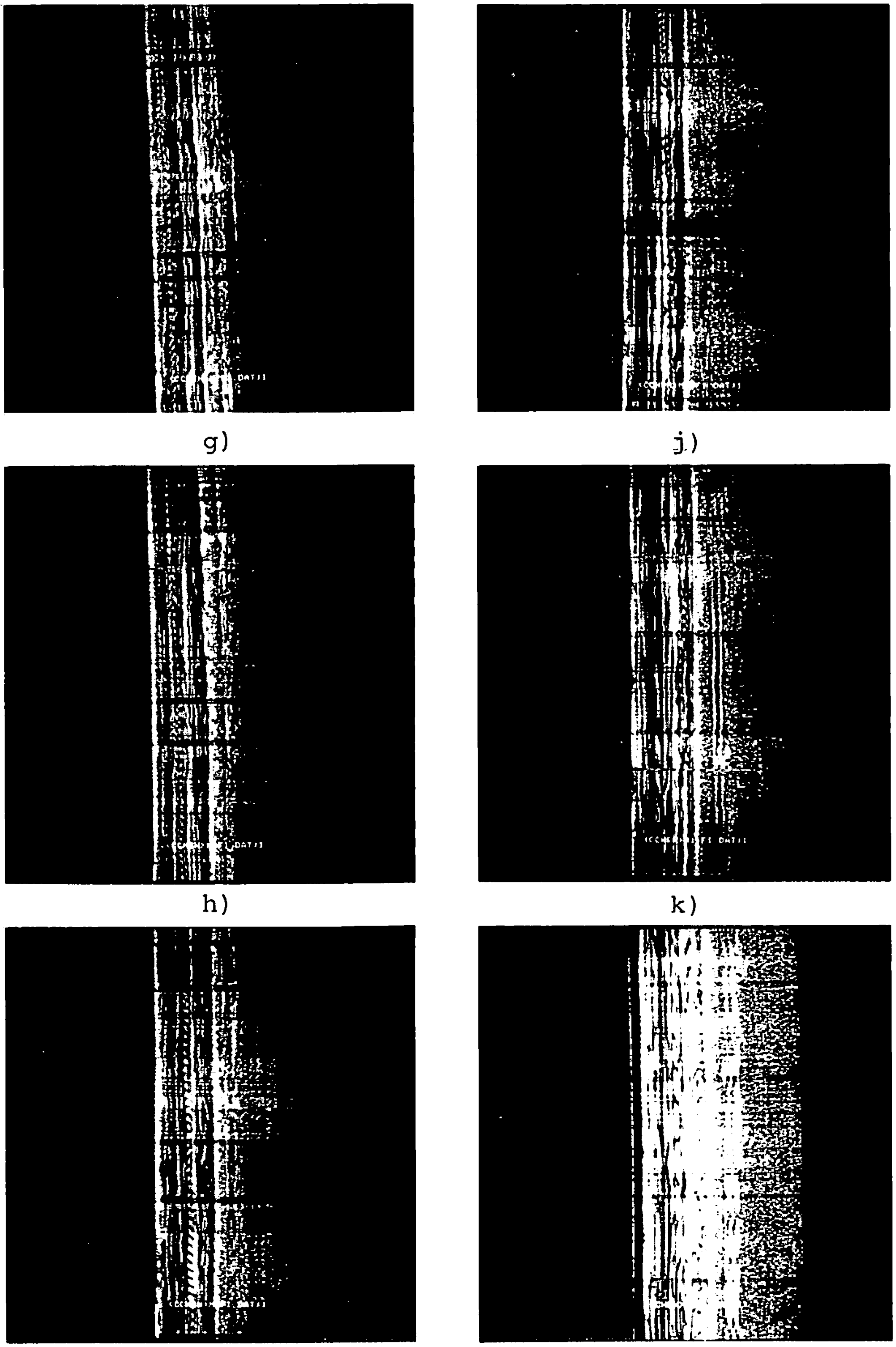

g) j)

h) k)

i) l)

Fig. 8-15. (Continued)

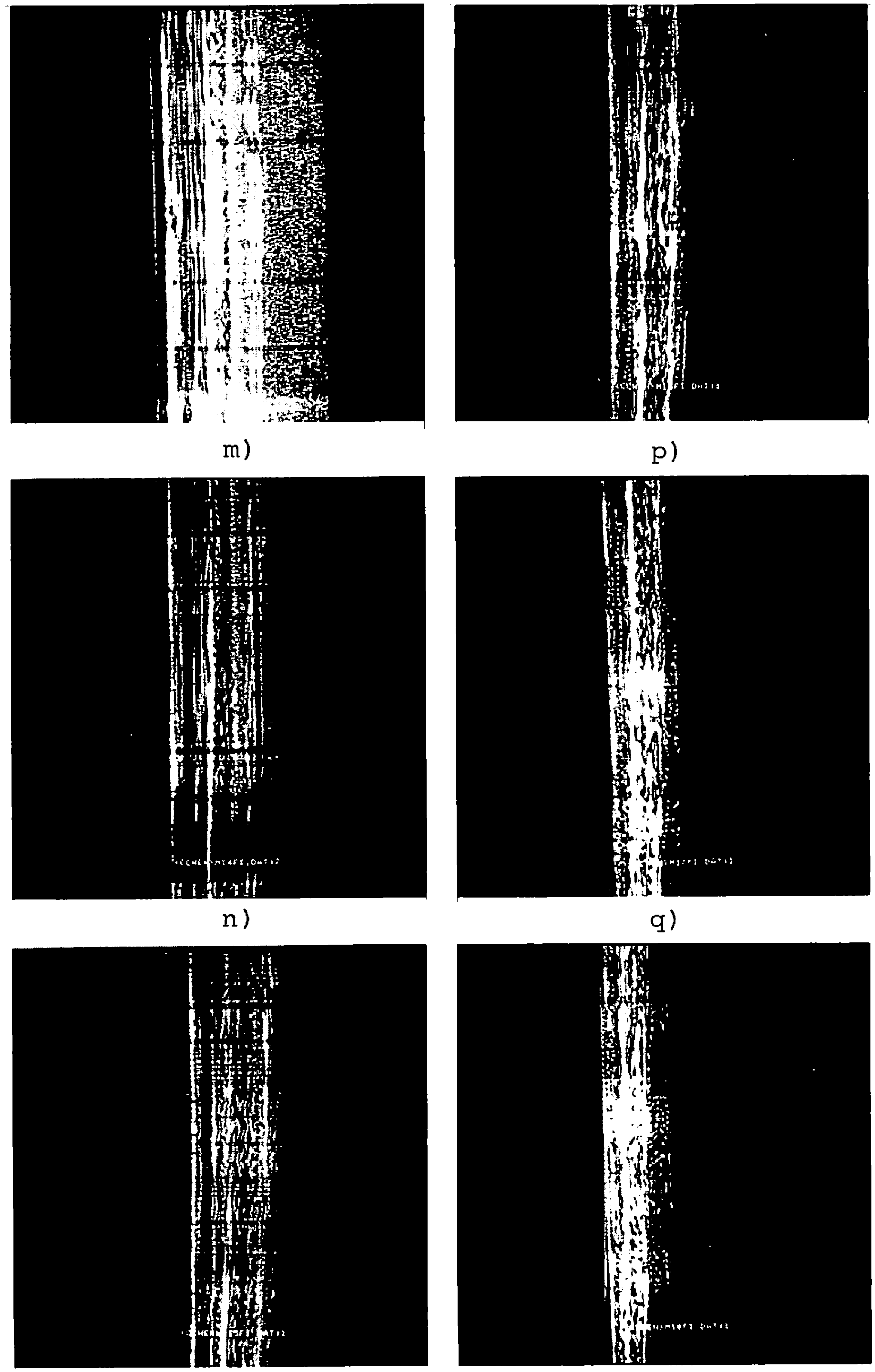

m) p) n) q) o) r)

Fig. 8-15. (Continued)

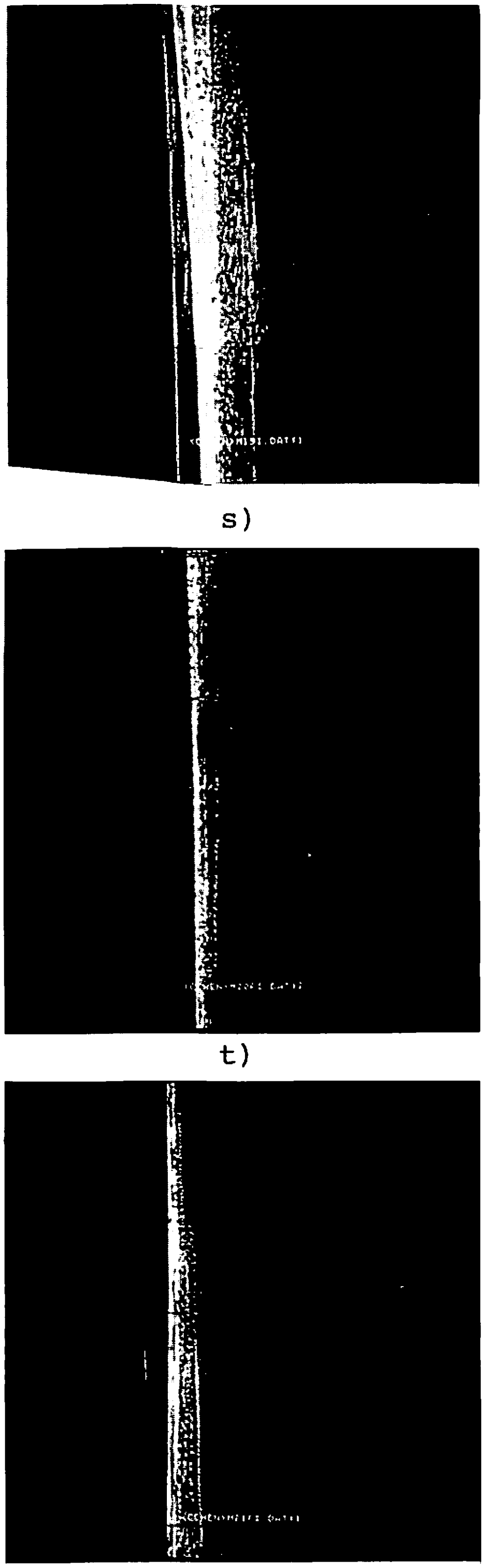

s)

t)

u)

Fig. 8-15. (Continued)

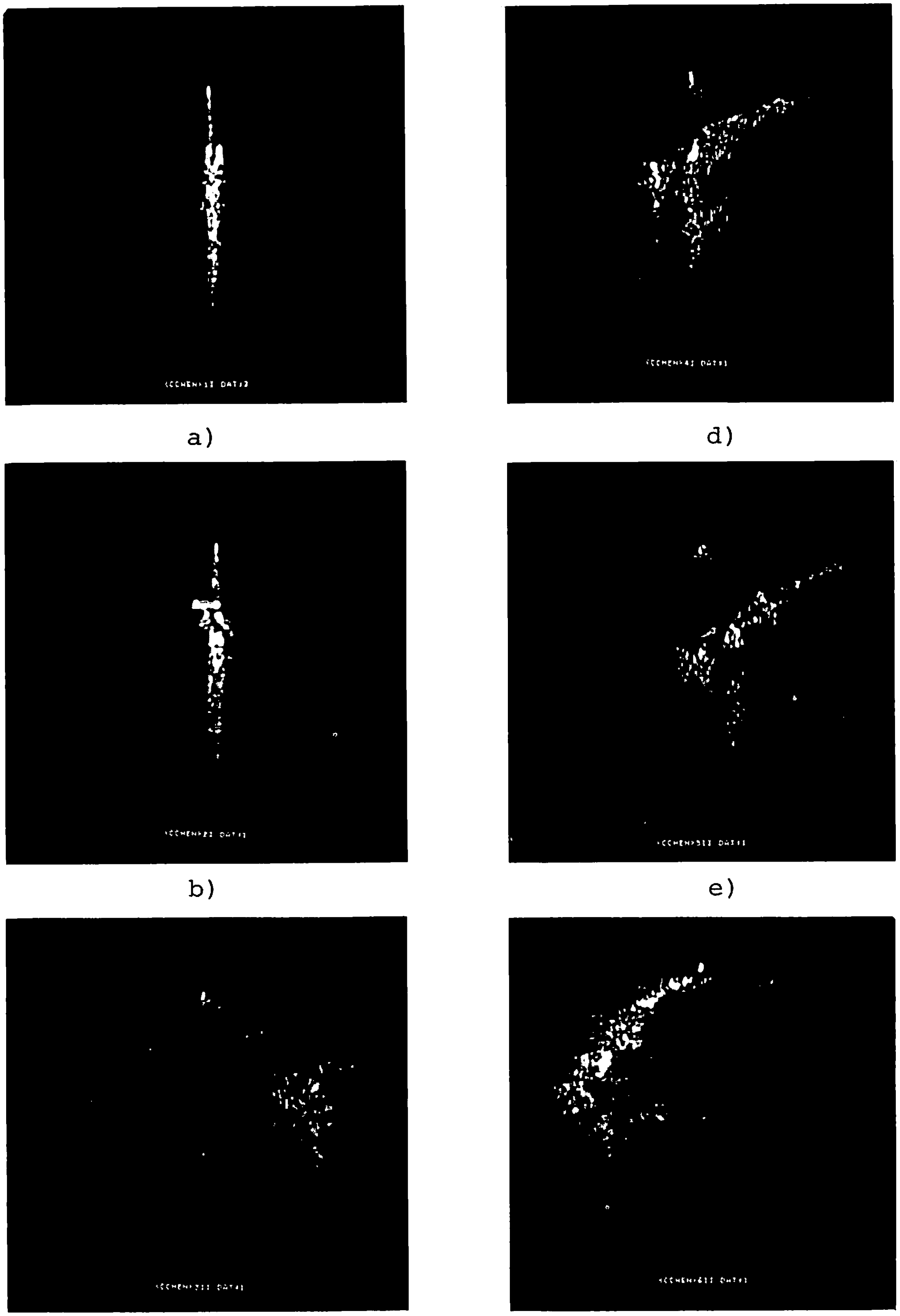

a) d)

b) e)

c) f)

Fig. 8-16. Aircraft images after range re-alignment

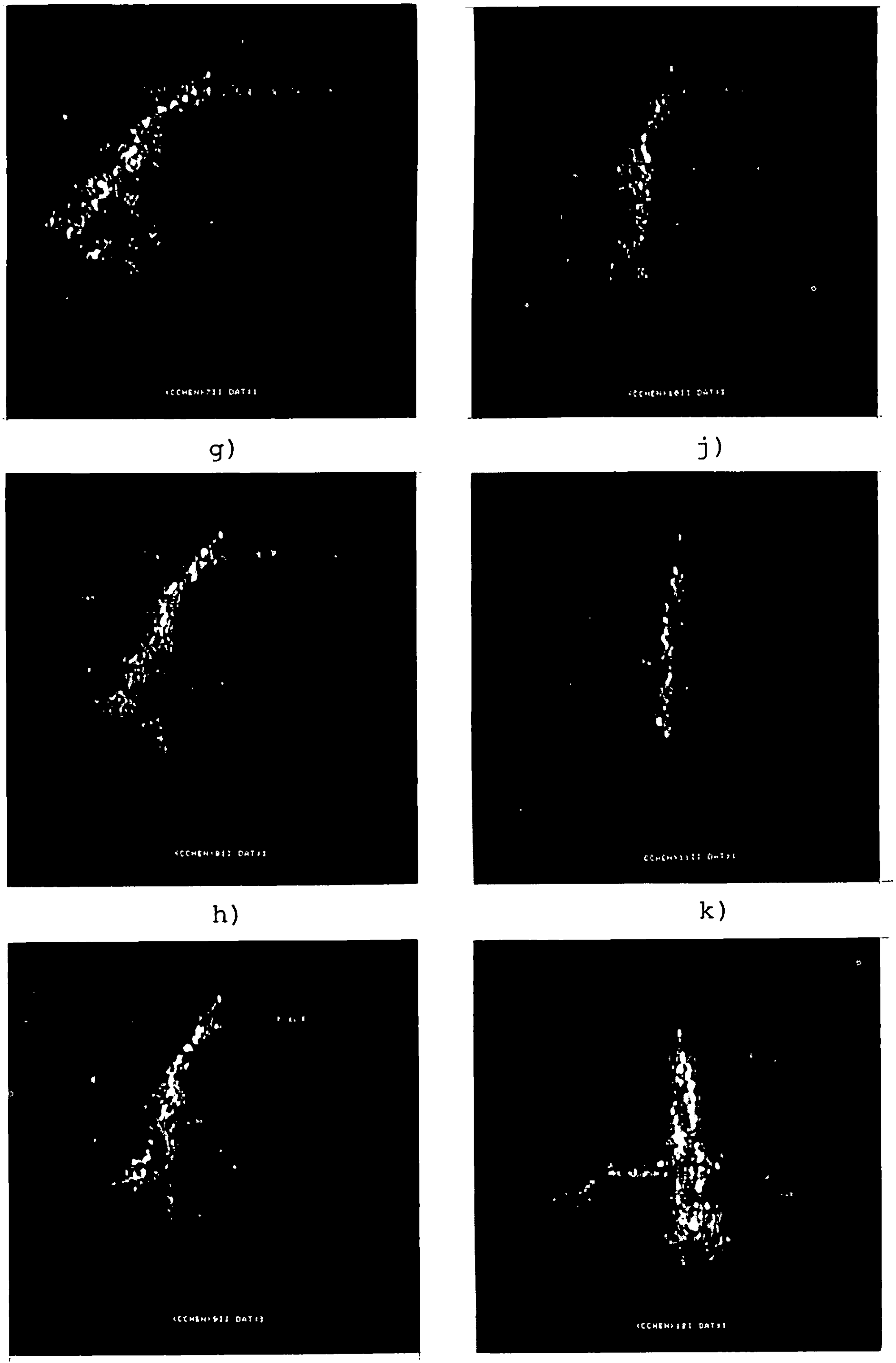

g) j)

h) k)

i) l)

Fig. 8-16. (Continued)

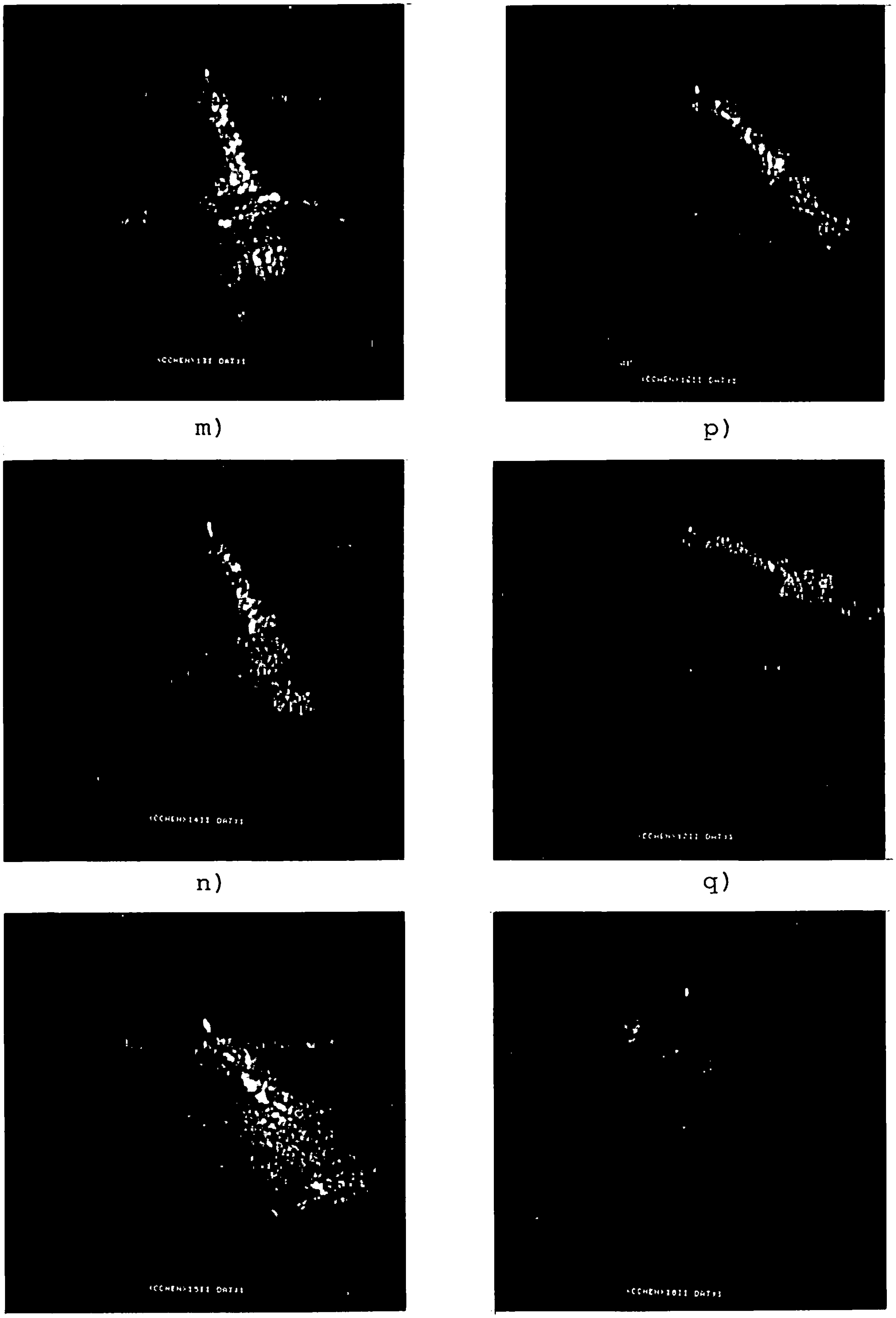

m) p)

n) q)

o) r)

Fig. 8-16. (Continued)

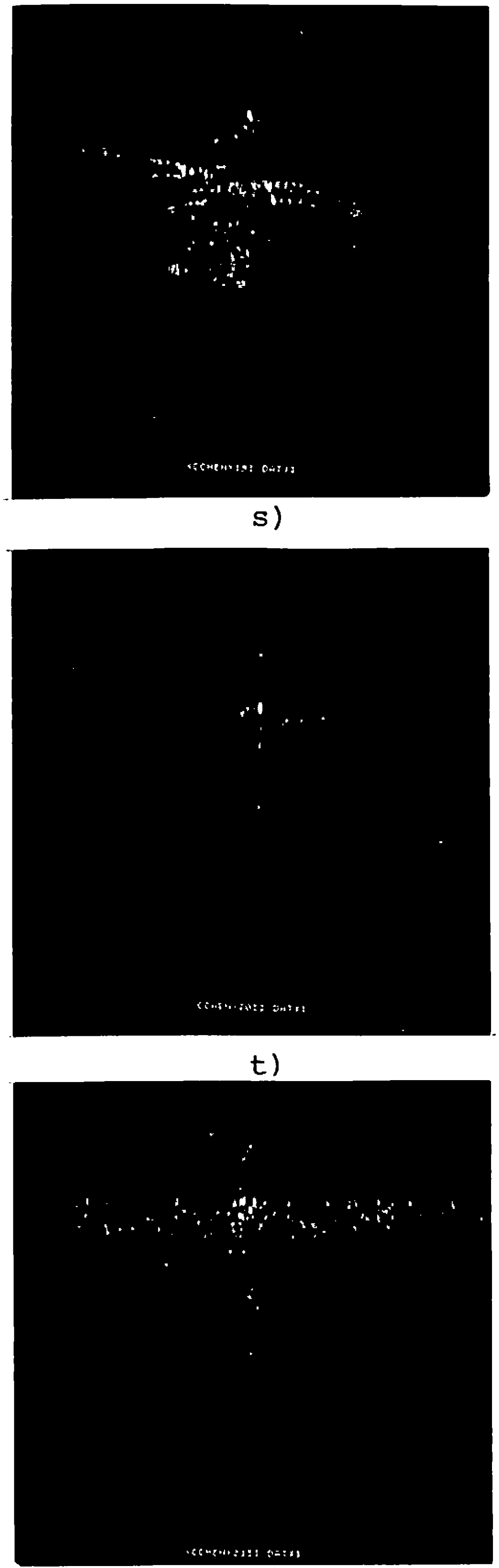

s)

t)

u)

Fig. 8-16. (Continued)

with respect to the fuselage. Since the fuselage trajectory is not parallel to that of the wingtip, the motion compensation did not work and the image is blurred.

8.5 Conclusions

This chapter has presented the experimental results associated with imaging a moving aircraft target from a stationary ground-based radar. Preprocessing techniques for range curvature, range alignment, motion compensation, and coherent presumming are all presented. Gross phase and fine tuning phase are separated for imaging the target. Coherence processing intervals, range collapsing and range re-alignment are all examined. Two data sequences, interval 1 and interval 2, are taken for real radar data. Many parameters are tested and their results are shown. Each resultant image has been tested against the physical aircraft flight information before any interpretations are attempted. Images of encouraging quality confirm the feasibility of the coherent radar imaging of the flying aircraft.

Chapter 9

SUMMARY AND EXTENTIONS

9.1 Summary

This dissertation has presented analysis and experimental results of several radar imaging systems. As a preliminary research of this work, a classification method on two dimensional systems based on the structure of their point spread function matrices has been proposed to aid in understanding imaging systems. The classification principle is universal and cases apply to the specialized field of radar imaging. Many physical examples are shown to fit in most of the cases nicely and it is hoped that more systems could be identified with some of the cases and possibly even new imaging systems developed based on the classified system structure as the image reconstruction techniques advance. We have demonstrated that, depending on the accuracy one pursues, the stripping mode of SAR imaging can range from the non-separate 1-D invariant case to the separable 2-D invariant case. While going to a simpler system model saves some computation time and storage requirement, part of the information becomes irretrievable as a result of approximation. Analysis on the tradeoff between the DOF loss and the simplification of the system PSF is a possible extention of the system classification work.

The radar system analysis and the processing techniques in this dissertation assume discrete linear imaging systems with the target being a rigid body of constant reflectivities. Physical phenomena, e.g., target point blocking, reflectivity change as a function of aspect angle, multiple reflections, parts moving on the target, etc. if completely incorporated in the PSF's would make the actual imaging system fairly nonlinear. Another nonlinearity comes from our data processing in which both the radar returns and the resultant image are transformed on a point by point basis, e.g., taking the log of the magnitude parts, to reduce the dynamic range. The effects of those nonlinearities remain to be analyzed in the extention work.

In the RAT-SCAT system, image reconstruction was assumed separable on the individual data section following considerations of physical limitations and fast-algorithm desirability. Larger sectors (e.g., 25.6°) could have been processed if we had chosen to nonseparably process the data in which a constant target reflectivity function could be assumed. The quality of the final RAT-SCAT images are limited by target size, wavelength, bandwidth of the transmitted signal set, fidelity of the radar receiver processing unit, background reflectivity, sidelobe effect, and ability to find the true rotation center of the component images.

While the RAT-SCAT imaging is performed under a well-controlled environment, the imaging geometry in Chapters 7 and 8 is more realistic in that a full-sized flying aircraft target is imaged. However, because of the increased complexity of the PSF , a method of system decomposition is proposed in which the preprocessing simplifies the relationship between the transformed data and the object function. Range realignment, range curvature compensation, motion compensation, and presuming are examples of preprocessing performed. After the preprocessing, the remaining system is (hopefully) a separable one and fast processing techniques like the FFT can be applied. Side lobe effects in the final images can be greatly reduced by incorporating a weighting window upon the data in the presumming and FFT processings.

In both the RAT-SCAT and the motion-induced-aperture imaging, the range bin width and azimuth bin width are equalized by interpolation techniques to make square images suitable for human interpretation. This involves calculating the relative magnitudes of the range bandwidth which is determined by the bandwidth of the transmitted radar signals and the azimuth bandwidth which is proportional to the amount of rotation of the target.

While the range resolution is independent of the carrier frequency f_0 of the radar signals, the azimuth resolution is a function of f_0. In fact, it is the large f_0

which makes imaging possible along the azimuth direction with only a few degrees of the target rotation. Recall that although the PSF's of the tomographic system have a very similar mathematical form as those of the RAT-SCAT system, it needs a full 180^{0} projections to reconstruct the image because of a zero f_0.

The final radar images are enhanced to reveal more details. Most of the postprocessing enhancement techniques used are nonlinear and belong to the immeasurable art of image enhancement and image analysis [9-1]. Nevertheless the understanding of the characteristics of the radar imaging systems, in particular the cascaded decomposition of the processing procedure, could aid in the advancement of techniques for image storage, encoding, enhancement, quantization, and restoration. For example, knowing the dynamic range limitation of the film and the Fourier transformation property of the lens, we could store the radar images on the films in the frequency domain to spread the energy over the film [9-2]. In the image encoding domain, Chen [9-3] has developed a radar image coding method based on dual mode interpolation for images with strong targets and hence high dynamic range.

9.2 Sonar Imaging

Finally, a potential application of the coherent radar imaging principle to other systems will be discussed.

As described earlier, the two-dimensional imaging systems must collect a set of one-dimensional data about the target reflectivity or transmission from different aspect angle of the object for image reconstruction. In the MFS system, the gathered data is in the frequency domain and represents points at particular target aspect angles and with radii being the radar frequency f_c translated into the spatial frequency domain or $\frac{2f_c}{c}$ where c is the speed of light in the case of radar imaging. One advantage of the large f_0 lies in the fact that it places the data points away from the origin of the frequency coordinate system making the data points relatively distant from each other and less redundant, as analyzed in Chapter 4. The range bandwidth is $\frac{2B_r}{c}$ in the radar imaging, where B_r is the effective bandwidth of the transmitted signals in Hz. Because of the exceedingly large value of c, a very large bandwidth B_r of the signal is required to achieve a fine range resolution comparable to the target size. For example, bandwidths larger than 1024 MHz are required to achieve a range resolution of 0.5 foot. This large bandwidth requirement has set many restrictions on the system design and limitations on its overall performance.

In the sonar system, the situation is quite different. Here the propagation speed v of the sound in, say the vacuum, is only 1086 ft/sec approximately. The disparity between the light speed and sound speed is in the 6th order of 10's power. To obtain the same data points in the frequency domain of a sonar system as in the radar system requires

$$\frac{2f_0}{c} = \frac{2f_s}{v}$$

and (9-1)

$$\frac{2B_r}{c} = \frac{2B_s}{v}$$

where f_s and B_s are the carrier frequency and the bandwidth of the sonar wave in Hz, respectively. Thus $f_s = 6.6$ kHz and $B_s = 565$ Hz in the sonar system would be compatible with $f_0 = 6.6$ kH_z and $B_r = 512$ MHz in the radar system, a required bandwidth only 10^{-6} of that of the radar system. An interpretation of the above analysis is as follows: the amount of information about the target inferrable by a single pulse is given by the time-bandwidth-product of the received signal, or approximately the number of range bins on the target. Since the time duration of the received signal is in proportion to the time on target (TOT) it follows that for a fixed number of TBP, the required bandwidth is higher in the case of a faster propagation speed or a smaller TOT.

The above analysis is based purely on mathematical comparison. Because of the large characteristic differences between the electromagnetic waves and sonar waves, there are many physical considerations to be made before actually applying the SAR techniques to the sonar imaging system. For example, in radar imaging systems, it is usually assumed that during the transmission and receiving of a single pulse, the target is stationary. This assumption makes imaging equations relatively simple and is justified by the high speed of the light. In the sonar system the signal dwell time on the target could be so long (because of a low v) that the target might rotate by a significant amount during TOT and violate the stationarity assumption. Compensating target motion within one pulse time could be very difficult. Also, the PRF requirement is not as easily met because of the slow v. From this point of view, sonar system should be better suitable to imaging slowly moving targets like the submarines. Another major disadvantage with the sonar system is the high attenuation rate of the sound wave which tends to impose a requirement for very high power transmitters even in the modest target range. Besides, target reflectivity under sonar, signal coherence and overall system designs have to be well understood and many experiments performed before the feasibility of sonar imaging can even be assumed.

REFERENCES

[2-1] S. Twomey, "The Application of Numerical Filtering to the Solution of Integral Equations Encountered in Indirect Sensing Measurements," J. Franklin Institute, Vol. 279, pp. 95-109 (1965).

[2-2] S. Twomey, "Information Content in Remote Sensing," Applied Optics, Vol. 13, pp. 942-145 (1974).

[2-3] F. Gori and G. Guattari, "Shannon Number and Degrees of Freedom of an Image," Opt. Comm., Vol. 7, pp. 163-165 (1973).

[2-4] D.G. McCaughey and H.C. Andrews, "Degrees of Freedom for Projection Imaging," IEEE Trans. on Acoustics, Speech, and Signal Processing, Vol. ASSO-25, No. 1, pp. 63-73 (Feb. 1977).

[2-5] H.C. Andrews and B.R. Hunt, Digital Image Restoration, Prentice Hall, Englewood Cliffs, New Jersey (1977).

[2-6] H.C. Andrews and C.L. Patterson, "Singular Value Decomposition and Digital Image Processing," IEEE Trans. Acoustics, Speech, and Signal Processing, Vol. ASSP-24, pp. 26-53 (Feb. 1976).

[2-7] B.R. Hunt, "A Matrix Theory Proof of the Discrete Convolution Theory," IEEE Trans. Audio Electro-acoustics, Vol. AV-19, pp. 285-288 (1971).

[2-8] R. Bellman, Introduction to Matrix Analysis, 2nd Ed., New York: McGraw-Hill (1970).

[2-9] C.C. Chen, "Synthetic Aperture Radar and Imaging System of the Stripping Mode," USCIPI Report #770, USC, Los Angeles, Calif. 90007, (Sept. 1977).

[2-10] J.W. Goodman, Introduction to Fourier Optics, McGraw-Hill, New York (1968).

[2-11] R.O. Harger, Synthetic Aperture Radar Systems, Academic Press, New York (1970).

[2-12] E.N. Leith, "Range-Azimuth-Coupling Aberrations in Pulse-Scanned Imaging Systems," *JOSA*, Vol. 63, No. 2, pp. 119-126 (Feb. 1973).

[2-13] A.W. Rihaczek, *Principles of High-Resolution Radar*, McGraw-Hill, New York (1967).

[2-14] A.A. Sawchuk, "Space-Variant Image Restoration by Coordinate Transformation," *JOSA*, Vol. 64, No. 2, pp. 138-144 (Feb. 1974).

[2-15] A.A. Sawchuk, "Space-Variant System Analysis of Image Motion," *JOSA*, Vol. 63, No. 9, pp. 1052-1063 (Sept. 1973).

[2-16] H.C. Andrews, *Computer Techniques in Image Processing*, Academic Press, New York (1970).

[2-17] R.A. Crowther, et.al., "The Reconstruction of a Three-Dimensional Structure from Projections and its Applications to Electron Microscopy," *Proc. Ron. Soc. Lond. A 317*, 1970.

[3-1] H.C. Andrews and B.R. Hunt, *Digital Image Restoration*, Prentice-Hall, 1977.

[3-2] M.I. Skolnik, *Radar Handbook*, McGraw-Hill, 1970.

[3-3] A.W. Rihaczek, *Principles of High-Resolution Radar*, McGraw-Hill, 1969.

[3-4] D.A. Ausherman,"Digital vs. Optical Techniques in SAR Data Processing," *Proceedings of the International Optical Computing Conference 1977, SPIE Volume 119*.

[3-5] W.M. Brown and L.J. Porcello, "An Introduction to Synthetic-Aperture Radar," *IEEE Spectrum*, September 1969.

[3-6] H.L. McCord, "The Equivalence Among Three Approaches to Deriving Synthetic Array Patterns and Analyzing Processing Techniques," *IRE Transactions on Military Electronics*, April 1962.

[3-7] W.M. Brown, et.al. "Synthetic Aperture Processing with Limited Storage and Presuming," *IEEE Transactions on Aerospace and Electronic Systems*, Vol. AES-9, No. 2, March 1973.

[3-8] J.W. Goodman, *Introduction to Fourier Optics*, McGraw Hill, 1968.

[4-1] J.C. Kirk, Jr., "Motion Compensation for SAR," *IEEE Transactions Aeronautical and Electrical Systems*, Vol. 11, No. 3, May 1975.

[4-2] J.C. Kirk, Jr., "A Discussion of Digital Processing in SAR," *IEEE Transactions Aeronautical and Electrical Systems*, Vol. 11, No. 3, May 1975.

[4-3] M.I. Skolnik, *Radar Handbook*, McGraw-Hill, 1970.

[4-4] F. Gori and G. Guattari, "Shannon Number and Degrees of Freedom of an Image," *Optics Communication*, Vol. 7, No. 2, 1973, pp. 163-165.

[4-5] S. Twomey, "Information Content in Remote Sensing," *Applied Optics*, Vol. 13, No. 4, 1976, pp. 942-945.

[4-6] S. Hou and H.C. Andrews, "Fundamental Limits and Degrees of Freedom of Imaging Systems," *Proceedings of SPIE*, Vol. 74, 1976.

[4-7] D.G. McCaughey and H.C. Andrews, "Degrees of Freedom for Projection Imaging," *IEEE Transactions on Acoustics, Speech and Signal Processing*, Vol. ASSP-25, No. 1, February 1977.

[4-8] M. Marcus and H. Ming, *A Survey of Matrix Theory and Matrix Inequalities*, Allyn and Bacon, 1964, pp. 24.

[4-9] J.W. Goodman, *Introduction to Fourier Optics*, McGraw-Hill, 1968.

[4-10] E.N. Leith, "Quasi-Holographic Techniques in the Microwave Region," *Proceedings of the IEEE*, Vol. 59, No. 9, September 1971.

[4-11] R.O. Harger, *Synthetic Aperture Radar Systems*, Academic Press, 1970, pp. 37-42.

[4-12] R.O. Harger, *Synthetic Aperture Radar Systems*, Academic Press, 1970, pp. 64-65.

[4-13] W.M. Brown and R.J. Fredricks, "Range-Doppler Imaging with Motion Through Resolution Cells," *IEEE Transactions on Aeronautical and Electrical Systems*, Vol. AES-5, No. 1, January 1969, pp. 98-102.

[4-14] E.N. Leith, "Range-Azimuth-Coupling Aberrations in Pulse-Scanned Imaging Systems," *JOSA*, Vol. 63, No. 2, February 1973, pp. 119-126.

[4-15] E.N. Leith, "Complex Spatial Filter for Image Deconvolution," _Proceedings of IEEE_, Vol. 65, No. 1, January 1977, pp. 18-28.

[5-1] H.C. Marlow, et.al., "The RATSCAT Cross-Section Facility," _Proceedings of the IEEE_, Aug. 1965.

[5-2] R.O. Harger, _Synthetic Aperture Radar Systems_, Academic Press, 1970.

[5-3] R.N. Bracewell and A.C. Riddle, "Inversion of Fan Beam Scans in Radio Astronomy," _Astrophysics Journal_, Vol. 150, 1967.

[5-4] L.A. Shepp and B.F. Loga, "The Fourier Reconstruction of a Head Section," _IEEE Transactions on Nuclear Science_, Vol. NS-21, June 1974.

[5-5] D.G. McCaughey and H.C. Andrews, "Degrees of Freedom for Projection Imaging," _IEEE Transactions on Acoustics, Speech, and Signal Processing_, Vol. ASSP-25, No. 1, Feb. 1977.

[5-6] G.N. Ramachandran and A.V. Lakshminarayanan, "Three Dimensional Reconstruction from Radiographs and Electron Micrographs: Application of Convolution Instead of Fourier Transforms," _Proc. Nat. Acad. Sci._, Vol. 68, 1971.

[5-7] P.R. Smith, et.al., "Image Reconstruction from Finite Numbers of Projections," _J. Phys. A.: Math., Nucl. Gen._, Vol. 6, March 1973.

[5-8] H.C. Andrews and B.R. Hunt, _Digital Image Restoration_, Prentice-Hall, 1977.

[6-1] M.I. Skolnik, _Radar Handbook_, McGraw-Hill, 1970.

[6-2] A.V. Oppenheim and R.W. Schafer, _Digital Signal Processing_, Prentice-Hall, 1975.

[7-1] C.C. Chen and H.C. Andrews, "Radar Turntable Imaging," submitted for publication in _IEEE Transactions on Aerospace and Electronic Systems._

[7-2] R.O. Harger, _Synthetic Aperture Radar Systems_, Academic Press, 1970.

[7-3] H.C. Andrews and B.R. Hunt, _Digital Image Restoration_, Prentice-Hall, 1977.

[7-4] C.C. Chen, and H.C. Andrews, "Data Structures of Two Variable to Two Variable Mappings," submitted for publication in *IEEE Transactions on Circuits and Systems*.

[7-5] E.N. Leith, "Complex Spatial Filters for Image Deconvolution," *Proceedings of the IEEE*, Vol. 65, No. 1, January 1977.

[7-6] E.N. Leith, "Range-Azimuth-Coupling Aberrations in Pulse Scanned Imaging Systems," *JOSA*, Vol. 63, No. 2, February 1973.

[9-1] W.K. Pratt, "Digital Image Processing," John Wiley & Sons, 1978.

[9-2] D. Ausherman, ERIM, private communications.

[9-3] W.H. Chen, "A Dual Mode Nonlinear Interpolative Compressor for SAR Images," *Proceedings of the 19th Annual SPIE Symposium on Efficient Transmission of Pictorial Information*, San Diego, August 1975.